GUIDED-MODE RESONANT FILTERS AND REFLECTORS:

PRINCIPLES, DESIGN, AND

FABRICATION

by

MANOJ NIRAULA

Presented to the Faculty of the Graduate School of

The University of Texas at Arlington in Partial Fulfillment

of the Requirements

for the Degree of

DOCTOR OF PHILOSOPHY

THE UNIVERSITY OF TEXAS AT ARLINGTON

May 2016

Acknowledgements

I joined the Nanophotonics Device Group at the University of Texas at Arlington as an Undergraduate Research Associate in May, 2013. During my three years here, the endless support I received from the group played a great part in my success. I would like to acknowledge and thank everyone who helped me succeed.

I express the utmost gratitude towards Dr. Magnusson, my doctoral advisor, for the opportunity, resources, mentorship, and inspiration that he provided during my time in Nanophotonics Device Group. He encouraged me to pursue my own research interests that made my lab work enjoyable and fruitful. He inspired me to become a better scientist and an efficient communicator.

I am greatly thankful towards Dr. Jae Woong Yoon for his mentorship, guidance, and co-work. The theoretical and experimental skills I learned from him have enabled me to become an independent researcher and a problem solver.

I also acknowledge Dr. Kambiz Alavi, Dr. Yuze Sun, Dr. Michael Vasilyev, and Dr. Weidong Zhou for the time they have devoted serving as a member of my dissertation committee. Their advice, guidance, and criticism helped me improve my understanding of this dissertation.

I thank Dr. Kyu Jin Lee and Dr. Yeong Hwan Ko for their help and guidance during my research. Dr. Lee trained me to use the lab equipment and answered many lithography/process related questions I had. Mrs. Kristin Pearl Bergfield was extremely helpful with her administrative support during the first year of my PhD program. I thank Dr. Yiwu Ding and for writing the 1D rigorous coupled-wave analysis (RCWA) algorithm

Finally, I thank my parents Tejnath Niraula and Sita Devi Niraula and my uncle Surendra Niraula for their continuous support.

<div align="right">

Manoj Niraula

May, 2016

</div>

Abstract

GUIDED-MODE RESONANT FILTERS AND REFLECTORS:
PRINCIPLES, DESIGN, AND
FABRICATION

Manoj Niraula, PhD

The University of Texas at Arlington, 2016

Supervising Professor: Robert Magnusson

Thin-film structures incorporating wavelength-scale gratings provide functionalities for applications in various optical systems. Previously, spectral filters, wideband reflectors, and polarizers have been identified as potential application areas. In this dissertation, we overview the operational principles of these resonant periodic structures, discuss the methods of their design and fabrication, and propose and demonstrate novel functionalities for spatial and spectral filtering, and unpolarized wideband reflection. Fashioned with materially sparse gratings, these optical devices are easy to fabricate and integration friendly compared to their traditional multi-layer counterparts making their research and development critical for practical applications.

We study, theoretically, modal properties and parametric dependence of resonant periodic bandpass filters operating in the mid- and near-infrared spectral domains. We investigate three different device architectures consisting of single, double, and triple layers based on all-transparent dielectric and semiconductor thin films. The three device classes show high-performance bandpass filter profiles with broad, flat low-transmission sidebands accommodating sharp transmission peaks with their efficiencies approaching 100% with appropriate blending of multiple guided modes. We present three modal

coupling configurations forming complex mixtures of two or three distinct leaky modes coupling at different evanescent diffraction orders. These modal compositions produce various widths of sidebands ranging from ~30 nm to ~2100 nm and transmission peak-linewidths ranging from ~1 pm to ~10 nm. Our modal analysis demonstrates key attributes of subwavelength periodic thin-film structures in multiple-modal blending to achieve desired transmission spectra.

We provide the first experimental demonstration of high-efficiency and narrow-linewidth resonant bandpass filter applying a single patterned silicon layer on a quartz substrate. Its performance corresponds to bandpass filters requiring 15 traditional Si/SiO_2 thin-film layers. The feasibility of sparse narrowband, high-efficiency bandpass filters with extremely wide, flat, and low sidebands is thereby demonstrated. This class of devices is designed with rigorous solutions of Maxwell's equations while engaging the physical principles of resonant waveguide gratings. An experimental filter presented exhibits a transmittance of ~72%, bandwidth of ~0.5 nm, and low sidebands spanning ~100 nm. The proposed technology is integration-friendly and opens doors for further development in various disciplines and spectral regions where thin-film solutions are traditionally applied.

We demonstrate concurrent spatial and spectral filtering as a new outstanding attribute of resonant periodic devices. This functionality is enabled by a unique, near-complete, reflection state that is discrete in both angular and spectral domains and realized with carefully crafted nanogratings operating in the non-subwavelength regime. We study the pathway and inter-modal interference effects inducing this intriguing reflection state. In a proof-of-concept experiment, we obtain angular and spectral bandwidths of ~4 mrad

and ~1 nm, respectively. This filter concept can be used for focus-free spectral and spatial filtering in compact holographic and interferometric optical instruments.

We report unpolarized broadband reflectors enabled by a serial arrangement of a pair of polarized subwavelength gratings. Optimized with inverse numerical methods, our elemental gratings consist of a partially etched crystalline-silicon film on a quartz substrate. The resulting reflectors exhibit extremely wide spectral reflection bands in one polarization. By arranging two such reflectors sequentially with orthogonal periodicities, there results an unpolarized spectral band possessing bandwidth exceeding those of the individual polarized bands. In the experiments reported herein, we achieve zero-order reflectance exceeding 97% under unpolarized light incidence over a 500-nm-wide wavelength band in the near-infrared domain. Moreover, the resonant unpolarized broadband accommodates an ultra-high-reflection band spanning ~85 nm and exceeding 99.9% in efficiency. The elemental polarization-sensitive reflectors based on one-dimensional resonant gratings have simple design, robust performance, and are straightforward to fabricate. Hence, this technology is a promising alternative to traditional multilayer thin-film reflectors especially at longer wavelengths of light where multilayer deposition may be infeasible or impractical.

We demonstrate an interesting attribute of resonant bandpass filters which is high angular stability for fully conical light incidence. Fashioning an experimental bandpass filter with a subwavelength silicon grating on a quartz substrate, we show that fully conical incidence provides an angular full-width at half-maximum linewidth of ~9.5° compared to a linewidth of ~0.1° for classical incidence. Slow angular variation of the central wavelength with full conical incidence arises via a corresponding slow angular variation

of the resonant second diffraction orders driving the pertinent leaky modes. Moreover, full conical incidence maintains a profile with a single passband as opposed to the formation of two passbands characteristic of resonant subwavelength gratings under classical incidence. Our experimental results demonstrate excellent stability in angle, spectral profile, linewidth, and efficiency.

Finally, we propose a novel method of design and fabrication of photonic lattices that incorporates the best of both worlds: a polarized resonant grating can be designed and converted to its unpolarized lattice equivalent using the same design parameters to obtain a similar performance. We show this in context of a single-layer polarized bandpass filter operating at 1550 nm with ~100% transmission efficiency. An unpolarized square-hole lattice with identical parameters operates as a bandpass filter at ~1560 nm with ~70% transmission efficiency. Moreover, conventional laser interference lithography technique for mask patterning is limited to circular-hole photoresist lattice. We propose a method to lay down a metal hard-mask by lifting-off patterned photoresist in two steps for a square-hole lattice. Our comprehensive study provides new principles for easy design and fabrication of square-hole photonic lattices for unpolarized guided-mode resonance applications.

Table of Contents

List of Illustrations

List of Tables

Chapter 1
Introduction and Background

Introduction

Recent advances have shown that technology based on light is a dominant aspect of the modern world. Not only are light waves the fastest way to send information across two points, their high frequencies (THz-scale) allow larger modulation and bandwidth in optical communications. Light can be used as a means of rapid detection of molecular composition and occurrence of biochemical reactions in medical diagnosis. Infrared light from distant stars and galaxies helps us understand the history and composition of our cosmos. Presently, electrical computing is nearing its saturation in terms of data throughput and processing speed, thus paving a path towards research and development of optical computing to overcome these limitations. With applicability in virtually boundless fields of science and technology, light-manipulation-based systems will be a cornerstone of our future technological endeavors.

To advance optical systems, it is important to understand and appreciate the interactions between light and objects, especially of size comparable to the light's wavelength. One of the earliest such interactions was reported by R. W. Wood in 1902 [1]. Wood referred to the diffraction spectrum with a distinct "edge" produced by a metallic-diffraction grating as astounding and anomalous. He noticed that the diffraction spectrum only occurred for p-polarized light and experienced about a 10:1 intensity drop under certain conditions. This later came to be known as Wood's anomaly. In 1907, Lord Rayleigh theorized higher-order scattering of light relative to the periodicity of the grating lines.

Rayleigh's theory on light scattering could predict the occurrences of Wood anomalies at the "edge" of a band [2]. However, it could not explain the 10:1 drop in intensity at lower frequencies.

In 1936, Strong evaporated different metal coatings on gratings of same periodicity and showed that the spectral location of Wood's anomalies depended on the type of the coating and angle of incident light [3]. Strong noticed that the location of passing-off (or "edge") for higher-order diffraction depended solely on the grating period, and not the type of metal coating. In 1941, Fano identified two anomalies: a sharp anomaly or "edge" occurring at frequencies predicted by Rayleigh and a diffuse anomaly that extended at lower frequencies from Rayleigh and consisted 'generally of a minimum and maximum of intensity (one dark band and one bright band)' [4]. A guided-wave approach based explanation of Wood's anomaly was provided by Hessel and Oliner in 1965 [5]. There, Rayleigh's anomaly at the "edge" of diffraction spectrum was attributed to 'the emergence of a new spectral order at glazing angle.' Fano's diffusion anomaly was extended as a resonance type related to the guided waves supported by the grating.

Although the early experiments by Wood and Fano involved metallic gratings, dielectrics soon became an additional material of interest due to their low absorption coefficient. Invention of holographic lithography techniques to create grating patterns [6] and formulation of rigorous methods to solve grating equations [7] increased the interest in dielectric waveguide-grating structures. In 1985, Mashev and Popov studied the anomalous high reflection peak in the zero-order diffraction regime using a dielectric-coated grating [8]. They showed that, in theory, the reflection peak reaches 100% in efficiency. They experimentally obtained ~35% reflection peak efficiency at normal

incidence and wavelength tunability by varying the angle. In 1990, Wang *et al.* proposed a simple method of predicting the spectral locations of anomalous resonances in reflection [9]. This resonance mechanism was applied as reflection filters that were demonstrated both theoretically [10] and experimentally [11,12]; and also extended to transmission filters [13]. Implementation of inverse optimization methods such as genetic algorithm [14] and particle-swarm optimization [15] in the design of grating geometry has led discovery of useful grating structures performing as bandpass filters [14,16], wideband reflectors [17–19], optical biosensors [20], polarizers [21,22], and absorbers [23,24]. These fundamental application areas are highly important in advancing optical systems to meet the technological needs of the future.

Background

Grating Equation and Subwavelength Regime

For a diffraction grating as shown in Figure 1–1, the relationship between diffraction angle (θ_m) for *m*-th order diffraction and the angle of incidence (θ_i) is given by Rayleigh's grating equation [2]:

$$n \sin \theta_m = n_C \sin \theta_i + m \frac{\lambda}{\Lambda},$$

(1.1)

where *n* is the refractive index of diffracted wave propagation medium, n_C is the refractive index of the incidence medium, λ is the wavelength of incident light, and Λ is the grating period. At normal incidence ($\theta_i = 0$), Eq. 1.1 reduces to:

$$\sin \theta_m = m \frac{\lambda}{n\Lambda}.$$

(1.2)

3
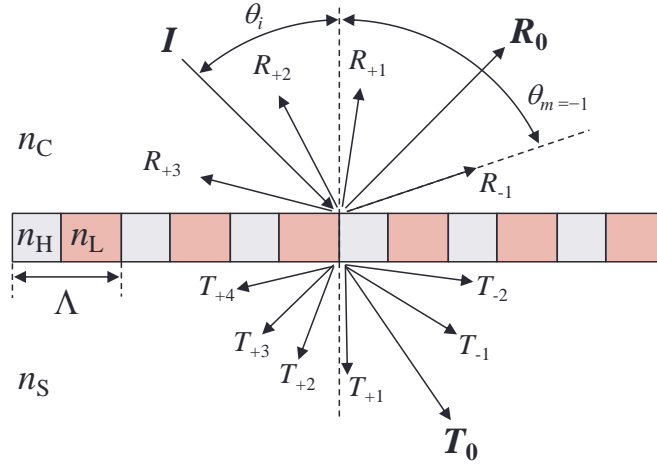
Figure 1-1 Schematic illustration of different diffraction orders due to periodic gratings. The grating layer consists of index modulation of n_H and n_L with a period Λ. Light is illuminated from the cover region with index n_C at an angle θ_i. R_m and T_m represent m-th order ($m = 0,\pm1, \pm2\ldots$) diffracted waves in reflection and transmission, respectively. θ_m is the angle of an m-th order diffracted wave.

In Eq. 1.2, when the right hand side term is less than 1, θ_m takes a finite value and the wave is propagating. Whereas, when the right hand side term is greater than 1, θ_m does not exist, i.e. m-th order diffracted wave is non-propagating and evanescent. In many applications, it is desirable to only have zero-order propagating waves. This can be guaranteed by setting grating period such that $\lambda/n\Lambda > 1$. In this case, all non-zero diffraction orders are evanescent. This type of grating architecture is called *subwavelength gratings*. Likewise, grating architectures where higher diffraction can propagate in the cover or substrate media are called *non-subwavelength gratings*.

Guided-Mode Resonance Mechanism

The term guided-mode resonance was first used in a 1990 paper by Wang *et al*. where the authors used rigorous coupled-wave theory to study and estimate locations of resonance anomalies due to dielectric waveguide-gratings [9]. The 1992 [10] and 1993 [25]

4
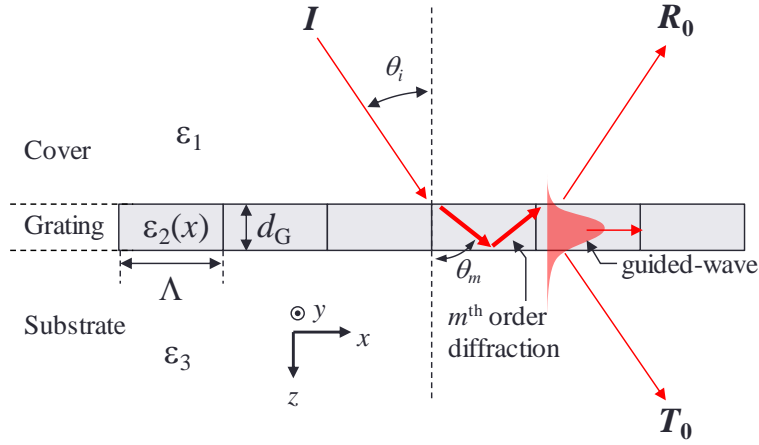
Figure 1–2 Planar waveguide-grating model to study guided-mode resonance mechanism. The grating layer consists of spatial modulation of refractive index. In the waveguide-grating, m-th order diffraction from the incident light is guided.

papers by same group extended the study to a transmissive waveguide-grating type structure where wavelength filtering applications using the guided-mode resonance effect was proposed. A canonical representation of the structure is shown in Figure 1-2. It comprises of a cover region, also the incidence medium, with relative permittivity ε_1, spatially modulated grating layer with permittivity $\varepsilon_2(x) = \varepsilon_g + \Delta\varepsilon \cos Kx$, thickness d_G, and period Λ, and a substrate region with permittivity ε_3. Here, ε_g is the average relative permittivity of the grating layer and is greater than both ε_1 and ε_3, $\Delta\varepsilon$ is the index modulation, and grating vector $K = 2\pi/\Lambda$. Light of wavelength λ is incident on the waveguide grating through the cover region at an angle of θ_i. In the waveguide-grating layer, θ_m is the m-th order diffraction and drives a guided mode as shown in the figure.

If transverse electric (TE, electric field of incident light along y-axis) light polarization is assumed, the coupled-wave equation in the grating layer is [26]

5

$$\frac{d^2\hat{S}_m(z)}{dz^2}+\left[k^2\varepsilon_g-k^2\left(\sqrt{\varepsilon_g}\sin\theta_m-m\lambda/\Lambda\right)^2\right]\hat{S}_m(z)+\frac{1}{2}k^2\Delta\varepsilon\left[\hat{S}_{m+1}(z)+\hat{S}_{m-1}(z)\right]=0,$$

(1.3)

where $\hat{S}_m$ is the m-th diffraction order inhomogeneous plane wave amplitude, wave-number $k=2\pi/\lambda$, and λ is the free-space wavelength. As the index modulation ($\Delta\varepsilon$) approaches zero, the waveguide-grating resembles a planar unmodulated waveguide and its wave equation is given by

$$\frac{d^2E(z)}{dz^2}+\left(k^2\varepsilon_g-\beta^2\right)E(z)=0.$$

(1.4)

Here, β is the propagation constant. The guided-wave in Figure 1-2 can be excited if the effective refractive index of the waveguide $N = \beta/k$ satisfies

$$\max\left(\sqrt{\varepsilon_1},\sqrt{\varepsilon_1}\right)\leq N<\sqrt{\varepsilon_g}.$$

(1.5)

When $\Delta\varepsilon\rightarrow 0$, Eqs. 1.3 and 1.4 can be directly compared and the propagation constant of the waveguide grating can be expressed as

$$\beta\rightarrow\beta_m=k\left(\sqrt{\varepsilon_g}\sin\theta_m-m\frac{\lambda}{\Lambda}\right),$$

(1.6)

and the effective waveguide index is $N_m = \beta_m/k$. Here it is important to note that for a guided mode to be supported by the waveguide, the β of the mode must satisfy Eq. 1.6.

The eigenvalue equation for modulated slab waveguide can be obtained by referring to the eigenvalue equation for unmodulated case [27]. The eigenvalue equation for TE polarized light incidence is

$$\tan\left(\kappa_m d\right)=\frac{\kappa_m\left(\gamma_m+\delta_m\right)}{\kappa_m^2-\gamma_m\delta_m},$$

(1.7)

where $\kappa_m = \left(\varepsilon_g k^2 - \beta_m^2\right)^{\frac{1}{2}}$, $\gamma_m = \left(\beta_m^2 - \varepsilon_1 k^2\right)^{\frac{1}{2}}$, and $\delta_m = \left(\beta_m^2 - \varepsilon_3 k^2\right)^{\frac{1}{2}}$. For transverse magnetic (TM, magnetic field along y-axis) polarized light, the eigenvalue equation is

$$\tan\left(\kappa_m d\right) = \frac{\varepsilon_g \kappa_m \left(\varepsilon_3 \gamma_m + \varepsilon_1 \delta_m\right)}{\varepsilon_1 \varepsilon_3 \kappa_m^2 - \varepsilon_g^2 \gamma_m \delta_m}. \tag{1.8}$$

Equations 1.7 and 1.8 give the locations of waveguide mode resonances for TE and TM polarizations. It is worthwhile to note that expressions for TE and TM waves in these equations are different. This follows that the resonance wavelength for TE and TM waveguide modes are also different. This difference introduces polarization-selectivity in guided-mode resonance based devices as will be discussed in following chapters.

The derivations in this section considers a grating layer with continuous sinusoidal index modulation given by $\varepsilon_2(x) = \varepsilon_g + \Delta\varepsilon \cos Kx$. In practice, waveguide-gratings can have discrete index modulations including two-part periods. Such grating architectures can be solved rigorously through Fourier series expansion of form [28]

$$\varepsilon_2(x) = \sum_h \varepsilon_h \exp\left(j\frac{2\pi h}{\Lambda}\right) \tag{1.9}$$

where ε_h is the h-th Fourier component of grating layer permittivity. The diffraction grating is solved by finding solutions to Maxwell's equations for the boundary-value-problems at the cover, grating, and substrate regions. Details are provided in [28,29].

Dissertation Overview

This dissertation presents theoretical and experimental study on bandpass filters, experimental demonstration of unpolarized broadband reflectors, proposal and experimental demonstration of a novel concurrent spatial and spectral filters, and design

and fabrication principles of unpolarized photonic lattices. These contents are divided into eight chapters. Each chapter is briefly discussed below.

Chapter 2 provides an overview of the theoretical, inverse optimization, and experimental methods applied in the subsequent chapters. Spectral simulations are carried out using rigorous coupled-wave analysis and finite element method. Discussion about particle-swarm optimization, an inverse optimization method is included. Experimental methods include holographic lithography, dry etching, device characterization, and optical measurements.

Chapter 3 provides a theoretical study of three distinct classes of optical bandpass filters and their mode coupling mechanisms. The bandpass filters studied consist of a single layer Se-Ge binary grating structure, a single-layer partially etched Si grating structure, and a three-layer embedded SiO_2 on Si grating structure. Across the studied grating architectures, resonant modes forming the stopbands and passbands generally differ. Parametric dependence of bandpass profiles is also studied.

Chapter 4 includes an experimental demonstration of a narrow-linewidth bandpass filter. The bandpass filter is designed using partially etched Si gratings on quartz substrate. Fabrication steps include holographic interference lithography and reactive ion etching. Experimental bandpass performance includes 72.1% peak efficiency and 0.48 nm peak linewidth at 1304 nm wavelength of light. Ability to rapidly tune the design wavelength by varying the angle of incidence is also demonstrated.

Chapter 5 presents a novel device concept in the non-subwavelength regime. A near-unity reflection peak is observed in the first-order regime. This resonance peak, unlike reflection peaks in the subwavelength regime, exists only at one wavelength (852

nm) and at normal incidence. This concurrent spatial and spectral selective reflection state is studied by invoking intermodal-interference and pathway-interference mechanisms. The device concept is experimentally demonstrated using sputtered TiO_2 on glass slides. Focus-free spatial filtering of laser outputs is proposed as a potential application of this device class.

Chapter 6 summarizes an experimental demonstration of polarization-independent wideband reflectors. Here, two polarization-selective wideband reflectors based on one-dimensional periodic gratings are sequentially arranged such that their grating vectors are orthogonal to one another. It is shown that this sequential arrangement reflects both TE and TM components of incident light, resulting in broadband unpolarized light reflection. Experimental results show high-efficiency unpolarized wideband reflection and angular-tolerance of the sequentially arranged pairs of polarization-selective broadband reflectors. Reflection efficiency nearing 99.99% in experiment is reported.

Chapter 7 compares the angular tolerance of a resonant bandpass filter under classical and fully conical light incidence. Numerically, it is found that for small angles, the variations in wave vectors of a resonant mode are much smaller for fully-conical incidence than for classical incidence. This angular stability provides ~95x higher angular tolerance in experiment for fully conical incidence compared to its classical counterpart.

Chapter 8 presents the feasibility of conversion from a resonant polarized grating to an unpolarized photonic lattice though direct translation of geometrical parameters. Performance of a polarized bandpass filter is compared to an unpolarized square-hole photonic lattice with exact grating parameters. Similar bandpass profile is numerically demonstrated, however with slight spectral redshift and degradation of transmission

9

efficiency in the unpolarized lattice. Fabrication challenges for square-hole lattice are also discussed and a novel two-step resist liftoff method is proposed.

Chapter 9 provides a summary of the research and illustrates some interesting directions for future work. Experimental unpolarized bandpass filters and concurrent spatial and spectral filters in transmission are identified as promising prospects.

Chapter 2
Methods and Materials

In this chapter, methods of device simulation, inverse optimization, device fabrication, characterization, and optical measurements are discussed. These methods are utilized in producing results summarized in subsequent chapters.

Simulation Tools

Optical responses of resonant periodic structures and their internal fields are simulated using two different computational methods: rigorous coupled-wave analysis and the finite element method.

Rigorous Coupled-Wave Analysis (RCWA)

An RCWA [29] computer algorithm belonging to and created by the Nanophotonics Device Group at University of Texas at Arlington and implemented in MATLAB® environment is used to solve grating structures with 1D periodicity. For structures with 2D periodicity, commercially available RSOFT DiffractMod® is used. We account for material dispersion and extinction coefficients for visible and near-IR wavelengths. There, we use optical constants reported in the literature as well as through our ellipsometric measurements. We have briefly discussed the fundamentals of RCWA computations in Chapter 1. More details about this method are discussed in [29].

Finite-Element Method (FEM)

We use commercially available COMSOL Multiphysics® for FEM [30] computations. We use it mostly to verify the optical response computed using RCWA. In
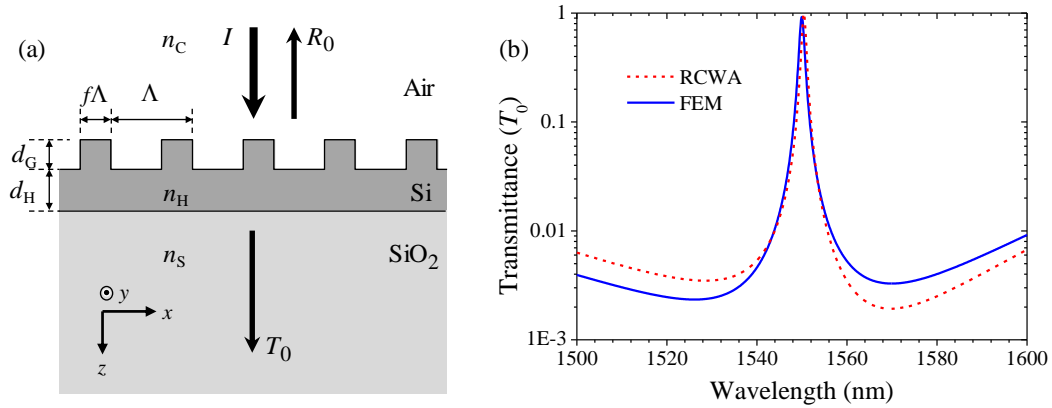
Figure 2-1 Numerical solutions. (a) A resonant periodic structure with partially etched single layer Si on SiO$_2$ substrate. The geometrical parameters are period Λ = 1018 nm, fill factor f = 0.21, grating depth d_G = 355 nm, homogeneous Si layer thickness d_H = 297 nm. The refractive indices are n_C = 1.0 (Air), n_H = 3.48 (Si), and n_S = 1.48 (SiO$_2$). I, R_0, and T_0 represent incident, zero-order reflected, and zero-order transmitted wave, respectively. (b) Numerical solutions of periodic structure in (a) using RCWA (dashed red) and FEM (solid blue) for transverse-electric (TE) polarization of input light at normal incidence.

FEM, a periodic structure is divided into fine triangular meshes and Maxwell's equations are solved for the boundary-value problems at the boundaries of these meshes.

Comparison between RCWA and FEM

COMSOL's geometrical design feature allows a grating structure definition using co-ordinate system as opposed to layer-by-layer limitation in RCWA. In Chapter 4, we discuss the use of FEM to solve optical response and field distribution of an exact fabricated structure.

In both RCWA and FEM, the convergence (accuracy) of a solution depends on computational conditions. For instance, in RCWA, the convergence increases for higher number of spatial harmonics implemented in the computation. On the other hand, a finer mesh-size improves the convergence in FEM. A comparison between RCWA and FEM simulated spectral response is provided in Figure 2-1. The periodic structure shown in Figure 2-1(a) consists of silicon (Si) gratings on glass (SiO$_2$) substrate. The grating geometry

is defined by period Λ = 1.018 mm, fill factor f = 0.21, grating depth d_G = 355 nm, and homogenous Si layer depth d_H = 297 nm. Si and SiO$_2$ are modeled with a constant refractive index of n_H = 3.48 and n_S = 1.48, respectively. Air is the cover medium with index n_C = 1.0. RCWA (red dashed) and FEM (blue solid) simulated spectrum for plane wave incidence at normal angle of incidence and transverse electric (TE) polarization is shown in Figure 2-1(b). In RCWA calculations, we take 20 spatial harmonics in consideration. In FEM (COMSOL) simulations, we set the triangular mesh-size to 'Extra fine.' In the figure, we see a slightly different spectral response for RCWA and FEM computations. It is interesting to note that this difference is not noticeable when y-axis in Figure 2-1(b) is plotted in linear scale. For the purposes of this research, we mostly use RCWA simulated spectrum and ignore the slight discrepancy, if any, between the two techniques.

Inverse Optimization

Inverse optimization facilitates in finding a suitable grating architecture for a particular application, in a virtually infinite parametric space. We use particle-swarm optimization method for inverse optimization.

Particle-Swarm Optimization (PSO)

PSO method for inverse optimization of continuous non-linear functions was proposed by Kennedy and Eberhart in 1995 [31]. Our PSO code uses an RCWA algorithm in forward calculation. Device geometry type, parametric range, refractive indices, and desired spectral response ($\eta_{desired}$) are supplied to the PSO code. Examples of device geometry type defined in PSO code are number of layers, type of periodicity, etc. Parametric range refers to a range of values that a geometrical parameter, grating period
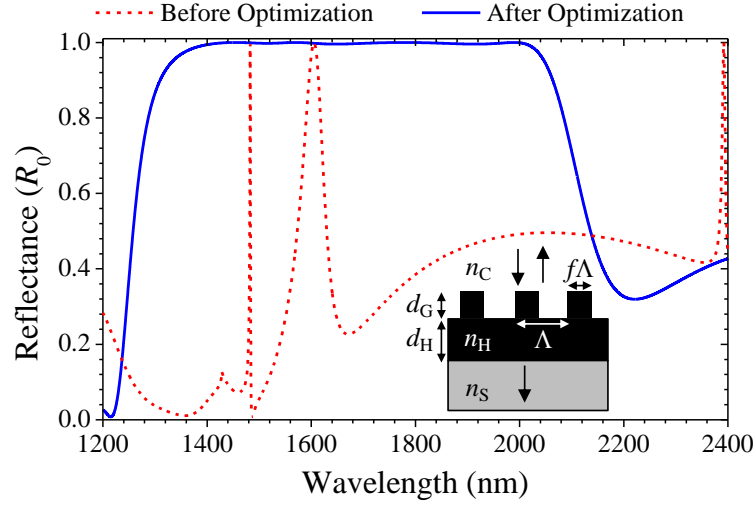
Figure 2-2 Parametric optimization using PSO method. Inset in the figure shows a resonant periodic structure with partially etched single layer dielectric on a substrate. Transverse magnetic (TM) spectral response of the device at normal incidence computed using RCWA before optimization (dashed red) and after optimization (solid blue). In PSO, in this example, R_0 > 99% for ~600 nm-wide wavelength band at ~1700 nm is demanded.

for instance, can take. The PSO code computes and minimizes a fitness function (FF) given as

$$\text{FF} = \left[\frac{1}{N} \sum_{i=1}^{N} \left\{ \eta_{\text{desired}} \left(\lambda_i \right) - \eta_{\text{design}} \left(\lambda_i \right) \right\}^2 \right]^{\frac{1}{2}}, \tag{2.1}$$

where N is the number of wavelength points used to define the desired spectrum, λ_i is the i-th wavelength point, and η_{design} is the spectral response calculated by PSO. Example of a wideband reflection design obtained through PSO is shown in Figure 2-2.

Device Fabrication

In this section, steps undertaken during nanofabrication of resonant grating structures are discussed briefly. The fabrication process is illustrated in Figure 2-3.

14
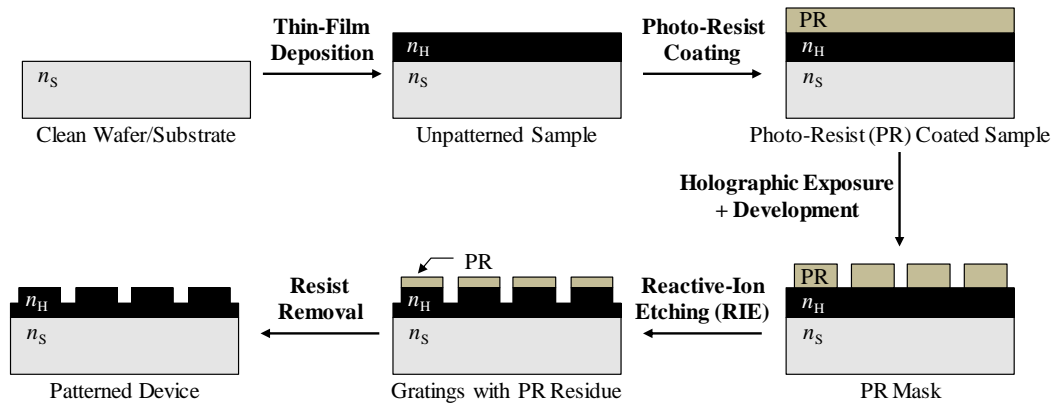
Figure 2-3 General steps undertaken during resonant periodic device fabrication.

Substrate/Wafer Cleaning

Glass substrates and silicon-on-quartz (SOQ) wafers are cleaned using ultra-sonic bath in acetone for 20 minutes followed by immersion in iso-propyl alcohol (IPA) for 5 minutes. The substrates/wafers are then rinsed in deionized (DI) water for another 2 minutes and blown dry using nitrogen (N_2) gas. Ultra-sonic bath removes particle impurities on a wafer.

Thin-Film Deposition

TiO_2, Si, gold, chromium (Cr), etc. thin-films are deposited in our work. TiO_2 films are sputtered on glass slides using a KJL Lab 18 thin-film deposition system. The deposition condition is typically set to 225 W forward power, 2.5 mTorr pressure, and argon (Ar) ambient at 25 sccm. Total sputter time is ~55,000 seconds for ~600 nm thick TiO_2 film. Measured deposition rate is ~0.65 nm/min.

Gold is sputtered using a Denton Vacuum sputtering system in Ar ambient. Gold sputtering time varies by application. For scanning electron microscopy (SEM), sputtering
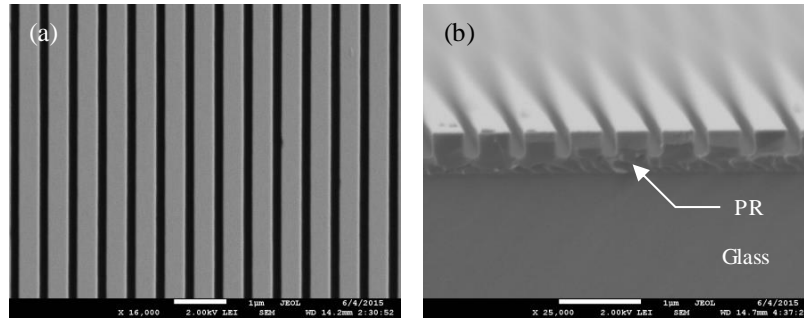
Figure 2-4 SEM images of negative photoresist mask on glass substrate. (a) Top-view and (b) cross-section SEM images of 1D grating photoresist (PR) mask fabricated using holographic lithography are shown. Scale bars in (a) and (b) is 1 μm.

is typically carried out of 60 seconds for a ~5-nm-thick gold film. For gold reference mirror, sputtering is carried out for 20 minutes to obtain ~100-nm-thick coating.

Cr is deposited using an AJA e-beam evaporation system. E-beam evaporation is chosen as it provides a light-of-sight deposition that is highly directional. Typical deposition rate is ~0.5 nm per second at 2.3 A current.

Photo-resist Coating

Photo-resist (PR) is coated using a spin coater. Both positive and negative resists are used. SEPR-701, a positive PR is used when desired grating fill-factor is smaller than 50%. On the other hand, to obtain fill-factor>50%, we use UVN-30, a negative PR. To improve resist adhesion to silicon films, we use Microprimer-HMDS coating before applying a PR coating. Typical spin-coating speeds are ~2500 rpm for negative PR, ~2000 rpm for positive PR, and ~3000 rpm for HMDS. Each spin-coat is followed by a soft bake at 110°C for typically 60 seconds. PR coating is carried out under yellow light in the Nanophotonics Device Group cleanroom at the University of Texas at Arlington.

Holographic Exposure and Development

Holographic interference lithography [6] is implemented to expose the PR coated wafer. In the exposure, we use a collimated beam from our Azure DUV266 laser. In this process, the grating period is controlled by the angle of incidence of the UV light and the grating fill-factor is controlled by the length of exposure. We follow the exposure with hard bake at 110°C for typically 90 seconds. To wash-off the light-activated PR, we develop the wafer in AZ-917 MIF developer for typically 2 minutes, followed by DI water rinse. The wafer is then dried using a N_2 blower. At the end of this process, a desired PR mask on the wafer is obtained. Examples are shown in Figure 2-4.

Reactive-Ion Etching

Next step is to transfer the PR mask to the high-index film. We accomplish this through reactive-ion etching (RIE), a dry etching technique, using a PlasmaLab 80 RIE machine. We etch TiO_2 films using a mixture of Ar (15 sccm), CHF_3 (25 sccm) and CF_4 (25 sccm) gases. The process conditions are: 30 mTorr pressure and 500 W forward power. The etch rate of TiO_2 in our experiment is ~25 nm/min. To etch Si films, we use SF_6 (14 sccm) and CHF_3 (38 sccm) gas mixture. RIE chamber conditions in our Si etch recipe are: 5 mTorr pressure and 100 W forward power. The Si etch rate depends on the size of the mask opening. With low fill-factor PR masks, we obtain up to 40 nm/min etch rate. For high fill-factor masks, the etch rate though Si is ~29 nm/min. The end product of reactive-ion etching is a patterned device ready for characterization and optical measurements.

Characterization Techniques

In order to optimize the fabrication process, wafers and devices are characterized using the following techniques.
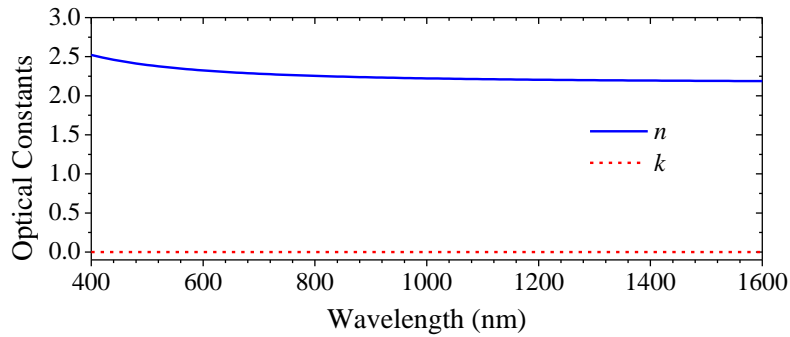
Figure 2-5 Ellipsometry results of a sputtered TiO$_2$ film. Index of refraction (n) and extinction coefficients (k) for a ~600-nm-thick TiO$_2$ film sputtered on a glass substrate are shown.

Ellipsometry

We use ellipsometry to measure the optical constants and thickness of deposited films, as these parameters are process-dependent and tend to vary over time. We use a VB-400 VASE Ellipsometer system capable of measuring film thickness and optical constants in the ~400-1700 nm wavelength range. We characterize a sputtered TiO$_2$ film to obtain the refractive index and extinction coefficient as shown in Figure 2-5. Here we note that expected refractive index of TiO$_2$ is ~2.51 at λ = 850 nm [32]. However, the sputtered TiO$_2$ film index through ellipsometry is ~2.24 at the same wavelength. The lower refractive index of the sputtered film is attributed to voids formed during deposition.
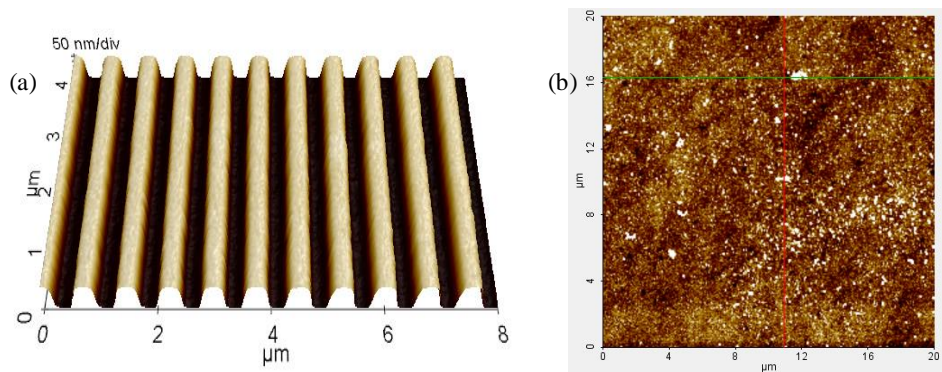
Figure 2-6 Examples of AFM measurements. AFM images showing (a) profile of TiO$_2$ gratings and (b) surface roughness of a representative device.

18
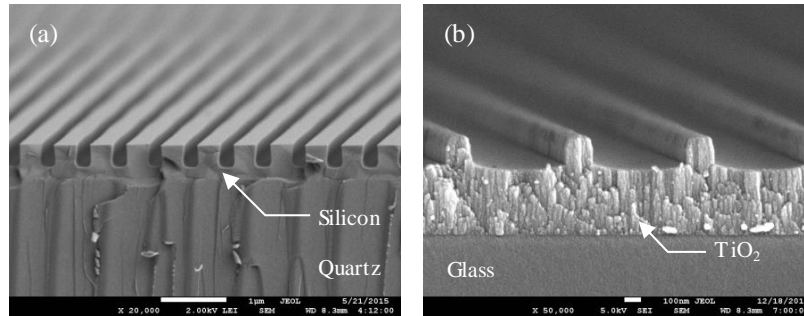
Figure 2-7 SEM images of fabricated devices. Cross-section SEM images of devices with (a) single-crystalline Si gratings on quartz substrate and (b) sputtered TiO_2 gratings on glass substrate. Note the quality of crystalline-Si film in (a) in comparison to a sputtered TiO_2 film in (b). Scale bars in (a) and (b) are 1 µm and 100 nm, respectively.

Atomic Force Microscopy

Atomic Force Microscopy (AFM) is carried out using a XE-70 by Park AFM. This technique is utilized to measure surface roughness of films as well as geometrical parameters of fabricated grating structures. Examples of AFM images are shown in Figure 2-6.

Scanning Electron Microscopy

Scanning electron microscopy (SEM) is used to study the uniformity and geometrical parameters of fabricated devices. A JEOL JSM-7600F field emission scanning electron microscope is used in this study. Gold is sputtered on samples to discourage electric charging during SEM. Examples of SEM are shown in Figure 2-7.
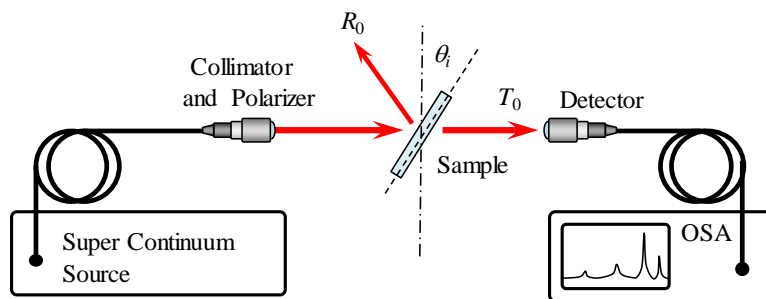
Figure 2-8 Schematic of a general experimental setup used in transmission measurement.
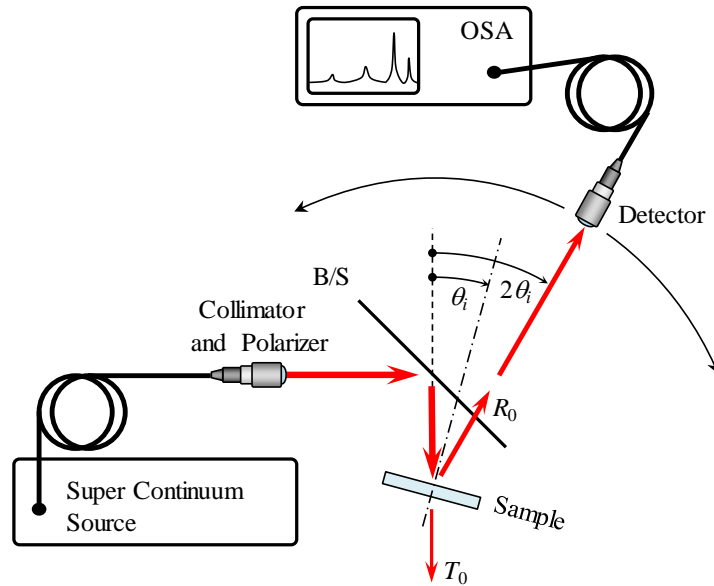
Figure 2-9 Schematic of a general experimental setup used in reflection measurement.

Optical Measurements

Fabricated resonant grating devices are intended to work as bandpass filters, concurrent spatial and spectral filters, and wideband reflectors. Different measurement setups are used to measure device performance, based on device functionality.

Transmission Measurement

Schematic of experimental setup used to measure zero-order transmittance (T_0) is shown in Figure 2-8. The light source is generally a super-continuum light source. The output light is collimated for the desired wavelength. For polarization-dependent measurements, a linear polarizer is used. Transmitted light is collected using a detector and transmitted to an optical spectrum analyzer (OSA) using an optical fiber. Adequate sampling resolution is maintained in the OSA. For T_0 calculation, transmitted signal is normalized by the input. Sample is set on a rotation stage for angular measurements.

Reflection Measurement

Experimental setup for reflection measurement is illustrated in Figure 2-9. Here, a beam-splitter (B/S) is used to collect the reflected signal at the detector. Reference signal for normalization is measured using ~100-nm-thick gold coating that is deposited, through sputtering, on the non-device areas of the sample.

Summary

We discussed different methods that are implemented in developing content for the subsequent chapters. RCWA and FEM based computations are used in our theoretical study. Our device geometry is designed using PSO, a powerful yet effective inverse optimization tool. For device fabrication, we use standard thin-film materials and lithography techniques. We optimize our fabrication processes through characterization using ellipsometry, AFM, and SEM. Finally, we measure and report the performance of the fabricated devices.

Chapter 3

Mode-coupling mechanisms of resonant transmission filters

Nanostructured films with subwavelength periods exhibit guided-mode resonance (GMR) effects enabling applications including wavelength-selective mirrors [10,25] and biochemical sensors [20]. Attendant resonant thin-film lattices constructed with dielectric, metals, or semiconductors support spectral band profiles and local photonic field distributions in great variety. By tailoring multiple leaky modes in desired spectral domains, a host of useful photonic devices and components can be realized [33,35]. In early works, GMR devices operated principally in reflection [8,25,35,36]. In 1995, the first transmission, or bandpass, GMR filters were presented, which were designed with multilayer structures [13]. In subsequent research, Tibuleac et al. provided numerical transmission filter designs in the optical region and experimentally verified their performance in the microwave region [14,37,38]. Kanamori *et al.* reported transmission color filters with broad bandwidths [39]. Sang et al. considered the resonant transmission properties of Ge-based membranes [40]. Furthermore these authors presented mechanically tunable GMR devices by applying a dual membrane structure [41]. Most recently, experimental results have been provided in the telecommunications region near the 1550-nm wavelength [42], in the mid-IR 7- to 14-μm region [43], and in the 3- to 9-μm region [44].

To advance thin-film filter technology, GMR-based bandpass filters are of great interest as they can be seen as being complementary with metallic or multilayer-based systems. Key attributes of high-performance GMR transmission filters include a narrow-

line transmission peak, high efficiency, and low sidebands. We note that designing GMR bandpass filters with broad low-transmission sidebands typically involves parametric optimization because of the optically transparent nature of the thin-film materials.

Initially, GMR transmission filters applied a waveguide grating to create a narrow resonance line with attached high-reflection multilayers to implement broad low-transmission sidebands [13]. More advanced GMR transmission filter designs with only a few thin-film layers and even a single-layer waveguide grating were found using a genetic algorithm [14]. Thus, in 2001, a single-layer transmission filter was presented that resonates at the CO_2 laser wavelength of 10.6 μm and exhibits extensive <1% transmission sidebands spanning 2.21 μm while operating in TE polarization [14]. Corresponding to a part of this low transmission band, there is a 99% flat-reflection band covering 1.91 μm with the relative sideband width generated by this high-reflection band being $\Delta\lambda_R/\lambda_C$ = 18% where λ_C is the center wavelength. As designed, a narrow transmission peak emerges and splits the band in the middle [14]. This wideband high-reflectance/low-transmittance response is not explainable by homogeneous effective thin-film interference. Indeed, a complex modal interaction is involved as Ding and Magnusson identified in their theory of doubly resonant GMR bandpass filters [16]. Considering the versatile governing physics and substantial parametric design space associated with this device class, a host of unexplored aspects remains.

Accordingly, in this chapter, we investigate the modal coupling mechanisms of key resonant bandpass-filter architectures in a quest to uncover new high-performance devices in this class. These include a single-layer binary Ge-Se waveguide grating, a two-layer partially etched Si grating structure, and a three-layer embedded Si waveguide

23
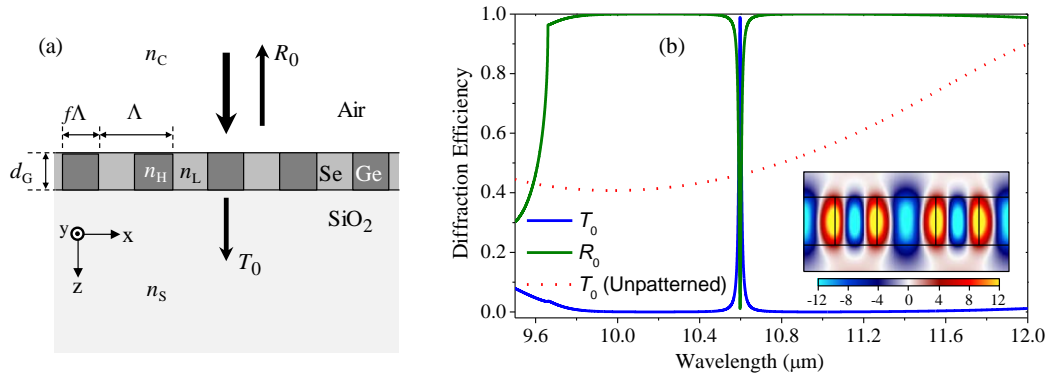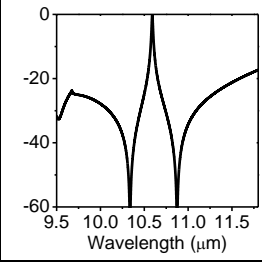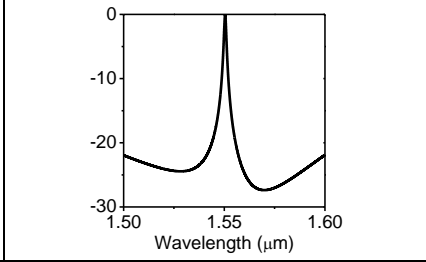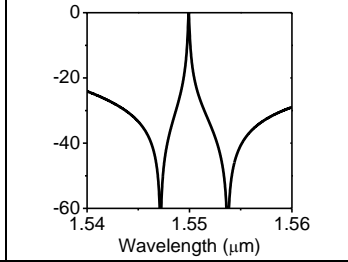
Figure 3-1 Ge-Se single layer device. (a) Device schematic and (b) spectral performance of a single-layer GMR bandpass filter with period $\Lambda = 6.91$ μm, fill factor $f = 0.42$, and grating thickness $d_G = 3.8$ μm. Refractive indices are $n_C = 1$ (air), $n_S = 1.4$ (SiO$_2$), $n_H = 4$ (Ge), and $n_L = 2.64$ (Se). T_0 and R_0 denote the zero-order transmittance and zero-order reflectance, respectively. The dashed line in (b) represents the optical response for the grating layer replaced with the effective homogeneous layer. The inset in (b) shows the distribution of the total electric field over 2Λ at the T_0-peak wavelength. The TE polarization state prevails.

structure. We show that devices with experimentally realistic geometric parameters can be designed to yield flat low-transmission sidebands with bandwidths ranging from ~40 nm to ~2100 nm and sharp transmission peaks with full-width at half-maximum (FWHM) linewidths ranging from ~1 pm to ~10 nm in the mid- and near-infrared spectral domains. We introduce a systematic method to achieve a practical transmission profile with an arbitrarily narrow pass bandwidth.

Device 1: Ge-Se single-layer device

The first device is a single-layer waveguide grating structure similar to the one presented in [14]. The device schematic and diffraction spectra are illustrated in Figures 3-1(a) and 3-1(b), respectively. We use rigorous coupled-wave analysis [29] for the numerical calculations. We excite the device with a TE-polarized plane wave under normal incidence; transverse-electric polarization refers to the electric field vector of the incident wave being normal to the plane of incidence and parallel to the grating lines.

Table 3–1 List of Performance Parameters for the Three Devices Treated

Performance Parameters	Device 1 Figure 3-1	Device 2 Figure 3-4	Device 3 Figure 3-7	Ding *et al.* [16]
Resonance Wavelength (λ_C)	10.6 μm	1.55 μm	1.55 μm	1.55 μm
Pass Bandwidth ($\Delta\lambda_{pass}$)	14 nm	1 nm	0.1 nm	2 nm
Side Bandwidth ($\Delta\lambda_{side}$)	2165 nm	122 nm	38 nm	126 nm
Relative Pass Bandwidth ($\Delta\lambda_{pass}/\lambda_C$)	0.132%	0.0645%	0.00645%	0.129%
Relative Side Bandwidth ($\Delta\lambda_{side}/\lambda_C$)	20.42%	7.87%	2.45%	8.13%
Pass to Side Bandwidth Ratio ($\Delta\lambda_{pass}/\Delta\lambda_{side}$)	0.65%	0.82%	0.26%	1.59%
Resonance Q factor ($\lambda_C/\Delta\lambda_{pass}$)	757	1550	15500	775
Log(T_0) profile on a dB scale				
Device 1	Device 2		Device 3	

In Figure 3-1(b), the high-reflection band shown with R_0>99% covers 2.165 μm or 20.4%. In this case, the low sidebands are entirely generated by the high-reflectance band. This was not the case in [14] as discussed above, since propagating ±1 diffraction orders below the Rayleigh wavelength aided the device performance; there the R_0>99% band provided ~86% of the low band. Other performance parameters for this device are summarized in Table 3–1. Note that the side bandwidth is defined as $T_0 \leq 1\%$.

The total electric field distribution at the T_0 peak wavelength of 10.6 μm shown in the inset of Figure 3-1(b) indicates that the transmission peak arises from a second order

coupling to the TE_0 mode. As clearly revealed by the totally different response (red dotted curve) of an effective-medium homogeneous film, the low-transmission band is attributed to the broadband multiple-resonance effect rather than homogeneous thin-film interference. In the subwavelength region, a rectangular grating layer such as that in Figure 3-1(a) may be approximately modeled as a homogeneous negative uniaxial layer with an ordinary index of refraction, corresponding to TE polarization, given by

$$n_O = \left[n_L^2 + f \left(n_H^2 - n_L^2 \right) \right]^{1/2}. \tag{3.1}$$

In this computation, the periodic film is replaced by a film with refractive index thus found.

Figure 3-2 Amplitudes of different coupling orders at different wavelengths. (a) 9.80 μm, (b) 10.40 μm, (c) 10.59 μm, (d) 10.60 μm, (e) 10.65 μm and (f) 11.20 μm. S_0 (green line), $S_{\pm1}$ (blue line), and $S_{\pm2}$ (red line) represent the zero-, first-, and second-order amplitudes, respectively. The inset on the right-top side of each plot indicates the corresponding wavelength with respect to the transmission spectrum.

Modal study

We identify the resonant modes responsible for the flat sidebands by computing the amplitudes of the coupling orders for various wavelengths as summarized in Figure 3-2. To place this in context, we recall that the y-component of the electric field in the grating in Figure 3-1 can be expressed as [26]

$$E_y(x,z) = \sum_q S_q(z)\exp(-i\boldsymbol{\sigma}_q \cdot \mathbf{r}),$$

(3.2)

where $\boldsymbol{\rho}_q = \boldsymbol{\rho} - q\mathbf{K}$ with $\boldsymbol{\rho}$ being the wave vector of the refracted input wave, $\mathbf{K}$ is the grating vector with magnitude $K = 2\pi/\Lambda$, and $\mathbf{r} = (x,z)$ is the position vector. This is the coupled-wave expression for the internal field where the S_q is the amplitude of the q-th space harmonic in the inhomogeneous plane-wave expansion; Figure 3-2 displays these amplitudes. At $\lambda = 9.8$ μm as shown in Figure 3–2(a), we observe simultaneous first- and second-order coupling to a TE$_2$-type mode. The zero-order propagating wave, with amplitude S_0, is efficiently reflected with resulting peak amplitude of 2 as there is a standing wave in the input half-space. The dominant contribution to the internal modal field is due to the evanescent diffraction orders with amplitudes $S_{\pm 1}$ as seen in Figure 3–2(a). In Figure 3–2(b), the $S_{\pm 2}$ contribution morphs into a TE$_0$-like distribution; further variations are observed in Figure 3–2(c) at the 50% transmittance wavelength on the short-wavelength side. Generally, the amplitudes of the first and second diffraction orders grow as the wavelength approaches the T_0 peak. In Figure 3–2(d), the second-order coupling amplitude far exceeds that of the first order and the distribution is in the shape of a TE$_0$ mode; note that the transmitted zero-order amplitude is near unity, consistent with Figure 3-1. For the longer wavelength range, the amplitudes of the first and second orders

27
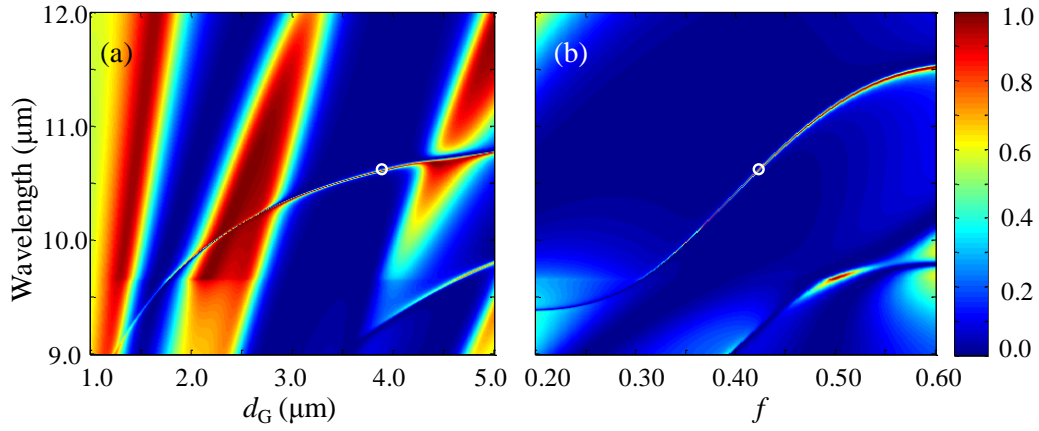
Figure 3-3 T_0 spectrum as a function of (a) grating thickness (d_G) and (b) fill factor (f) of the device in Figure 3-1(a). The white circles correspond to the filter in Figure 3-1.

decrease as shown in Figure 3–2(e). At λ = 11.2 μm, the first order has a typical TE_2 mode character whereas the second order dominantly couples to a TE_1-like mode as shown in Figure 3–2(f).

In summary, TE_2 and TE_1 types of modes under first- and second-order coupling are involved in the formation of Figure 3–1's flat low-transmission sidebands, and a TE_0 mode under dominant second-order coupling induces the narrow T_0 peak in this design. This coupling configuration expresses the detailed modal properties of the doubly resonant bandpass filters proposed by Ding and Magnusson [16].

Parametric study

Figure 3-3 shows the variation of transmittance relative to key parameters. The grating layer thickness controls both the location of the transmission peak and the sidebands as shown in Figure 3–3(a). In Figure 3–3(b), the sideband properties are insensitive to the grating fill factor while the peak wavelength is highly dependent upon it. Therefore, by controlling the fill factor, the peak wavelength can be finely tuned without a significant effect on the sideband properties.
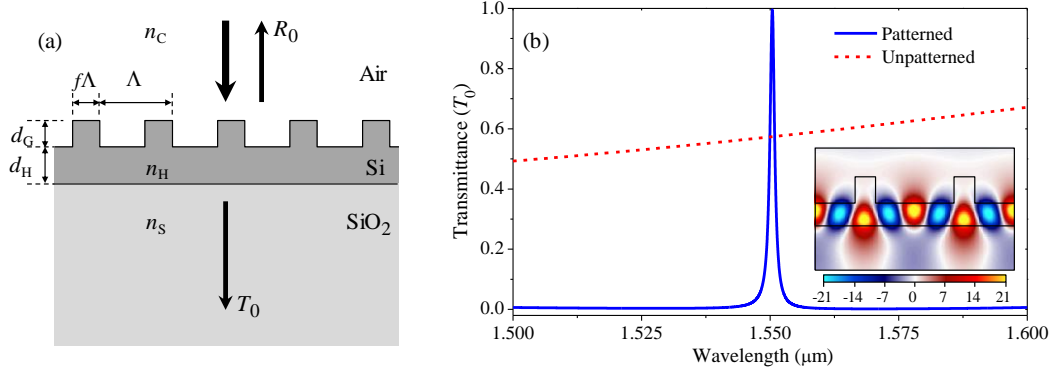
Figure 3-4 Partially etched Si thin-film device. Structure and (b) performance spectrum of a Si-based GMR bandpass filter with the following parameters: grating period Λ = 1.018 μm, fill factor f = 0.21, grating thickness d_G = 0.355 μm, and homogeneous sublayer thickness d_H = 0.297 μm. Refractive indices are n_C = 1 (air), n_S = 1.45 (SiO₂), and n_H = 3.48 (Si). The dashed line in (b) represents the optical response with the grating layer replaced with an effective homogeneous layer. The inset in (b) shows the total electric field at the T_0-peak wavelength.

Device 2: Partially etched Si thin-film device

The second device architecture studied is a partially etched single-layer structure. In this device, the grating ridges match identically to the underlying homogeneous layer made of the same material such that no reflections or phase changes arise upon transition from the grating ridge into the layer. We call this structure a "zero-contrast" grating [18] in distinction to a high-contrast grating [45]. This structure is highly favorable for standard mask-based nanofabrication processes. The film medium is Si, and the device structure and T_0 spectrum are presented in Figure 3–4; Table 2.1 lists the performance parameters.

The total electric field at the T_0-peak wavelength in Figure 3–4(b) arises dominantly from the second-order coupling to a TE₀ mode in the homogeneous sublayer. The vertical oscillation of the field maxima in the sublayer is a result of interference between a TE₀ mode under the second-order coupling and a TE₁ mode at first-order coupling as shown in Figure 3-5(c). The low-transmission sideband is again, as in Figures
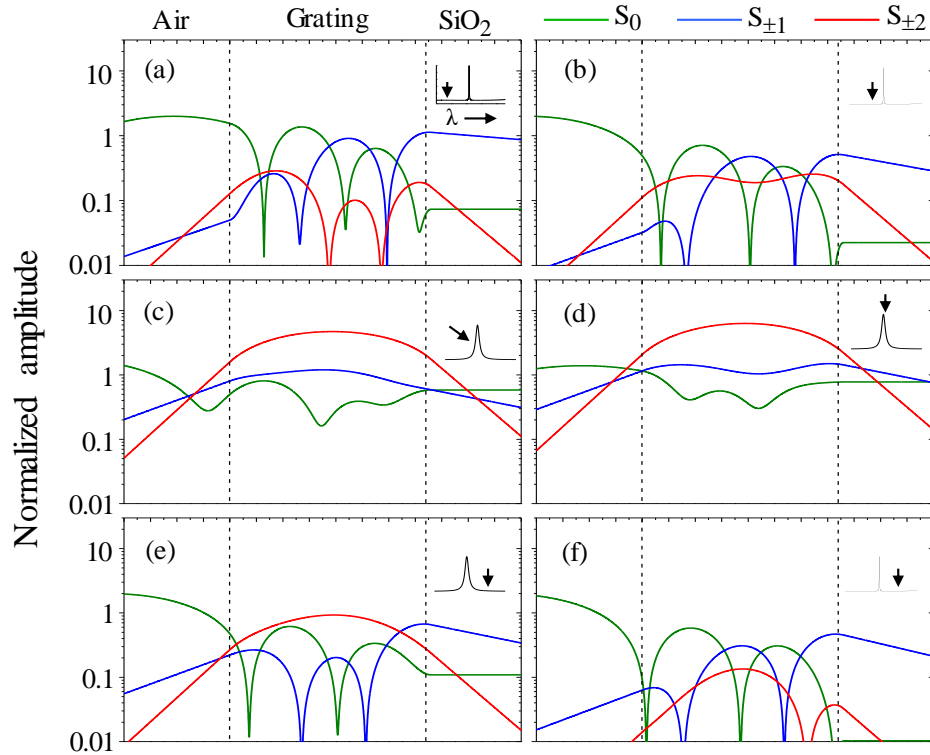
Figure 3-5 Amplitudes of coupling orders at different wavelengths. (a) 1.50 μm, (b) 1.545 μm, (c) 1.549 μm, (d) 1.55 μm, (e) 1.552 μm and (f) 1.6 μm. S_0 (green line), $S_{\pm1}$ (blue line), and $S_{\pm2}$ (red line) represent the zero-, first-, and second-order amplitudes, respectively. The inset in each plot indicates the corresponding wavelength with respect to the transmission spectrum.

3-1 and 3–2, attributed to the broadband multiple-resonance effect rather than homogeneous thin-film interference as the effective homogeneous film shows a totally different response (red dotted curve) than the patterned device.

Modal study

To identify the operative modes responsible for the flat sidebands and resonant peak, we compute amplitudes of coupling orders at different wavelengths ranging from 1.5 μm to 1.6 μm. Figures 3–5(a)-(f) show the amplitudes at different wavelengths in increasing order. In the short wavelength range, for example at λ = 1.5 μm in Figure 3–5(a),
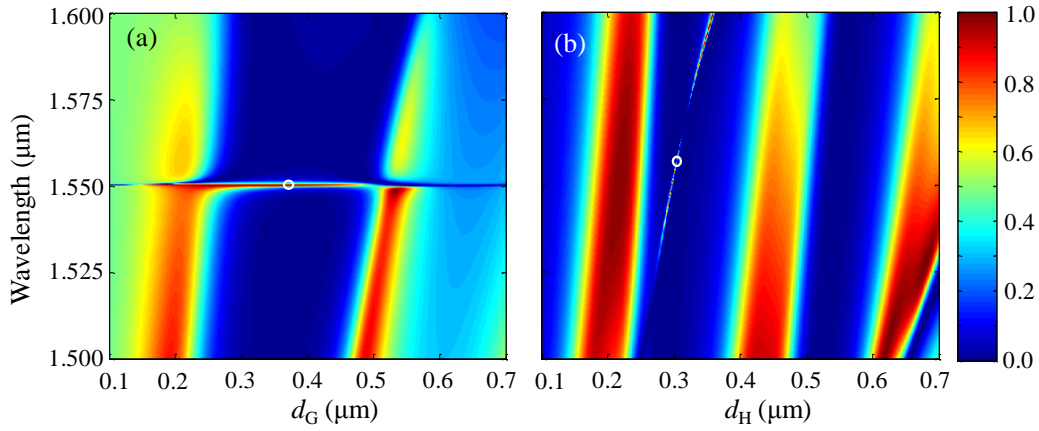
Figure 3-6 T_0 spectrum as a function of (a) grating layer thickness and (b) homogeneous layer thickness. The white circles in (a) and (b) denote the device parameters.

the dominant modes associated with excitation by the first and second evanescent diffraction orders, respectively, are TE_2 and TE_1 modes with classic mode shapes. For the first order, the excited mode has a significant amplitude in both the Si grating and homogeneous sublayer. In Figure 3–5(b) for the longer wavelength $\lambda = 1.545$ µm, the amplitudes of both the first and second orders increase. The increase in the second-order amplitude is attributed to the coupling to a TE_0 type mode. At the T_0-peak, at wavelength of 1.55 µm, the second-order coupling gains dominance involving a TE_0 mode and the first-order coupling is reduced to a TE_1 mode. For wavelengths exceeding the T_0-peak wavelength, the first and second order amplitudes decrease as shown in Figures 3–5(e) and 3–5(f). In Figure 3–5(f) for $\lambda = 1.6$ µm, a TE_2 mode becomes dominant for the first-order coupling and the second order couples to a TE_1 mode; this is similar to the coupled mode configuration for $\lambda = 1.5$ µm shown in Figure 3–5(c). Like the single-layer Device 1, this device exhibits the double resonance mode configuration in [16]. In contrast to the single-layer device, however, the second-order excitation in this partially etched two-layer device involves TE_1 excitation for the formation of the broad low transmission sidebands.

31

Parametric study

In contrast to the single-layer device, the partially etched thin-film, single-layer Si architecture provides better controllability in parametric tuning of the spectral profile. Figure 3–6 shows the T_0 spectrum as a function of the grating and homogeneous Si layer thickness. In Figure 3–6(a), the sidebands and resonance wavelength are tolerant against significant changes in the grating layer thickness because the mode responsible for the narrow transmission peak dominantly resides in the homogeneous sublayer. Therefore, the homogeneous Si layer thickness has a significant impact on both the sidebands and the resonance position as shown in Figure 3–6(b). Also in Figure 3–6(b), we observe alternating low and high transmission bands with increasing homogeneous Si layer thickness. These low transmission bands can accommodate a transmission peak with appropriate sets of geometrical parameters.

Device 3: Three-layer embedded Si-waveguide device

The final device architecture under study is a three-layer structure consisting of a low-index cladding layer between the high-index grating and waveguide layers as reported by Tibuleac *et al*. [14]. The device structure and its T_0 spectrum are presented in Figure 3–7, and the performance parameters for this device are listed in Table 3–1.

Modal study

The field pattern in Figure 3–7(b)'s inset shows a TE_8 mode structure excited by first-order diffraction at the T_0 peak wavelength. To identify the resonance modes responsible for the flat sidebands, we again compute the amplitudes of coupling orders at example wavelengths; the results are presented in Figure 3–8. The flat sideband in the shorter wavelength range is attributed to the excitation of a TE_9 mode coupling [46] with

32
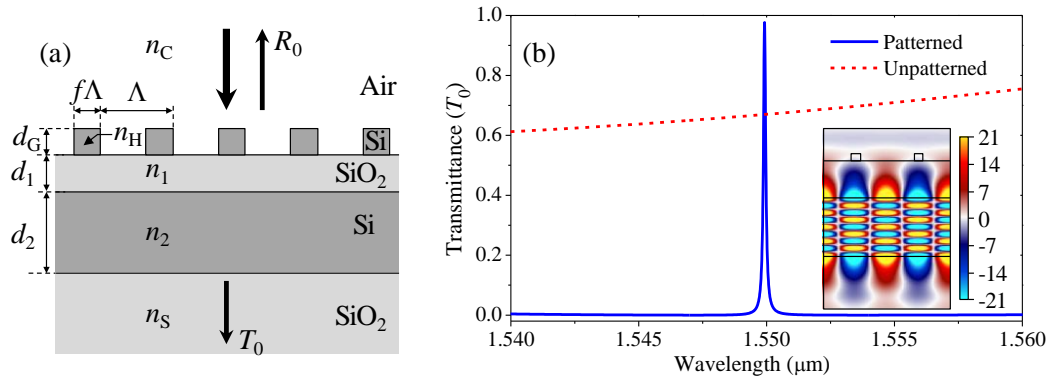
Figure 3-7 Three-layer embedded Si-waveguide device. (a) Structure and (b) T_0 spectrum of the three-layer GMR transmission filter with the optimized parameters of grating period $\Lambda = 1.029$ μm, fill factor $f = 0.152$, grating thickness $d_G = 0.262$ μm, upper cladding thickness $d_1 = 1.460$ μm, and embedded Si waveguide thickness $d_2 = 2.221$ μm. Refractive indices are $n_C = 1$ (air), $n_S = n_1 = 1.45$ (SiO$_2$), and $n_H = n_2 = 3.2$ (Si). The dashed line in (b) represents the optical response for the grating layer replaced with the effective homogeneous layer. The inset in (b) shows the total electric field at the T_0-peak wavelength.

the evanescent first orders as shown in Figures 3–8(a)-(c). The first node of the TE$_9$ mode is located in the homogeneous SiO$_2$ layer while the remaining eight nodes are located in the homogeneous Si layer. As the wavelength increases from 1.5470 nm to 1.5496 nm, the location of the first node in the homogeneous SiO$_2$ layer shifts toward the grating layer and the mode's amplitude in the homogeneous Si layer increases as shown in Figures 3–8(a)-(c). At the peak wavelength $\lambda = 1.550$ nm, the first node in the homogeneous SiO$_2$ layer is completely pushed out of the device as shown in Figure 3–8(d). Therefore, the mode morphs from TE$_9$ to TE$_8$, forming the flat sidebands and the narrow T_0 peak; at longer wavelengths, the relative size of the structure is smaller and cannot support the higher modes. For longer wavelengths, the amplitude of the first-order coupled TE$_8$ mode is operative continuously and decreases with wavelength as shown in Figures 3–8(e) and 3–8(f).

The operation of this device proceeds with a mechanism different from that in [16]. Figure 3–8 clearly shows how spectral metamorphosis of the multiple modes forms the
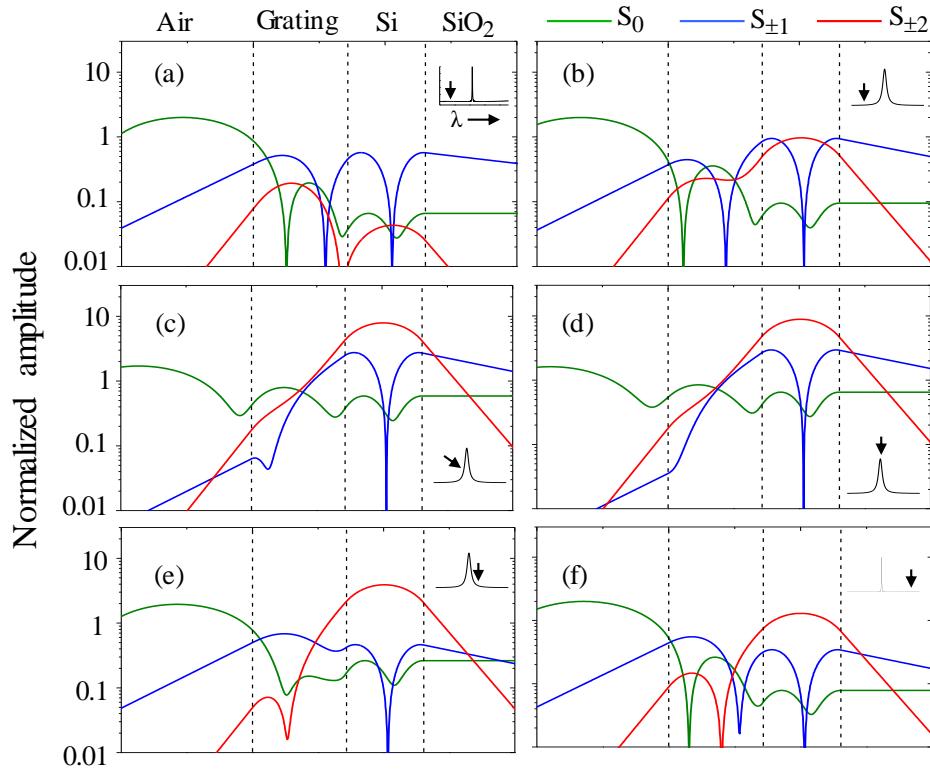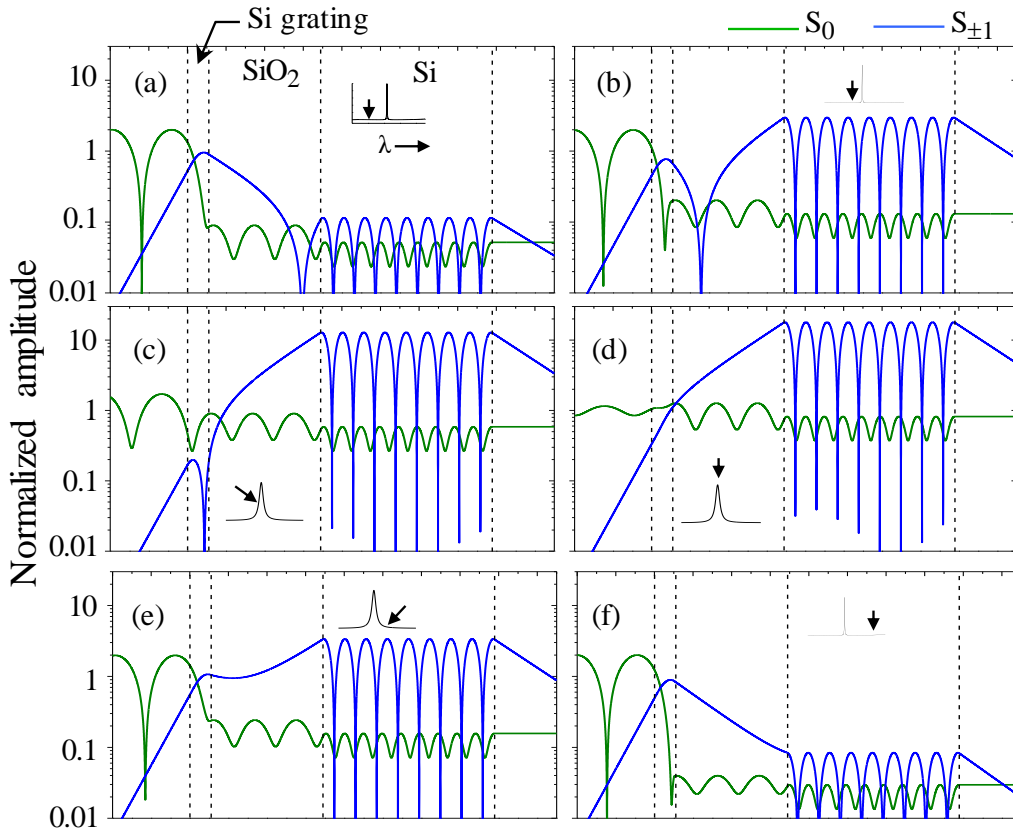
Figure 3-8 Amplitudes of the main coupling orders at different wavelengths. (a) 1.5470 μm, (b) 1.5496 μm, (c) 1.5499 μm, (d) 1.55 μm, (e) 1.5502 μm, and (f) 1.5600 μm. S_0 (green line) and $S_{\pm1}$ (blue line) represent the zero- and first-order amplitudes, respectively. The inset in each plot indicates the corresponding wavelength with respect to the transmission spectrum.

broad sidebands and the narrow transmission peak. In Figures 3–8(a)-(f), the relative field amplitude of the dominant mode (blue curves) in the top grating layer first decreases with wavelength, then becomes maximal at the peak wavelength, and finally decreases again for the longer wavelength range. The coupled mode in the low-transmission sidebands has strong diffractive leakage to the outside radiation as it has a large overlap in the diffraction grating layer as demonstrated in Figures 3–8(a) and 3–8(f). The broadband resonance feature providing the low-transmission sidebands is a natural consequence of the
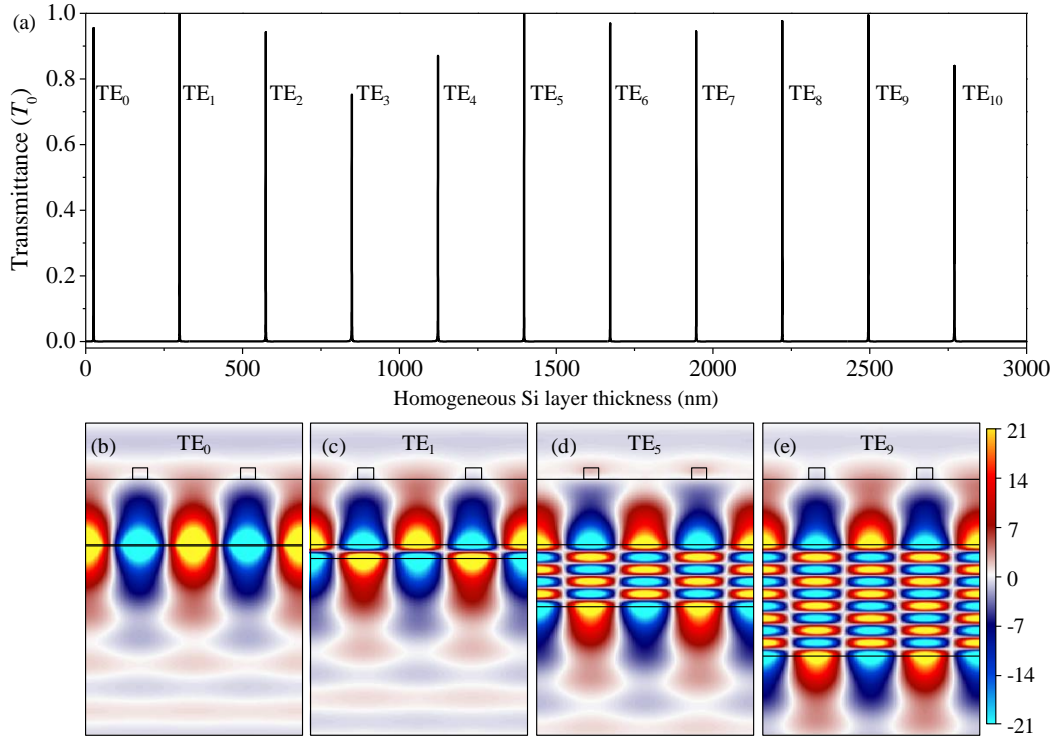
Figure 3-9 Spectral dependence on homogeneous Si layer thickness. (a) Zero-order transmittance for different values of homogeneous Si layer thickness (d_2) at Λ = 1.550 µm and total field at T_0 peak wavelength when the homogeneous Si layer thickness is: (b) d_2 = 0.025 µm operating at TE_0 mode, (c) d_2 = 0.300 µm operating at TE_1 mode, (d) d_2 = 1.398 µm operating at TE_4 mode, and (e) d_2 = 2.495 µm operating at TE_9 mode.

excitation of a short lived, highly leaky mode. In contrast, the coupled mode at the T_0 peak has a small overlap with the grating layer and, thereby, has a long lifetime causing the narrow spectral resonance shown.

Parametric study

Interestingly, over the former two device structures, this design has remarkable advantages in controlling major spectral properties and internal field patterns. At a fixed wavelength of 1.55 µm, when the thickness of the waveguide layer increases from 0 to 3000 nm, we observe 11 discrete transmission states as shown in Figure 3–9(a). Each resonant state corresponds to a different coupled guided mode from TE_0 to TE_{10}. Figures 3–9(b)-(e)

show electric field patterns associated with several selected transmission peaks in Figure 3–9(a). For example, the first occurrence of such a transmission state is at a thickness of 25 nm. The total field at the T_0 peak wavelength for a 25-nm thick waveguide layer shows a first-order coupling to a TE_0 mode as shown in Figure 3–9(b). The T_0 spectrum for the 25-nm thick waveguide layer operating in a TE_0 mode state is shown in Figure 3–9(a). A series of transmission peaks appears with 274-nm spacing in the homogeneous Si waveguide layer thickness without significantly changing the low-transmission sideband properties. The total field plots at the T_0-peak wavelengths for different transmission states exhibit similar characteristics. Figures 3–9(b)-(e) show that the amplitudes of total fields across the devices with different waveguide layer thicknesses are similar. The fields in the grating layer and in the homogeneous SiO_2 cladding are comparable and, to an extent, independent of the field distribution in the waveguide layer. In Figures 3–8(a)-(f), the amplitudes of all 8 nodes in the waveguide layer are constant for a given wavelength. Thus, with every 274-nm increase (or decrease) in waveguide layer thickness, the field configuration meets the boundary conditions for excitation by a higher- (or lower-) order mode at the fixed wavelength of 1550 nm in this example. We note that the free spectral range in thickness computed numerically in Figure 3–9(a) is consistent with an approximate expression given previously [25]; for the present case this formula is

$$\Delta d = 0.5\lambda [n_2{}^2 - (q\lambda/\Lambda)^2]^{-1/2}. \tag{3.3}$$

The peak linewidth and side bandwidth for the TE_{0-10} modes are plotted in Figure 3–10(a). The T_0 peak linewidth is generally narrower for a thicker waveguide as shown in the same figure; this is because the added optical path in the thicker waveguide leads to a longer resonance lifetime. Moreover, in Figure 3–10(a), the change in waveguide thickness
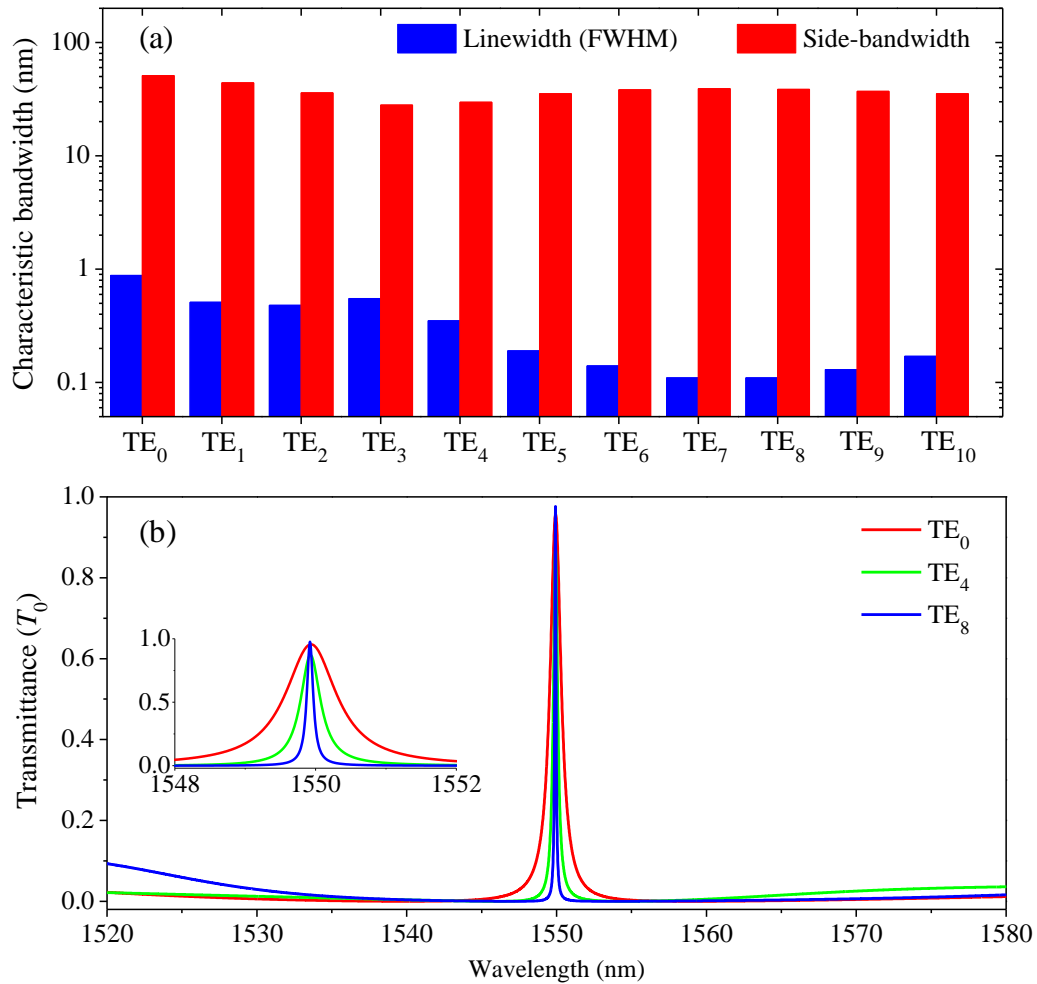
Figure 3-10 Side-bandwidth and linewidth analysis. (a) Characteristic bandwidths and (b) selected T_0 spectra of transmission peaks in Figure 3–9(a). Inset in (b) provides passband comparison for the selected transmission states.

does not have a significant impact on the level or bandwidth of the low-transmission sidebands as the sideband property is dominantly determined by the top grating patterns as observed in Figure 3–7(b). The transmittance spectra for TE_0, TE_4, and TE_8 modes plotted in Figure 3–10(b) show the decreasing T_0 peak linewidth for the higher-order mode while their side bandwidths are comparable.
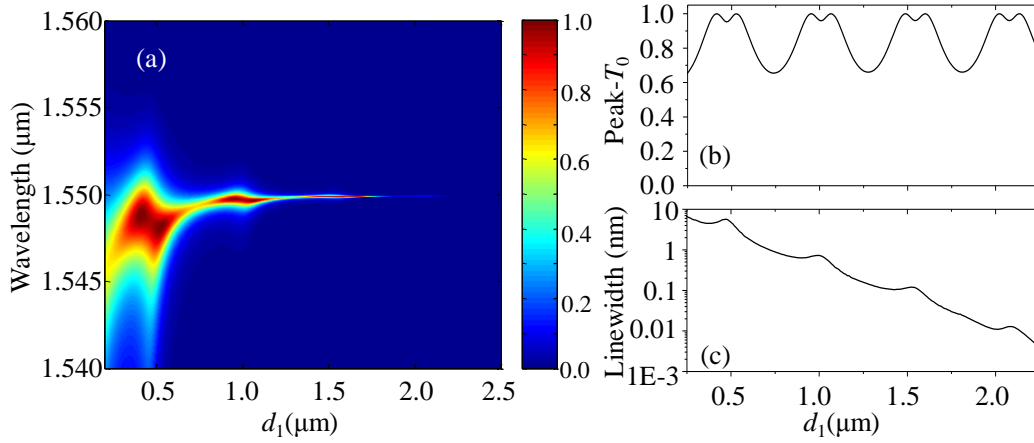
Figure 3-11 (a) T_0 spectrum, (b) peak efficiency, and (c) peak linewidth (FWHM) as functions of homogeneous SiO_2 layer thickness (d_1).

We proceed to further study the interesting physical properties provided by the homogeneous SiO_2 upper cladding layer. The T_0 spectrum is shown as a function of the SiO_2 layer thickness in Figure 3–11(a); the transmission peak location asymptotically increases, settling at 1550 nm for the SiO_2 layer thickness larger than 1 μm. Figures 3–11(b) and 3–11(c) show the dependence of the T_0 peak efficiency and linewidth, respectively, as functions of the SiO_2 layer thickness. The bandwidth of the transmission peak exhibits exponential decay as the thickness increases. The increase in thickness, however, has no effect on the sideband properties as observable in Figure 3–11(a). The T_0 peak efficiency shows a recurring pattern with thickness. The recurrence has a 534-nm period in the homogeneous SiO_2 layer thickness, and this value corresponds to the half wavelength ($\lambda/2n_1$) in SiO_2. Therefore, this particular property is related to a weak Fabry-Perot (FP) resonance in the homogeneous SiO_2 layer. In more detail, fields in the grating layer can be enhanced with the FP resonance in the SiO_2 layer, and the enhancement increases the radiation probability to the cover as evidenced by local peaks in the linewidth in Figure 3–11(c). In addition, the recurring double peaks in the FP undulation in Figure 3–11(b) may

Table 3-2 Mode Configurations Discussed in the Chapter

Location	Device 1 Figure 3-2	Device 2 Figure 3-4	Device 3 Figure 3-8	Ding et al. [16]
Left Sideband	**$TE_{1,2}$** $TE_{2,2}$	**$TE_{1,2}$** $TE_{2,1}$	$TE_{1,9}$	$TE_{1,2}$
T-Peak	$TE_{1,0}$ **$TE_{2,0}$**	$TE_{1,1}$ **$TE_{2,0}$**	$TE_{1,8}$	$TE_{2,0}$
Right Sideband	**$TE_{1,2}$** $TE_{2,1}$	**$TE_{1,2}$** $TE_{2,1}$	$TE_{1,8}$	$TE_{1,2}$
NOTE: The modes are listed in $TE_{m.n}$ format where m represents the coupling order and n represents the coupling mode. In each case, the mode in bold text represents the mode with higher amplitude.				

be explained by the association of the T_0-peak efficiency with radiation probabilities to the cover and substrate [47,48]. This unique feature allows for transmission peaks with infinitesimal bandwidth while maintaining broad, flat sidebands.

Conclusions

Table 3–1 summarizes the performance parameters for the three device architectures analyzed in comparison with the device studied in [16]. These performance parameters are supported by the different mode-coupling configurations as listed in Table 3–2. The device analyzed in [16] is a single-layer device with binary gratings similar in structure to Device 2 in this analysis. The bandpass property in both device designs arises from the double-resonance GMR effect. The partially etched Si device here shows different modal configurations with an additional leaky mode contributing to the formation of the low transmission sidebands. In the three-layer embedded Si-waveguide device, the operative mode morphs from one guided mode (TE_n) to the neighboring guided mode (TE_{n-1}) stimulated by the same evanescent diffraction order. The narrow transmission peak is obtained upon the spectral mode transition.

In summary, we study the modal properties of three GMR bandpass filter designs. We show that the broad low-transmission sidebands and narrow transmission peak with high efficiency approaching 100% can be obtained by appropriately blending multiple guided modes for a variety of thin-film grating structures based on all-transparent materials. More specifically, the single-layer binary grating structure consisting of Ge and Se yields bandpass filter performance in the mid-infrared spectral domain under the simultaneous excitations of the TE_1 and TE_2 modes for the broad low-transmission sidebands and the TE_0 mode for the narrow transmission peak. For the partially etched Si grating structure in the optical communication band, a mixture of TE_1 and TE_2 modes contributes to form the broad low-transmission sidebands while the narrow transmission peak is induced by a combination of TE_0 and TE_1 modes with different coupling orders. The final three-layer device consists of a top Si grating, SiO_2 upper cladding, and an un-patterned Si slab waveguide. In this structure, any combination of TE_n and TE_{n+1} modes generates a spectral profile for a bandpass filter provided by an appropriate layer thickness. These modal properties provide novel design principles for GMR bandpass filters with narrow peak bandwidths, high efficiency, and low-transmission flat sidebands in a desired spectral domain.

Chapter 4

Single-layer optical bandpass filter technology

Thin-film optics is a mature technological area. Multilayer dielectric films are widely applied to implement metal-free and thus low-loss filters, polarizers, and reflectors for incorporation in common optical systems [49]. These devices typically consist of stacks of homogeneous layers deposited with precise thicknesses and tight control of index of refraction and absorption. A large number of layers, perhaps ~10–100, may be needed to create the spectral, polarization, and angular attributes required for a particular application. These optical devices operate on the basis of multiple reflections between the interfaces incorporated in a layered stack. In particular, periodic quarter-wave layer systems provide classical high reflectors for bulk laser cavities as well as integrated distributed Bragg reflectors for vertical cavity lasers [50]. Embedding a half-wave spacer layer between two reflector film stacks enables formation of a passband centered at the design wavelength [49]. This passband is the functional basis for commercial bandpass filters operating in the visible and near-infrared spectral domains with applications in telecommunications, laser-line filtering, astronomical observations, and spectroscopic and analytical instrumentation.

Resonant thin-film subwavelength gratings enable versatile optical properties for reflectors [18,51,52], spectral filters [53,54], and beam-transforming elements [55]. On account of this structural simplicity and on-chip integration compatibility, it is of interest to develop high-performance bandpass filters with flat, low sidebands and narrow, high-efficiency passbands using analogous architectures. Previous related work has mostly

focused on theoretical design and explanation of the underlying physics [14,15,56]. In an early proposal, quarter-wave Bragg stacks are used to generate broad stopbands accommodating narrow transmission peaks induced by resonant subwavelength gratings [56]. Practical designs with a single, or a few, thin-film layers have been found using inverse numerical optimization methods [14,15]. In these advanced designs, multiple leaky resonant modes with low-Q and high-Q resonance properties are forced to cooperate in a single nanopatterned layer to generate a desired spectral response [16]. A recent theoretical study in this context shows that near-unity peak efficiency and arbitrarily-narrow linewidth at a desired spectral location are attainable with partially etched single-layer grating architectures even at normal incidence [57].

Experimental demonstration of resonant bandpass, or transmission, filters has been attempted by only a few groups [39,42,43]. Kanamori *et al.* fabricated color filters with efficiencies in the range of ~55-70% but with very wide bandwidths ~100 nm and without suppression of the sidebands [39]. Foley *et al.* reported transmission resonance with passband efficiency ~35% and a broad peak bandwidth exceeding 500 nm in the mid-infrared domain; these devices operated only under off-normal incidence [43]. In another experimental demonstration, Amin *et al.* provided a Rayleigh-anomaly-assisted transmission filter with ~50% efficiency in the near-infrared domain; however, this design lacks the flat, low stopbands and well-defined narrow passband that are critical in practice [42].

In this chapter, we report successful design, fabrication, and measurement of high-performance bandpass filters in the telecommunications band using single-layer resonant Si gratings. We obtain an ultra-narrow passband with peak efficiency ~72% and linewidth

~0.48 nm with attendant 100-nm-wide flat stopbands that lie below 1% in transmittance. These performance parameters satisfy requirements pertinent to wavelength-division multiplexing under the International Telecommunication Union standards [58]. The filter passband is supported by a high-quality guided-mode resonance whose operating wavelength is adjustable by tuning the angle of incidence of the input beam. These results demonstrate the feasibility of the proposed device class for bandpass filtering applications.

Device structure

We apply a single-layer resonant thin-film grating structure on a silicon-on-quartz (SOQ) platform as shown in Figure 4–1(a) in comparison with a classical multilayer structure in Figure 4–1(b) fashioned with the same native materials. The proposed single-layer structure has a crystalline-silicon (c-Si) film of thickness t on a quartz substrate with refractive index n_S = 1.51. The top c-Si film is in the x-y plane and contains a one-dimensional grating with period Λ. The grating grooves lie along the y-axis. The width and height of a grating ridge is $f\Lambda$ and d_G, respectively. We optimize these parameters using the particle swarm optimization (PSO) method [15] to generate the desired bandpass filtering functionality under normally-incident transverse-electric (TE) polarized light in the telecommunications band around vacuum wavelength of 1300 nm. TE-polarized input light has its electric-field vector along the grating-ridge axis (y-axis). The rigorous coupled-wave analysis (RCWA) [29] is used as a forward kernel in the parametric optimization code. We model the c-Si film with its refractive index 3.48 which is experimentally obtained by ellipsometry. We note that the extinction coefficient of the c-Si is ~10^{-6} and is therefore negligible in the numerical calculations.
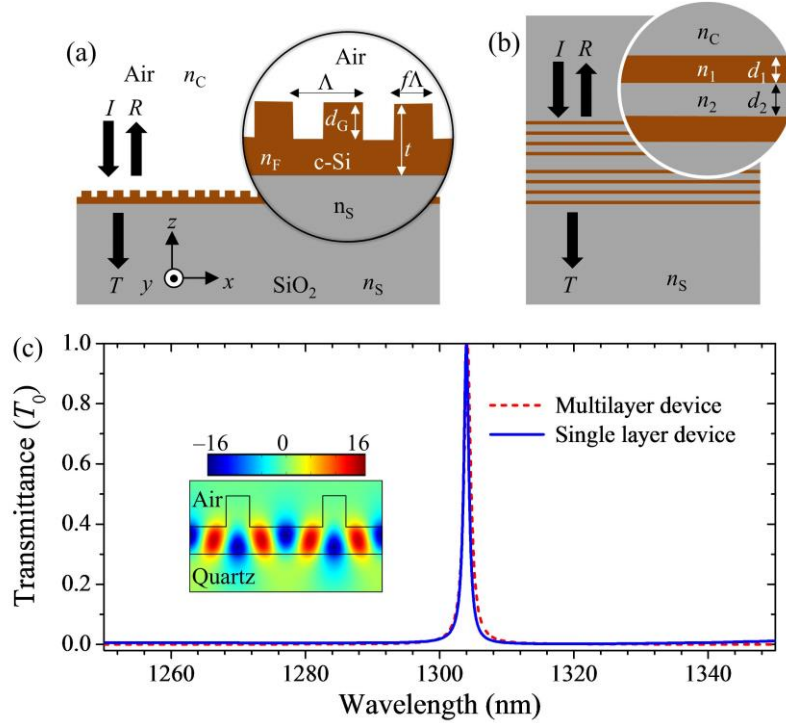
Figure 4-1 Performance of a single-layer resonant bandpass filter in comparison with a traditional multilayer device. (a) Structure of a nanopatterned single-layer device. The device parameters are: refractive indices n_C = 1.0 (Air), n_F = 3.48 (Si), n_S = 1.51 (SiO$_2$); film thicknesses t = 520 nm and d_G = 277 nm; period Λ = 860 nm; and fill factor f = 0.24. (b) Structure of a 15-layer traditional bandpass filter with indices n_1 = 3.48 (Si), n_2 = 1.51 (SiO$_2$), and n_C = n_S = 1.51 (SiO$_2$). The corresponding quarter-wave thicknesses are d_1 = 93.7 nm and d_2 = 215.9 nm. Layer 8 from the top has a half-wave thickness of 431.8 nm. (c) Calculated zero-order transmittance (T_0) of the nanopatterned single-layer device in comparison with the multilayer device. We assume TE-polarized light at normal incidence. The inset in (c) shows the electric field distribution at the peak wavelength λ = 1304 nm. The color scale is normalized by the incident electric-field amplitude.

Parametric optimization using the PSO method yields the zero-order transmittance (T_0) spectrum shown in Figure 4–1(c). The optimized parameters are given in the figure caption. The T_0 spectrum has a passband with peak efficiency 99.8% and full-width at half-maximum (FWHM) linewidth $\Delta\lambda$ = 0.9 nm centered at λ = 1304 nm. The normalized electric field (E_y) distribution at λ = 1304 nm shown in the inset of Figure 4–1(c) confirms that resonant coupling to the fundamental mode (TE$_0$) is responsible for the

formation of the sharp transmission peak. The high-intensity fields associated with the standing TE_0 mode excitation are strongly confined in the homogeneous portion of the c-Si layer. Thus, the device performance is robust against minor parametric variations in the top patterned region [57]. The flat stopbands have $T_0 \leq 1\%$ over a 100-nm-wide wavelength range spanning from 1250 nm to 1350 nm. This remarkable stopband formation by a single nanopatterned c-Si layer is supported by a *resonant* broadband reflection effect and not a *thin-film interference* effect as explained in a recent study [57]. There, Niraula *et al.* show that the partially etched grating device operates under a combination of two resonant modes: a low-Q TE_1 mode that forms the wide, flat stopband and a high-Q TE_0 mode that forms the narrow passband within the wide stopband. Fundamentally, as shown in detail in Figure 4 of ref. [16], the classic asymmetrical resonance line shape contains a reflection null and a peak for an unoptimized resonant grating. The null persists in spite of parametric variations that raise the reflectance sidebands; it is this reflectance null that provides the transmission peak applied here [16].

Comparatively, as noted above, a classical multilayer architecture with nearly identical performance requires 15 layers of Si and SiO_2. It consists of a 14-layer Bragg stack and one embedded half-wave defect layer as illustrated in Figure 4–1(b); see the figure caption for the parameters of this multilayer device. Importantly, the single-layer grating architecture is advantageous over the classical multilayer structure in many practical aspects. For example, an array of bandpass filters with different central wavelengths can easily be integrated on a single substrate by simply changing the period. Such a filter array has potential applications in wavelength division multiplexing systems and compact spectrum analyzers without a wavelength-dispersive element. We also note that a variety

$\Lambda = 856$ nm $\ f\Lambda = 196$ nm

(a)

(b)

(c)

c-Si
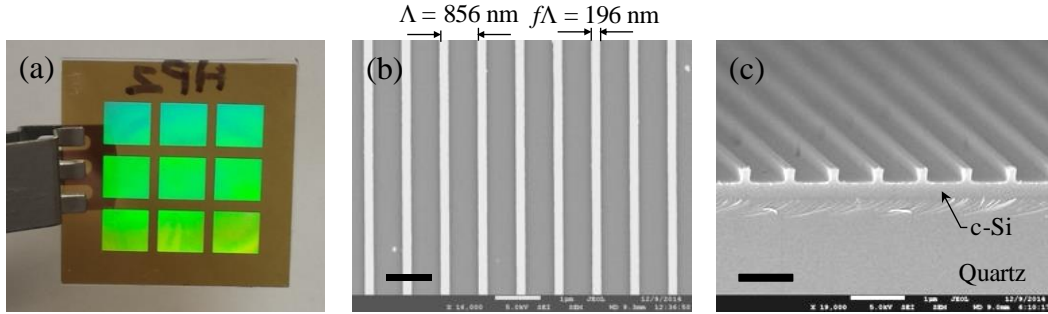
Quartz

Figure 4-2 Fabricated bandpass filter. (a) Photograph of nine fabricated devices on a 1×1 inch² silicon-on-quartz wafer. Each filter measures 5×5 mm². (b) Top-view and (c) cross-sectional scanning-electron micrographs of a device. Bar scales are 1 μm in (b) and (c).

of dielectric materials and structures is available for the proposed architecture in the visible, near-infrared, and longer wavelengths where the deposition of quarter- or half-wave multilayers is particularly tedious or impractical [14,57]. On the other hand, the polarization dependence of the resonant filters will be a drawback in some applications.

Experimental methods and results

Device fabrication

We experimentally demonstrate the proposed bandpass filter and its performance. In the fabrication, we use an SOQ wafer with 520-nm-thick c-Si on a quartz substrate. The fabrication processes include ultraviolet holographic lithography [6] to create a periodic photoresist mask, reactive-ion etching through the c-Si layer with a CHF_3+SF_6 gas mixture, and O_2 ashing for residual photoresist mask removal. Figure 4–2(a) shows nine fabricated devices on a 1×1 inch² SOQ wafer. Using scanning electron microscopy (SEM), we characterize the geometrical parameters of the fabricated device. Top-view and cross-sectional SEM images of a device are shown in Figures 4–2(b) and 4–2(c). The estimated parameters for the device with the best performance are period $\Lambda = 856$ nm, grating-ridge width $f\Lambda = 196$ nm, and grating depth $d_G = 272$ nm.
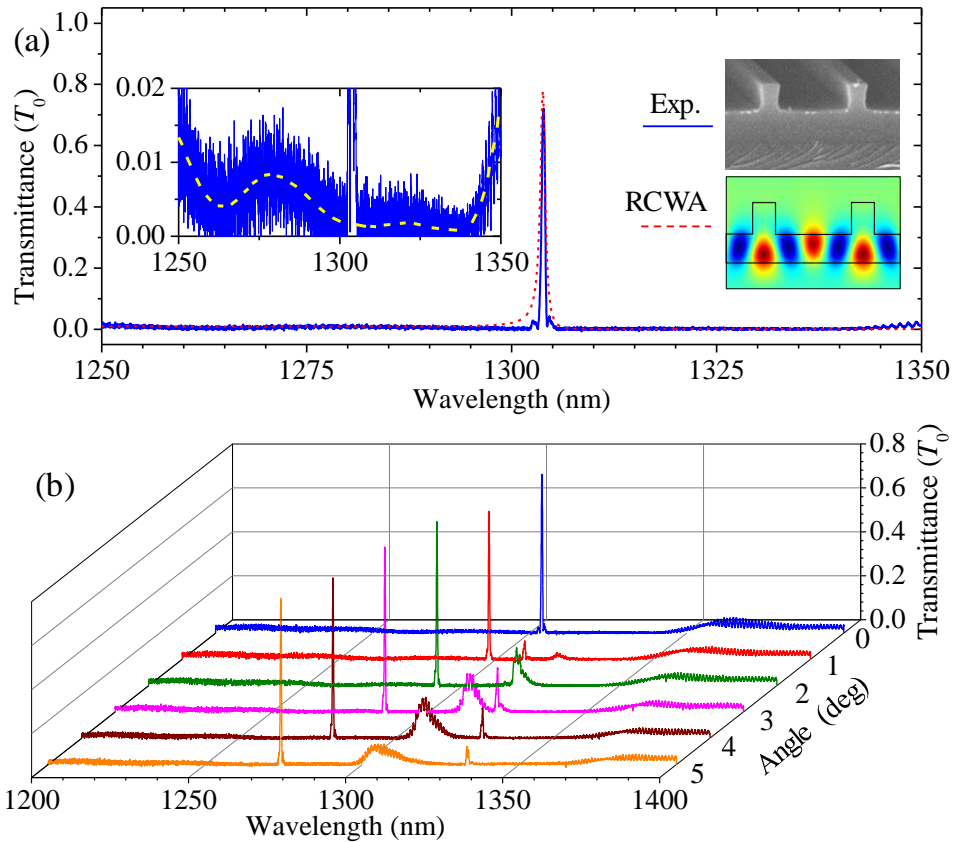
Figure 4-3 Experimental performance of a fabricated device. (a) Measured transmittance (T_0) spectrum in comparison with the RCWA simulation is shown. In the simulations, we use the fabricated device parameters obtained from AFM and SEM measurements. The inset graph shows a magnified view of the measured sideband spectrum before (blue solid) and after (yellow dashed) numerical noise rejection. Note that the source noise level is ~1% in transmittance. Additional insets show a close-up of the fabricated device and the computed internal electric-field distribution at resonance. (b) Angle-dependent T_0 spectrum for small angles of incidence.

Spectral measurements

For spectral measurements, we use a Koheras SuperK Compact super-continuum light source and a Yokogawa AQ6375 near-infrared optical spectrum analyzer (OSA). The input beam is highly collimated and TE-polarized with ~1 mm spot size. A single-mode optical fiber is used to transport the transmitted signal. T_0 is calculated as measured transmitted signal normalized by the measured transmitted signal without the device in

the beam path. An adequate sampling resolution of 0.02 nm is maintained in the OSA. The measured T_0 spectrum at normal incidence is shown in Figure 4–3(a). The narrow passband peak at λ = 1304 nm has an efficiency of 72.1% and a FWHM linewidth of Δλ = 0.48 nm. The resonance quality factor (Q-factor) is $\lambda/\Delta\lambda \approx 2.7\times10^3$. We note that higher Q-factors are theoretically attainable with this bandpass filtering principle [57]. The wide stopbands constituting the filter sidebands covering a 100-nm-wide wavelength region from 1250 nm to 1350 nm have T_0 < 1% as shown in the inset of Figure 4–3(a); furthermore, these bands remain reasonably low across a span exceeding 200 nm.

Angle-dependent T_0 spectrum is shown in Figure 4–3(b). Here, for every 1° increment in θ, the location of the transmission peak shifts by ~6 nm to a shorter wavelength while maintaining the high peak efficiency, narrow linewidth, and low stopbands. Therefore, this device permits continuous spectral tuning of the passband under angular adjustment. Angular-dependence of resonant bandpass filters is studied in detail in Chapter 7.

Parametric study

The theoretical spectrum in Figure 4–3(a) is calculated using the RCWA and quantitatively agrees with the experimental spectrum. The calculated T_0-peak efficiency in
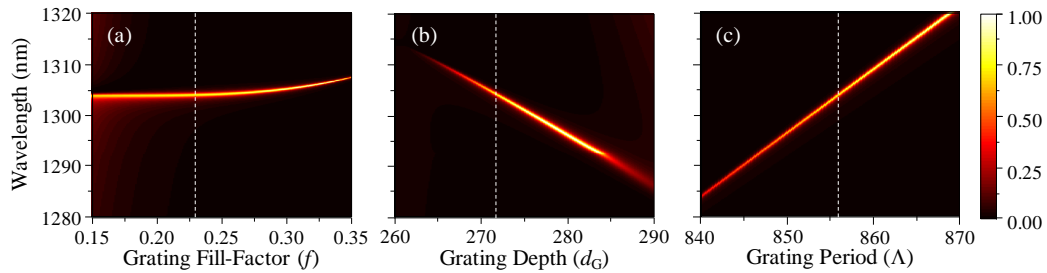
Figure 4-4 Parametric dependence of the bandpass filter. RCWA simulated T_0 spectra of the filter in relation to variations in (a) grating fill factor, (b) grating depth, and (c) grating period. Dashed white lines in (a), (b), and (c) represent fabricated device parameters.

Figure [4–3(a)](#) is ~77% for our experimental parameters. Had we successfully experimentally realized the PSO-optimized parameters of d_G = 277 nm, Λ = 860 nm and f = 0.24, a peak efficiency near 100% would be expected. We note that the final interface of the quartz substrate accounts for a ~4% drop in the observed peak efficiency; this is not compensated for in Figure [4–3](#).

The bandpass filter performance is fairly robust against minor parametric variations in the grating shape. This is because the high-intensity electric fields corresponding to a TE_0 mode are predominantly guided in the homogeneous c-Si layer as shown in the inset in Figure [4–3(a)](#). An RCWA-computed T_0 map in Figure [4–4(a)](#) shows spectral variation for changes in the grating fill factor (f). The experimental parameters are used in the calculation. Likewise, variation in the grating depth (d_G), for a constant film thickness (t = 520 nm), causes a shift in passband location and efficiency as shown in Figure [4–4(b)](#). This shift is attributed mainly to the attendant change in the thickness of the homogeneous c-Si layer where the TE_0 mode primarily resides. Finally, the transmittance map corresponding to variations in the grating period (Λ) is shown in Figure [4–4(c)](#). Here, the T_0-peak location is a near-linear function of Λ. As seen in Figures [4–4(a)-(c)](#), the stopbands are not significantly affected by variations in f, d_G, and Λ. This is because the transmission stopbands are formed by a low-Q resonance that is generally robust against minor parametric variations.

Conclusions

In conclusion, we provide the first experimental demonstration of an ultra-narrow bandpass filter in the near-infrared spectral domain using all-dielectric resonant gratings. We design, fabricate, and test nanostructured single-layer bandpass filters performing

with high efficiency, sub-nanometer-wide passbands and wide stopbands. The proposed device class is compatible with standard nanolithography processes and applicable to the visible/infrared/THz and longer wavelength domains. Recalling extraordinary optical transmission (EOT) through plasmonic nanoaperture arrays, nanostructured metallic bandpass filters have been fabricated [59]. However, the unavoidable inherent loss of metals results in low passband efficiencies and broad linewidths of EOT filters [59–61]. Therefore, further developing the device class proposed here is important for a host of applications. For example, this technology can be basis for wavelength-division demultiplexers, compact arrayed high-resolution spectrometers, hyper-spectral imaging, and Raman-scattering-based molecular-composition analyzers.

In future work, the results presented here can be improved by implementing single-layer crossed-grating designs for unpolarized light filtering. Recently, Shokooh-Saremi *et al*. proposed polarization-independent two-dimensional (2D) grating broadband mirrors designed using the PSO algorithm [19]. Hence, PSO is an effective tool for designing polarization-independent bandpass filters. An important near-term pursuit is to experimentally verify high-quality unpolarized bandpass filters of this kind.

Chapter 5
Concurrent spatial and spectral filters

Subwavelength periodic structures enable versatile applications including label-free optical biosensors [62], high-performance optical filters [12,14,43,53,63], broadband reflectors [33,45,52], beam-transforming meta-surfaces [55], absorbers [24,64], and high-Q optical resonators [65,66]. In the subwavelength regime with only zero-order external propagating waves, coupling of an input excitation wave with a resonant leaky mode can be modeled as a generic two-port resonance system. In lossless systems, the attendant resonant reflectance is unity regardless of the details of the particular coupling configuration [48]. Therefore, the resonance spectra in reflection and transmission form angular continua on characteristic dispersion bands in the angle-wavelength space [8,33]. In contrast, in this chapter, we show that non-subwavelength nanogratings with multiple propagative diffraction channels enable an angularly discrete resonance response. Previously it was shown that high first-order diffraction efficiency can be achieved with non-subwavelength resonant gratings. In particular, Parriaux and co-workers reported near-total first-order reflection from mirror-based waveguide-grating structures [67,68]. There are no prior reports on discrete angular resonance states as provided in this Chapter.

Proposed device

Our device concept is illustrated in Figure 5–1(a). The reflection is confined to a narrow, collimated spectral channel even under wideband diverging or converging incident light. Obtaining efficient zero-order reflection in the non-subwavelength regime involves simultaneous suppression of all other propagating orders. We accomplish this by
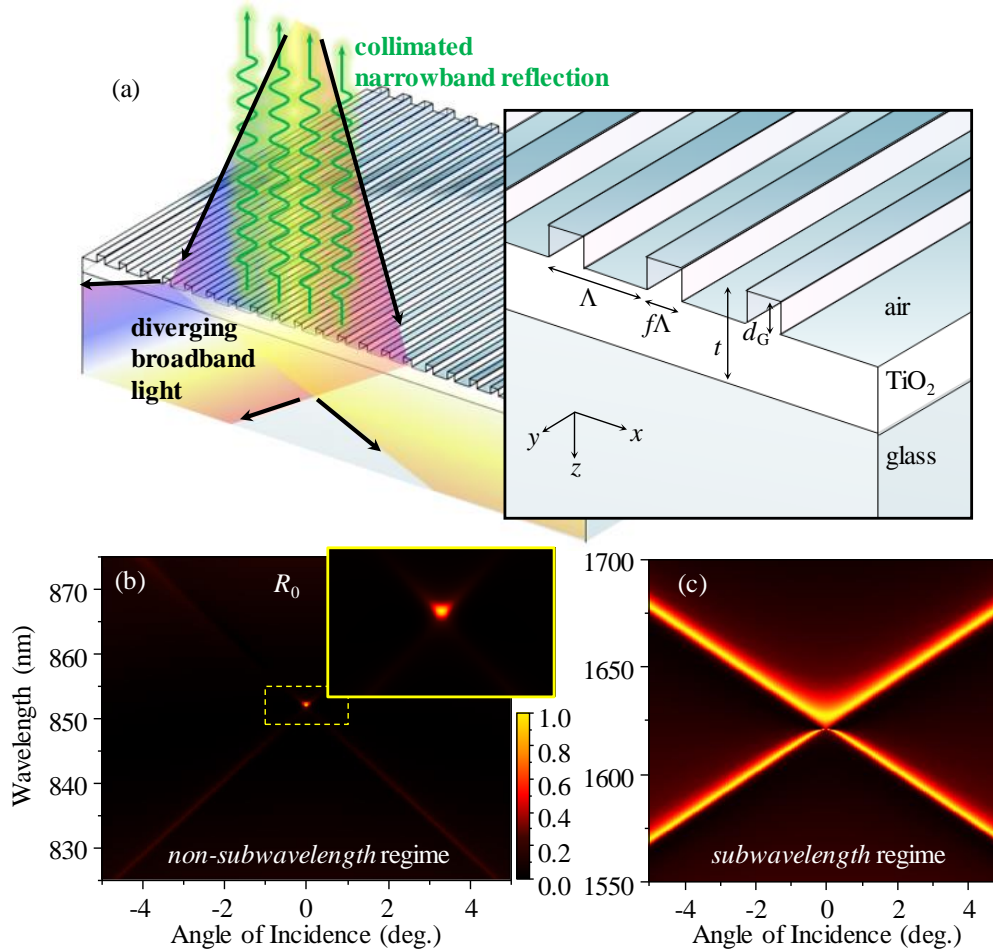
Figure 5-1 Theoretical reflectance showing spatial/spectral delta function characteristics. (a) Device schematic. The geometry is defined by the grating period Λ; fill factor F; total film thickness t and grating depth d. Refractive indices are $n_F = 2.52$ for the TiO$_2$ film, $n_S = 1.54$ for the glass substrate, and $n_C = 1.0$ for air. (b) Computed angle-dependent zero-order reflectance (R_0) spectrum of an optimized device under TE-polarized light incidence (electric field vector along y). The optimized parameters are $\Lambda = 696$ nm, $F = 0.33$, $t = 788$ nm, and $d = 210$ nm. (c) Angle-dependent R_0 spectrum of the same device in the subwavelength regime in the 1550~1700 nm wavelength region.

parametric optimization grounded in particle-swarm optimization (PSO) method [31]. In PSO, we use rigorous coupled-wave analysis (RCWA) [29] algorithm as forward computational kernel. We model a partially etched TiO$_2$ waveguide grating on a glass substrate as shown in Figure 5–1(a). The angle-dependent zero-order reflectance (R_0)
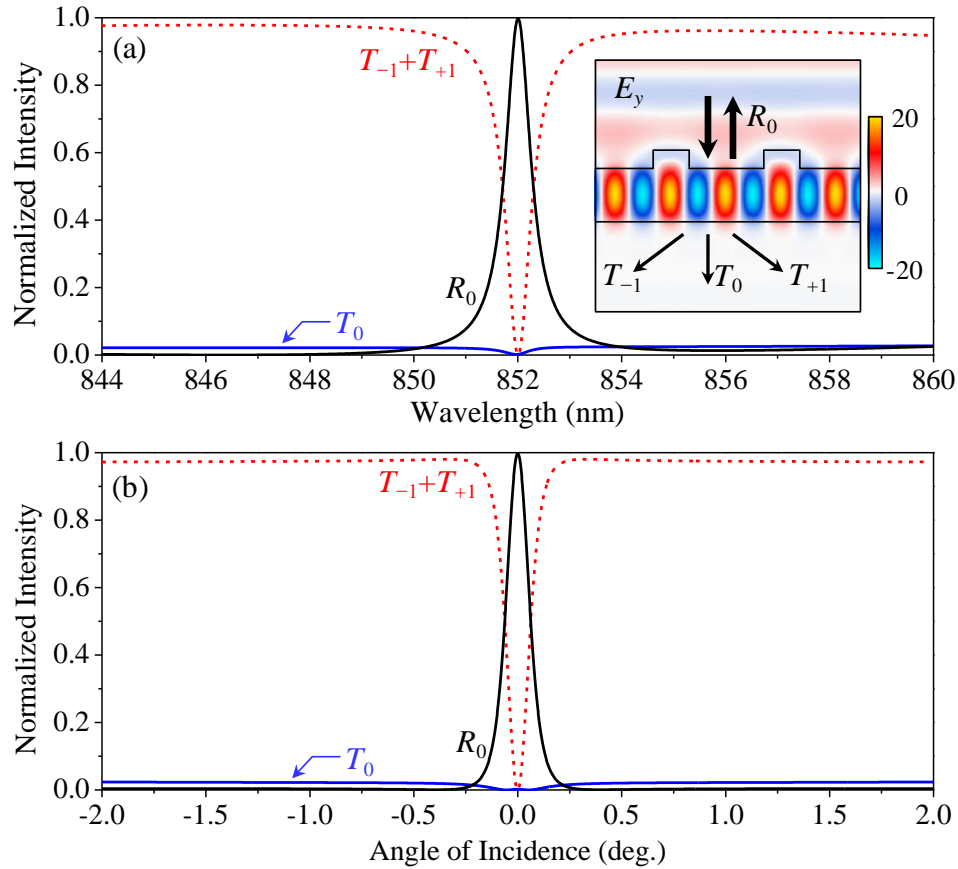
Figure 5-2 Diffraction efficiency pertinent to the device in Figure 5-1. (a) Spectra of all propagating orders under normal incidence. (b) Angular spectra of all propagating orders at wavelength λ = 852 nm. Inset in (a) shows the localized electric field amplitude distribution at the reflection-peak wavelength. The field amplitude is normalized by the incident field amplitude. The *y*-axis in (a) and (b) are identical.

spectrum under transverse-electric (TE) polarized light incidence in Figure 5–1(b) shows

the unique discrete angular/spectral reflection state at λ = 852 nm under normal incidence

(θ = 0). The reflection peak has 99.8% efficiency and full-width-at-half-maximum (FWHM)

bandwidths of $\Delta\lambda$ = 0.6 nm in wavelength and $\Delta\theta$ = 0.12° in angle. In the 1550~1700 nm

spectral band, this device transits to the subwavelength regime where different

functionality prevails. Figure 5–1(c) shows the corresponding spectrum; it is clearly

completely different than the spectrum in Figure 5–1(b). The chief objective of this Letter

is to explain this dramatic difference and provide experimental verification of the predicted discrete spectra.

The inset in Figure 5–2(a) shows the electric field distribution at the reflection peak center and the propagating waves associated with the device. The resonance is induced by a standing TE_0 guided mode coupling to four external waves R_0, T_0, and $T_{\pm 1}$. The spectra in Figures 5–2(a) and 5–2(b) show high-efficiency reflectance R_0 even with multiple simultaneous propagating waves that generally reduce the power available to it. The non-resonant background shows weak zero-order intensities R_0 and T_0 with most of the incident energy coupling to the two transmitted first-order substrate waves $T_{\pm 1}$. We remark that this effect is not associated with any Rayleigh-type power exchange [69]. The resonant excitation of the standing TE_0 guided mode at $\lambda = 852$ nm and $\theta = 0$ exchanges the dominant diffraction channel from $T_{\pm 1}$ to R_0 while T_0 remains persistently low. This new, intriguing power transfer mechanism requires detailed analysis.

Pathway and intermodal effects analysis

The discrete angular/spectral reflection state observed in Figure 5–2 can be explained by invoking two distinct interference mechanisms. First, interference between resonant and non-resonant diffraction pathways plays an important role. Figure 5–3(a) illustrates the two different diffraction pathways. The incident wave couples to four propagating diffraction orders. These are the zero-order reflected wave, zero-order transmitted wave, and two first-order transmitted waves. The second-order diffracted wave in the TiO_2 layer is totally reflected at the bottom TiO_2-glass interface and drives a TE_0-type mode yielding a guided-mode resonance mechanism [12]. Therefore, re-radiation of the mode to each outgoing diffraction order constitutes the resonant pathway. As
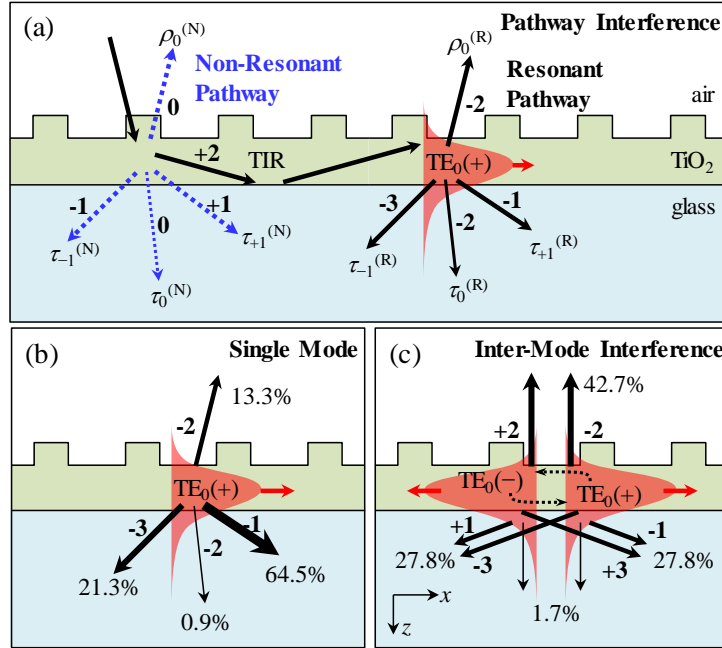
Figure 5-3 Interference effects associated with the discrete angular/spectral reflection. (a) Radiation pathways hypothesized to explain the observed spectra. The non-resonant pathway is formed by direct diffraction of the incident light. The resonant pathway is defined by leakage radiation stimulated by a TE_0 mode coupling through second-order diffraction. Integer numbers label dominant coupling diffraction orders for waves indicated by the arrows. (b) Leakage radiation probabilities pertaining to a traveling TE_0 mode at $\lambda = 848$ nm and $\theta = 0.565°$. (c) Leakage radiation probabilities associated with counter-propagating leaky modes at $\lambda = 852$ nm and $\theta = 0$.

indicated in Figure 5–3(a), $\rho_0^{(R)}$, $\tau_0^{(R)}$, and $\tau_{\pm1}^{(R)}$ refer to the *resonant* zero-order reflection, zero-order transmission, and first-order transmission amplitudes, respectively. Consequently, the non-resonant pathway corresponds to all other diffraction pathways which do not involve the second-order diffraction in the TiO_2 layer. The *non-resonant* diffraction amplitudes are thus denoted by $\rho_0^{(N)}$, $\tau_0^{(N)}$, and $\tau_{\pm1}^{(N)}$. Analogous interference picture applies to reflection resonances in the zero-order regime [70]. The intensity of the outgoing diffraction orders is expressed by a superposition such that $R_0 = |\rho_0^{(N)}+\rho_0^{(R)}|^2$, $T_0 = |\tau_0^{(N)}+\tau_0^{(R)}|^2$, and $T_{\pm1} = |\tau_{\pm1}^{(N)}+\tau_{\pm1}^{(R)}|^2$. The non-resonant amplitudes contribute the sideband intensity in the spectra. In the spectra in Figures 5–2(a) and 5–2(b), we see that

$\rho_0^{(N)} \approx 0$, $\tau_0^{(N)} \approx 0$, and $\tau_0^{(R)} \approx 0$ such that $R_0 \approx |\rho_0^{(R)}|^2$ and $T_0 \approx 0$. At the reflection peak center at $\lambda = 852$ nm and $\theta = 0$ in Figures 5–2(a) and 5–2(b) we see that $T_{\pm 1} \approx 0$ implying a nearly complete destructive interference between $\tau_{\pm 1}^{(N)}$ and $\tau_{\pm 1}^{(R)}$, meaning that there is a π phase difference between the two pathways with equal amplitudes, i.e., $\tau_{\pm 1}^{(N)} \approx -\tau_{\pm 1}^{(R)}$. By energy conservation this implies $R_0 \approx |\rho_0^{(R)}|^2 \approx 1$. The optimized structure is designed so that complete destructive pathway interference occurs in the first-order transmission channels at $\theta = 0$.

Under off-normal incidence, the destructive pathway interference in the first-order transmission becomes incomplete due to asymmetry in $\tau_{+1}^{(R)}$ and $\tau_{-1}^{(R)}$. In Figure 5–3(b), we indicate the leakage radiation probabilities associated with a TE$_0$ guided mode resonating at $\lambda = 848$ nm at a small off-normal angle ($\theta = 0.565°$). The leakage radiation probabilities are calculated by the absorbance analysis method proposed in [71] with following equation for peak absorbance

$$A_n = 4\eta_{abs}\eta_n, \tag{5.1}$$

where A_n is peak absorbance under wave incidence at radiation channel n, η_{abs} is absorption probability, and η_n is radiation probability of the resonant mode to radiation channel n. Eq. 5.1 can be used for inferring radiation probabilities even in lossless cases with $A_n = 0$ by taking the asymptotic limit

$$\eta_n = \lim_{k \to 0} \frac{A_n}{\sum_m A_m}, \tag{5.2}$$

where the index m in the summation runs over all the available radiation channels and k is the extinction coefficient of the material forming the resonator under consideration. For the single TE$_0$ mode in Figure 5–3(b), the radiation probabilities into $\tau_{+1}^{(R)}$ and $\tau_{-1}^{(R)}$ are

64.5% and 21.3%, respectively, denoting substantial asymmetry. This is a natural consequence of the difference in the coupling orders as $\tau_{+1}^{(R)}$ is emitted as first-order diffraction of the driving mode whereas $\tau_{-1}^{(R)}$ is generated by a third-order diffraction process. In contrast, the non-resonant amplitudes are approximately symmetric, i.e., $\tau_{+1}^{(N)} \approx \tau_{-1}^{(N)}$, because they both couple through a first-order process at small angle of incidence. Therefore, for $\theta \neq 0$, pathway interference in T_{+1} and T_{-1} cannot be identically destructive, resulting in sizable intensity in the first-order transmission channels and a weaker R_0 at resonance.

The enhancement of R_0 on resonance at $\theta = 0$ involves interference between secondary waves radiated by counter-propagating leaky modes. In Figure 5–3(c), we show the radiation probabilities and coupling orders for the standing TE_0 mode at $\lambda = 852$ nm and $\theta = 0$ corresponding to the resonance center of the discrete angular/spectral reflection state. We confirm that the radiation probability towards zero-order reflection is remarkably enhanced to 42.7% for the standing-mode case relative to 13.3% for the traveling-mode case in Figure 5–3(b). In contrast, as noted in Figure 5–3(c), the net radiation probability to the first-order transmission channels is substantially reduced. In Figure 5–3(c), the $TE_0(+)$ mode traveling in the $+x$ direction couples to the T_{+1} channel through first-order diffraction while the $TE_0(-)$ mode traveling along $-x$ contributes to this channel by third-order diffraction. We calculate the phase difference between these two contributions finding $\sim 1.09\pi$. The close-to-π phase difference provides destructive interference between the two constitutive components generated by the modes running along $\pm x$. This reduces the amplitude of $\tau_{\pm 1}^{(R)}$ sufficiently to enable their final extinction by interference with $\tau_{\pm 1}^{(N)}$.

Experimental results

Proof-of-concept experiments verify the proposed concept. We fabricate devices using sputtered TiO_2 films on microscope slides applying UV-laser interference lithography and reactive-ion etching. Shown in Figures 5–4(a) and 5–4(b) are scanning electron micrographs of the fabricated device. From these micrographs, the measured device parameters are period Λ = 753 nm, fill factor F = 0.25, TiO_2-film thickness t = 602 nm and grating depth d = 210 nm. The measured R_0 spectrum is shown in Figure 5–4(c). We clearly observe a discrete reflection peak at λ = 812 nm and θ = 0. The RCWA calculation assuming the device structure indicated by the red-dashed lines in Figure 5–4(b) shows excellent *quantitative* agreement with the experimental results as indicated in Figures 5–4(d) and 5–4(e). In the experiment, the resonance peak attains 80.1% efficiency and FWHM bandwidth of 1.42 nm in wavelength and 0.24° in angle.
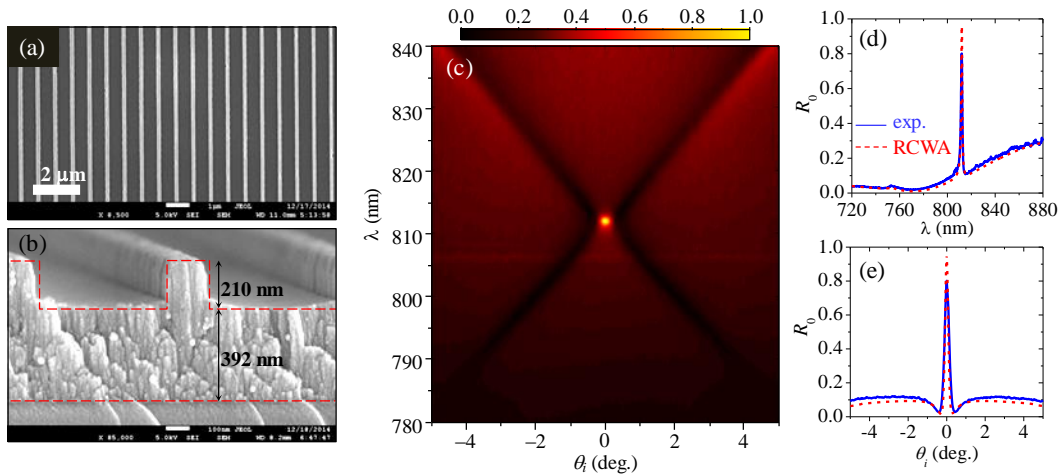
Figure 5-4 Experimental demonstration of a discrete angular and spectral reflector. (a) Top-view and (b) cross-sectional scanning electron micrographs of the fabricated device. Red-dashed lines in (b) indicate the structure used in the numerical calculation (RCWA) for comparison. (c) Measured angle-dependent R_0 spectrum. (d) Measured spectra and comparison with numerical calculation under normal incidence. (e) Angular spectrum at wavelength λ = 812 nm.

Spatial filtering application

An interesting potential use of the narrow angular selectivity is focus-free spatial filtering. In many applications, spatial filters are necessary to eliminate spatial noise associated with random laser fluctuation and scattering. Figure 5–5(a) shows conventional spatial filtering applying a pair of lenses and a pinhole. In this arrangement, high-accuracy optical alignment is required. Moreover, high-power applications are limited by potential pinhole thermal failure. Our device avoids these limitations owing to its focus-free spatial filtering property as illustrated in Figure 5–5(b). In this example, the spatial filter rejects high-frequency noise components without a focusing lens and pinhole.
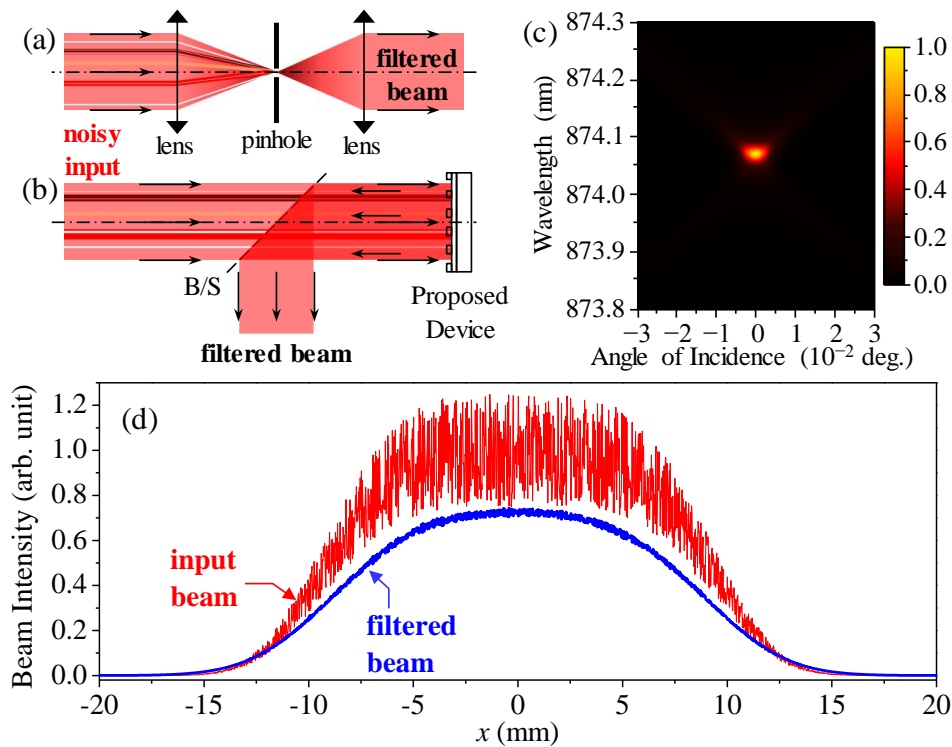
Figure 5-5 Spatial filtering with a discrete angular reflector element. (a) Conventional spatial filter using a pinhole/lens pair. (b) Proposed spatial/spectral filter fashioned with a resonant nanograting. (c) Reflectance spectrum of the spatial/spectral filter. The device parameters are Λ = 696 nm, F = 0.33, t = 2210 nm, and d = 210 nm. (d) Theoretical performance of the spatial filter with an input super-Gaussian laser beam with FWHM width of 16 mm carrying computer-generated pseudo-random noise.

We numerically demonstrate example performance of a focus-free spatial filter in this class. We design an ultra-sharp angular reflector with peak reflectance ~99.9% at wavelength λ = 874.069 nm and bandwidths of $\Delta\theta$ = 0.005° and $\Delta\lambda$ = 23 pm as shown in Figure 5–5(c). This angular bandwidth corresponds to a conventional spatial filter using a pinhole with a 1.7-μm diameter and an objective lens with focal length of 10 mm. The top TiO$_2$ grating of this design is identical to the design in Figure 5-1 but the new design has a thicker TiO$_2$ sublayer. The filtering performance of this element is presented in Figure 5–5(d). We assume a 16-mm-wide TE-polarized super-Gaussian beam carrying computer-generated pseudo-random noise as input light. The electric field of the beam is given by

$$E_{\text{in}}(x) = E_0 \left[1 + af(x)\right]^{1/2} \exp\left[-\frac{1}{2}\left(\frac{x}{w}\right)^4\right], \tag{5.3}$$

where a is a normalized amplitude of the computer-generated pseudo-random function $f(x)$ with [–1/2, 1/2] range and w is the beam width. The filtered output beam intensity is calculated by using the Fourier-decomposition method with the equations

$$\varepsilon_{\text{in}}(\theta) = \int\limits_{-\infty}^{+\infty} E_{\text{in}}(x)e^{-i2\pi x \cos\theta/\lambda} dx, \tag{5.4}$$

$$E_{\text{out}}(x) = \frac{1}{\lambda} \int\limits_{-\pi/2}^{+\pi/2} \rho_0(\theta)\varepsilon_{\text{in}}(\theta)e^{i2\pi x \cos\theta/\lambda} \cos\theta d\theta, \tag{5.5}$$

where λ is wavelength and $\rho_0(\theta)$ is the complex reflection coefficient of the discrete angular reflector. This formalism is valid for the far-field filtering property where evanescent components in the incident beam transfer no signal to the output beam. The intensity profiles in Figure 5–5(d) are calculated by taking the absolute square of the electric field

amplitudes, i.e., $|E_{in}|^2$ and $|E_{out}|^2$. The input beam parameters used in Figure are $a = 0.5$ and $w = 10$ mm. We find that the noise in the filtered output beam is reduced by a factor of ~17. The filtered output profile maintains the flat-top property of the input super-Gaussian beam in contrast to the sharp-top Airy disk profile characteristics of conventional spatial filters.

Conclusions

To conclude, we provide a new spatial/spectral filter concept based on guided-mode resonance effects in the non-subwavelength regime. We show that complex inter-modal and pathway interference processes enable these unique angular and spectral properties that are not feasible in the subwavelength regime. The experimental results show excellent quantitative agreement with theoretical predictions. We numerically demonstrate focus-free spatial filtering with the proposed device concept. We remark that the pathway and inter-modal interference effects invoked in the physical explanation of the device operation represent general aspects of guided-mode resonance phenomena in the non-subwavelength regime. Therefore, we expect high-efficiency spatial/spectral selectivity to be feasible in other diffraction channels including in zero-order transmission T_0. Developing such elements in connection with appropriate tuning methods may enable innovative solutions for directional and spectral beam management in solid-state light emitters without bulky external components.

Chapter 6

Wideband unpolarized resonant reflectors

Resonant broadband reflection implemented with dielectric subwavelength gratings is a functional basis for a host of applications, including low-loss mirrors [17,18], narrow-linewidth bandpass filters [72], beam-transforming surfaces [55], and polarizers [21,22]. Devices in this class are often designed with a single dielectric thin-film layer and may incorporate carefully-crafted grating architectures to meet specifications for a particular application. Comparatively, obtaining a similar performance using traditional distributed Bragg stacks requires perhaps ~10-100 quarter- and/or half-wave layers [49]. Multilayer thin-film-based broadband dielectric mirrors represent an established technology. Their commercial manufacturers deposit multilayer films with high precision in layer thickness and index of refraction. The reflectivity and bandwidth of a traditional Bragg stack depends on the number of quarter-wave layer pairs and their refractive-index contrast [49]. At longer wavelengths of light, in the mid-infrared and THz domains for instance, multiple thin-film deposition is often impractical on account of typically-slow deposition techniques and issues in maintaining consistent deposition conditions across long time spans. Resonant grating reflectors achieve superior performance by way of parametric optimization [18,73]. Indeed, single-layer subwavelength grating mirrors can easily be scaled to be operative in any wavelength regime assuming availability of suitable materials. Practical challenges in fabrication include the need for periodic patterning, control of etch or imprint processes to maintain grating features, and management of process-induced scattering centers.

Broadband light reflection from a single-layer subwavelength grating is an interesting, perhaps counterintuitive, phenomenon as the constituent materials are optically transparent in nature. This phenomenon is understood as a low-Q broadband resonance effect driven by laterally-guided Bloch modes [18,70,73]. Each mode represents a reflection peak (transmission dip) in the spectrum. In high-index grating architectures, wideband reflection can occur when reflection peaks corresponding to multiple guided-modes share a common, high-reflection band over a wide wavelength range. In a recent theoretical study, Magnusson showed that broadband mirrors based on subwavelength gratings can support wide reflection bands with efficiencies exceeding 99.99% [18]. Experimental demonstration of high-efficiency broadband mirrors based on this device class has been largely limited to input-polarization-dependent reflection [17,74]. There has been no prior experimental demonstration of wideband, high-efficiency, polarization-independent mirrors, which are critical in many practical applications.

In this chapter, we report comprehensive design, fabrication, and spectral characterization of broadband mirrors based on subwavelength silicon gratings. As the constituent individual 1D-grating reflectors are polarization dependent, we arrange two gratings in series with orthogonal periodicity to achieve broadband reflection for unpolarized light incidence. The individual grating reflectors are separated by a gap to avoid evanescent field coupling between them. Excellent theoretical and experimental results are obtained, verifying the feasibility of the fundamental idea.

Elemental Reflector Concept

The canonical device structure applied here consists of a thin layer of partially etched crystalline silicon (c-Si) on a quartz substrate as shown in Figure 6–1(a). The c-Si
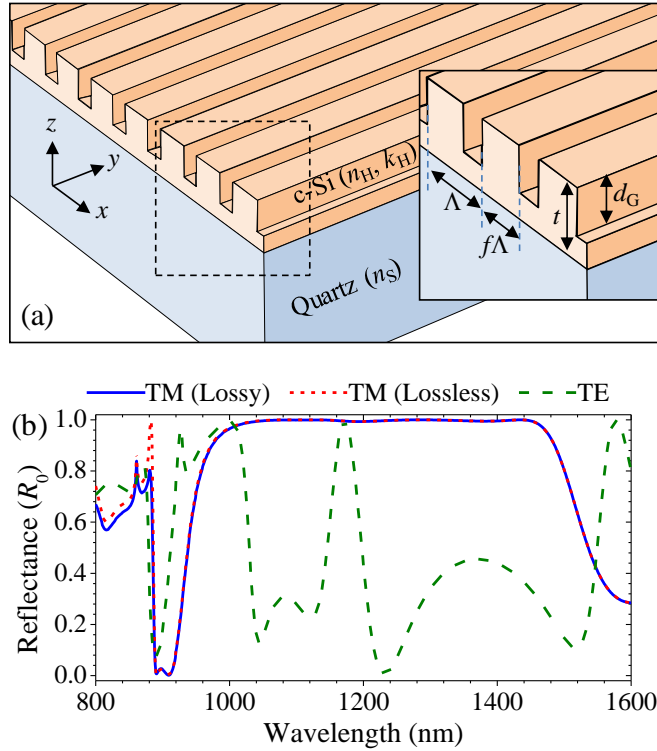
Figure 6-1 Structure and performance of a subwavelength broadband mirror. (a) The device structure of a thin-layer of partially etched c-Si on a quartz substrate. PSO optimized geometrical parameters are: period Λ = 560 nm, fill factor f = 0.66, c-Si layer thickness t = 520 nm, and grating depth d_G = 332 nm. Refractive indices are n_H and n_S for c-Si and quartz, respectively. c-Si is modeled with extinction coefficient k_H. (b) Computed zero-order reflectance (R_0) of the device for light incidence at normal angle. Spectral response for TM polarization is presented for both lossy (solid blue) and lossless (dashed red) cases. The TE spectrum (dashed green) does not exhibit wideband reflection.

layer, of total thickness t, is partially etched to create a 1D grating. The c-Si film lies on the x-y plane with the grating grooves parallel to the y-axis. The grating is periodic along the x-axis with a constant period of Λ. Each grating ridge has a height of d_G and a width of $f\Lambda$, where f is the grating fill factor. We call this variety a "zero-contrast grating" (ZCG) as the grating ridges are matched to a sublayer made out of the same material; hence, no phase changes occur for a ridge mode transiting across the ridge/sublayer interface [18]. Using the particle-swarm optimization (PSO) method [15,70], we optimize the geometrical

64

parameters of the grating structure to support high-efficiency broadband reflection for transverse-magnetic (TM) polarized light at normal incidence. Input light is in the TM (as opposed to transverse-electric, TE) polarization state if the magnetic (electric for TE) field vector is oriented along the grating grooves (y-axis). In the PSO calculations, we use an algorithm grounded in rigorous coupled-wave analysis (RCWA) [29] as the forward kernel to compute the spectral response. In our simulations, we account for the material dispersion in c-Si (refractive index = n_H, extinction coefficient = k_H) and quartz (refractive index = n_S). The optical constants for c-Si are obtained from [75].

The PSO-optimized geometrical parameters are period Λ = 560 nm, fill factor f = 0.66, grating depth (d_G) = 332 nm, and film thickness t = 520 nm. Simulated zero-order reflectance (R_0) spectra for an elemental reflector with these geometrical parameters are shown in Figure 6–1(b). The TM spectral response encompasses a 430-nm-wide spectral band extending from 1030 nm to 1460 nm with R_0 exceeding 99%. As the broadband reflection stems from resonances with low Q factors, we do not expect a significant drop in reflection efficiency due to extinction loss in the c-Si grating. Indeed, this is true as shown by the comparison between spectral responses for lossy and lossless cases in Figure 6–1(b). A small degradation in reflection efficiency due to absorption loss is observed at wavelengths $\lambda \leq 1100$ nm. At $\lambda > 1100$ nm, the effect is negligible as c-Si becomes virtually lossless at that point.

Serial Configuration for Unpolarized Reflection

It is well known that the 1D nature of these gratings results in a different spectral response for input TE and TM polarizations. This is clearly seen in Figure 6–1(b). Taking advantage of this difference, broadband polarizers where one polarization is nearly
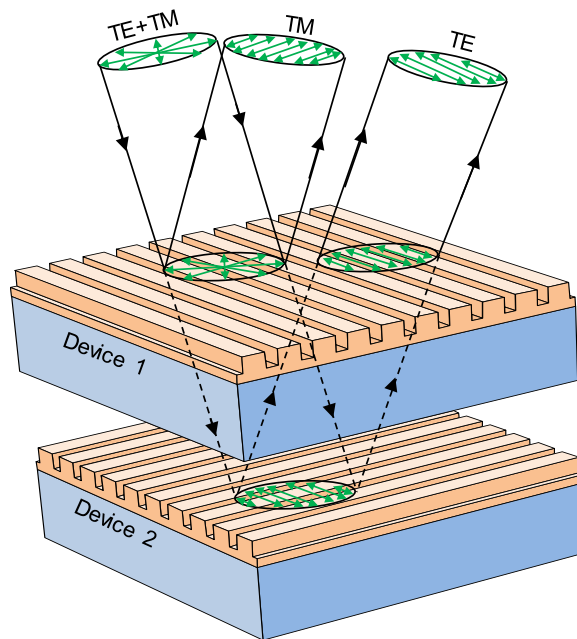
Figure 6-2 Serial arrangement of elemental ZCG reflectors. The grating vectors of the two identical subwavelength grating mirrors, labeled as Device 1 and Device 2, are orthogonal. For unpolarized light incidence, Device 1 reflects the TM polarization components and Device 2 reflects the TE polarization components relative to Device 1. Note that the transmitted TE-polarized light from Device 1 is in the TM polarization state relative to Device 2.

completely transmitted and the other is nearly fully reflected have been proposed [22]. However, in many applications for broadband mirrors, input-polarization-independent performance is required. Recently, resonant reflectors that are periodic in 2D were proposed to reflect both TE and TM polarizations of light [19,76,77]. In contrast, here we demonstrate a polarization-independent spectral response by arranging two polarization-dependent ZCG-type reflectors such as those presented in Figure 6–1 in series. This idea is illustrated in Figure 6–2. There, two mirrors, denoted Device 1 and Device 2, have their grating grooves orthogonal to one another. For unpolarized light incidence, Device 1 nearly completely reflects the TM component of the light and partially transmits the TE component to Device 2. This transmitted light is now TM polarized with respect to Device

2 and is therefore almost completely reflected, resulting in near-complete reflection of both TE and TM components of the incident light.

The device concept in Figure 6–2 relies on serial ZCG gratings that are spaced sufficiently far apart to avoid coupling between them via evanescent local fields. This concept differs from a theoretical proposal by Zhao *et al.* where cross-stacked gratings forming a two-layer woodpile photonic crystal are laid on a single substrate [78,79]. There, unpolarized light reflection across ~200 nm is a result spectral of overlap between reflective, but different, response for TE and TM polarized light input. Fabrication of woodpile photonic crystals is considerably more challenging than the simple single-layer devices provided currently.

Materials and Methods

Our elemental ZCGs in Figure 6–1(a) are fabricated using a commercially-available silicon-on-quartz (SOQ) wafer (Shin-Etsu Chemical Co). The SOQ wafer has a 520-nm-thick c-Si film on a quartz substrate. We use holographic lithography [6] to expose UVN-30, a negative photoresist (PR), creating a 1D mask. We reactive-ion etch (RIE) through the c-Si layer using SF_6 + CF_4 gas mixture. Residual PR after RIE is removed by ashing in an O_2 ambient. We characterize the fabricated devices using atomic force microscopy (AFM) and scanning electron microscopy (SEM) while optimizing the fabrication process to achieve the desired device geometry. Our ZCG reflectors for application in the serial configuration are fabricated using identical process conditions.

In the measurements, we use a super-continuum light source and a near-infrared optical spectrum analyzer. We measure the zero-order transmittance (T_0) of the elemental ZCG reflector as well as that of the sequential two reflectors. For an elemental ZCG

reflector, we measure T_0 as the transmitted signal normalized by the input signal for a particular polarization state. For the sequential arrangement, we use unpolarized light as input. In these experiments, the reference signal is the direct measured source spectrum with the sample removed and no other experimental components changed. Due to the subwavelength nature of the gratings, only zero-order propagating waves exist at wavelengths longer than the Rayleigh wavelength defined here in terms of the substrate index as $\lambda_R = \Lambda n_S$ (~850 nm). It follows that R_0 can be closely approximated as $1 - T_0$, especially at $\lambda > 1100$ nm where absorption loss due to the extinction loss in silicon is negligible.

To characterize high-efficiency mirrors and verify their actual performance, direct measurement of the reflectance, as opposed to approximating it as $1 - T_0$, is typically desired. However, establishing a reliable and well-defined reference signal is challenging especially in multicomponent experiments where motion of a component in the beam path may lead to beam misalignment and associated errors. In order to verify the data collected by the transmission approach, we perform reflection experiments comparing directly the reflectance of a sample and a metal mirror. Thus, to avoid misalignment, we deposit, through vacuum sputtering, a gold film on a non-device area of the SOQ wafer. The ~100-nm-thick gold film serves as a reference mirror, enabling the measurement of a reference signal without having to replace the sample thereby preserving alignment. We measure the reflection intensities of the gold coating and an elemental ZCG reflector for TM polarized light input. Gold coatings are highly-reflective above 900 nm in wavelength with reflectivity greater than 98% [80].
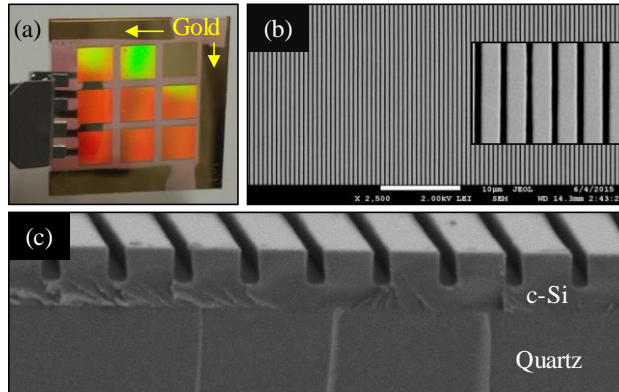
Figure 6-3 Fabricated broadband mirror. (a) Photograph of nine fabricated devices on a 1x1 inch² SOQ wafer. Each device is 5x5 mm². Approximately 100-nm-thick gold film is sputtered on the non-device edges of the SOQ wafer. Scanning-electron micrographs showing (b) top-view and (c) cross-sectional images of a representative device.

Results and Discussion

A photograph of an array of nine fabricated devices on a single SOQ wafer is shown in Figure 6–3(a). Here, we note that an array of broadband mirrors, each with different spectral characteristics and central wavelengths within the constraint of constant thickness, can easily be integrated on a single chip by varying the period and fill factor during holographic exposure; this is not generally feasible with multilayer Bragg stacks. Top-view SEM image of a representative device in Figure 6–3(b) shows highly uniform grating lines. A cross-sectional SEM is shown in Figure 6–3(c). Owing to its smoothness, we expect the scattering loss due to the grating fabrication process to be negligible. The pair of ZCG mirrors fabricated for sequential arrangement have similar geometrical parameters which are $f = 0.63$, $d_G = 330$ nm, $t = 520$ nm, and $\Lambda = 560$ nm.

Experimental T_0 and R_0 spectra of an elemental ZCG reflector for TM-polarized light incidence are shown in Figure 6–4(a). A normal angle of incidence is maintained. The measured reflectance spectrum features a 490-nm-wide spectral band stretching from ~960
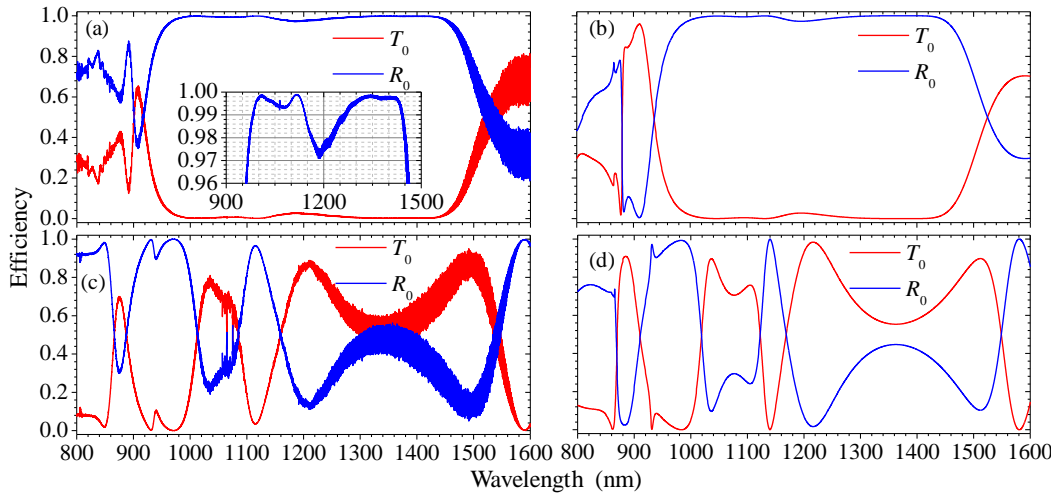
Figure 6-4 Input-polarization-dependent spectral response. (a) Experimental and (b) simulated T_0 and R_0 spectra for TM polarized light incidence. (c) Experimental and (d) simulated T_0 and R_0 spectra for TE-polarized light incidence. Device parameters are fill factor f = 0.63, grating depth d_G = 330 nm, c-Si film thickness t = 520 nm, and grating period Λ = 560 nm. The inset in (a) shows the wavelength band for R_0 > 96%. Spectral fluctuations in the measurements for λ > 1200 nm are due to Fabry-Perot resonance effects in the quartz substrate. We note that this fluctuation in (a) in the 1200-1450 nm band is weak due to low T_0 intensity in that band.

nm to ~1450 nm with R_0>0.97. The RCWA simulated TM spectrum in Figure 6–4(b) shows

an excellent *quantitative* agreement with the experimental spectrum in Figure 6–4(a). In the

simulations we use the geometrical device parameters obtained from AFM and SEM

measurements of the actual samples. In addition, Figures 6–4(c) and 6–4(d) show good

quantitative agreement between measured and simulated spectra for TE polarized light

incidence.

Outstanding experimental performance of an elemental ZCG reflector is limited

to TM polarization, as is evident by the experimental results in Figure 6–4. To demonstrate

unpolarized broadband reflection, we concatenate two ZCGs as in Figure 6–2 and proceed

to experimental characterization. Measurement results using unpolarized light at normal

incidence are shown in Figure 6–5. Here, the 520-nm-wide reflection band from ~915 nm
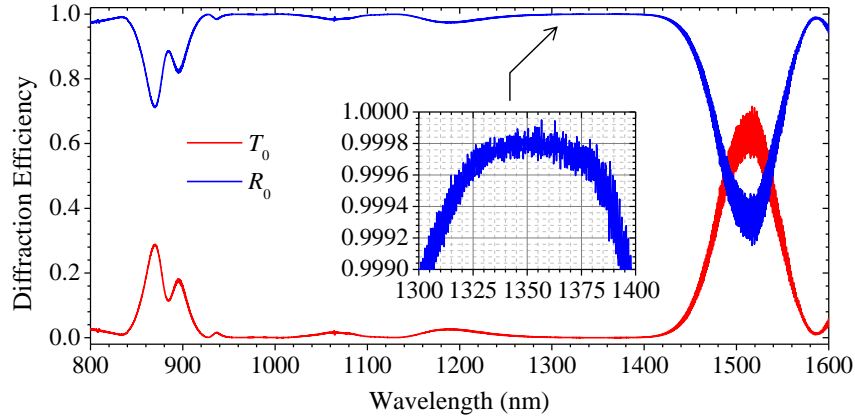
Figure 6-5 Polarization-independent spectral response. Measured T_0 and R_0 data using the experimental setup illustrated in Figure 6–2 for unpolarized light at normal incidence. R_0 is approximated as $1 - T_0$. The inset shows the wavelength band with $R_0 > 99.9\%$.

to ~1435 nm lies above 97% in reflectance. Moreover, an 85-nm-wide reflection band centered at $\lambda = 1350$ nm has an ultra-high reflectance with efficiency exceeding 99.9% and parts of that subband near 99.99%. We note that experimental performance of this class of devices is limited only by fabrication imperfections as its theoretical performance has been reported to exceed 99.99% for a wide wavelength band [18]. We note that in these measurements, the high reflectance band for the concatenated reflectors extends down to ~915 nm relative to ~960 nm for a single ZCG reflector. This is because of the high reflectance response in the TE-polarization state for an individual ZCG in the 920-980 nm band as rendered in Figure 6–4(c).

The experimental spectra in Figures 6–4(a) and 6–5 are fairly robust relative to small deviations in the angle of incidence. To quantify this, we set the input wavelength to 1350 nm and assess the behavior of the surrounding reflection band with extraordinarily-high efficiency for small variations in the polar angle of incidence, θ. For a ZCG mirror, as illustrated in Figure 6–1(a), we assume that the incident wave vector remains in the x-z plane and θ is defined as the angle between the wave vector and the z-axis. Results from

71
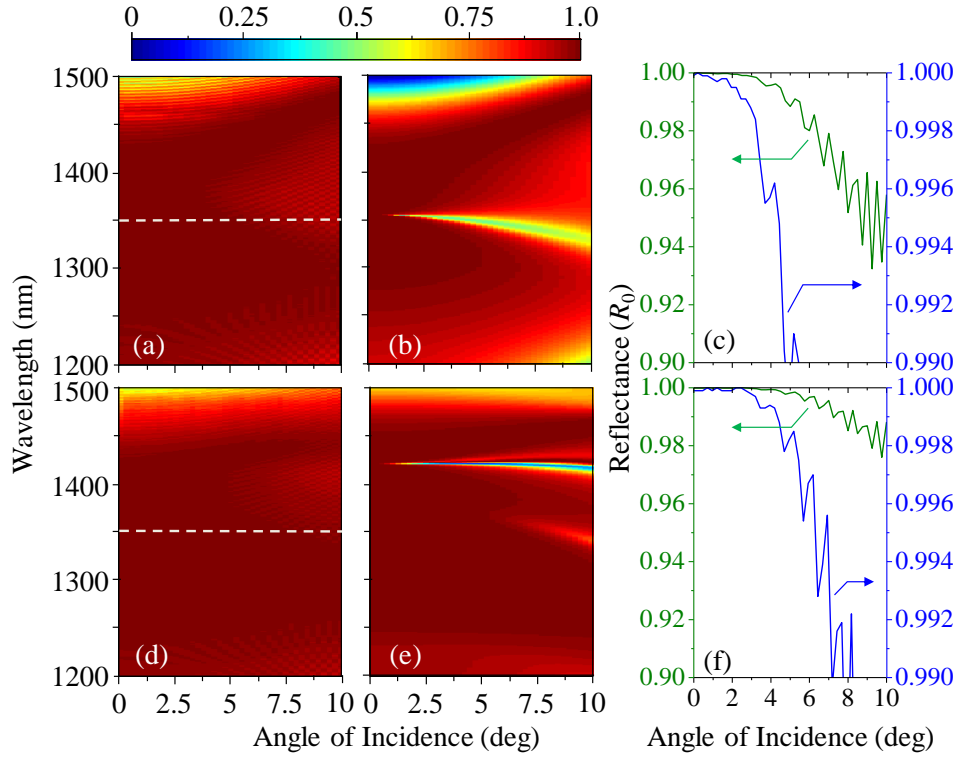
Figure 6-6 Angle-dependent spectral response. (a) Measured and (b) simulated R_0 maps for different polar angles corresponding to an elemental ZCG mirror for TM-polarized light incidence. (c) Angular R_0 corresponding to λ = 1350 nm in (a). (d)-(e) R_0 maps for concatenated ZCG mirrors for unpolarized light incidence showing (d) measurement and (e) simulation results. (f) Angular R_0 corresponding to λ = 1350 nm in (d). In the measurements, R_0 is approximated as $1 - T_0$. Dashed lines in (a) and (d) represent λ = 1350 nm.

this study are presented in Figure 6–6. Measured and simulated angle-dependent

reflectance maps corresponding to a polarization-dependent ZCG under TM-polarized

light incidence are shown in Figures 6–6(a) and 6–6(b), respectively. Similar maps for

unpolarized light corresponding to serial devices as in Figure 6–2 are shown in Figure 6–

6(d) for measurement and Figure 6–6(e) for simulation. Figures 6–6(c) and 6–6(f) show

experimental data of R_0 vs. θ at λ = 1350 nm corresponding to Figures 6–6(a) and 6–6(d),

respectively. These experimental results show robust performance of both types of
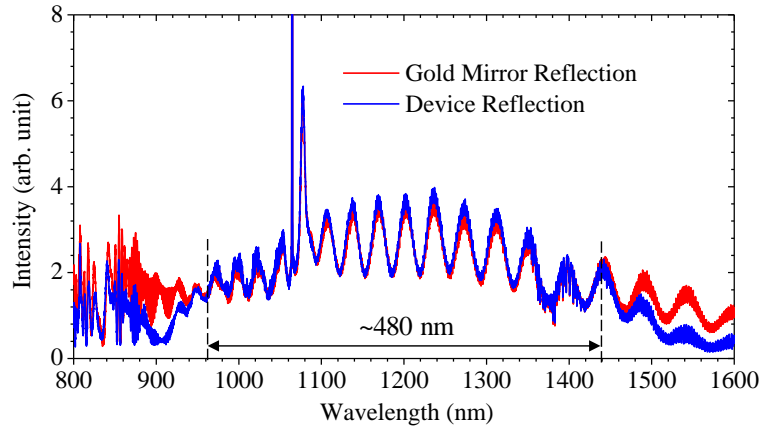
Figure 6-7 Reflection comparison with a gold mirror. Measured reflection intensities using a gold mirror (red line) and an elemental ZCG mirror (blue line) for TM-polarized light at normal incidence are shown. For a ~480-nm-wide spectral band centered at ~1230 nm, the measured intensity for the ZCG device is generally higher than the measured intensity for the gold mirror. The intensity spike at λ ~1060 nm is characteristic of the light source used in the measurement.

reflectors for small angular variations. For instance, at $\lambda = 1350$ nm, $R_0 \geq 99.9\%$ is sustained for $\theta \leq 2.75°$ for the polarized ZCG reflector whereas this value of R_0 maintains for $\theta \leq 4.25°$ for the unpolarized configuration. At the same wavelength, $R_0 \geq 99\%$ covers up to 4.75° and 7.75° in θ for these polarization-dependent and polarization-independent cases, respectively.

Finally, measured reflection intensity of the sputtered gold mirror in comparison with the reflectance of one of our ZCG reflectors is shown in Figure 6–7. TM polarization and a normal angle of incidence are employed. Here, for ~480-nm-wide wavelength range from ~960 nm to ~1440 nm, the measured reflectance of the grating device is generally on par or higher than that of the gold mirror. This implies that device reflectivity at the marked ~480-nm-wide band is >98% as claimed above. This is consistent with the experimental results presented in Figure 6–4(a). This supports our use of the approach taken in this research that $R_0 = 1 - T_0$ is a reliable way to quantify our devices.

Conclusions

In summary, we report successful design, fabrication, and characterization of unpolarized high-efficiency broadband mirrors based on subwavelength c-Si gratings. Our sequential arrangement concept is fundamentally different from coupled woodpile gratings and 2D photonic crystals previously reported in the literature. In fact, our unpolarized reflectors possess the extremely wide polarization-dependent reflection bands obtainable with optimized 1D ZCGs [18]. The relative bandwidth, defined as the ratio of unpolarized-reflection bandwidth ($\Delta\lambda$) for R_0>97% and center wavelength (λ_C), in our experiments, is $\Delta\lambda/\lambda_C$ ~44%. For comparison, the relative unpolarized-reflection bandwidths for the woodpile structure designed by Zhao *et al*. [78] and the 2D ZCG grating structure proposed by Ko *et al*. [77] are ~14% and ~24%, respectively. Generally, in 2D, or coupled 1D, resonant reflectors, the unpolarized reflection bandwidth is limited by a less-reflective polarization state. In contrast, a fractional band with high TE reflectance adjacent to the wide TM band provided by the ZCG reflectors reported here actually extends the unpolarized bandwidth. This is shown by our numerical and experimental results. In design and optimization of reflectors belonging to the device class presented herein, bandwidth enhancement by such means should be considered.

In spite of the conceptual simplicity of the ideas presented herein, their practical significance is potentially enormous. The basic polarized ZCG reflectors have simple design, robust performance, and are straightforward to fabricate. Hence, this technology may be a promising alternative to multilayer thin-film reflectors particularly at longer wavelengths of light where film deposition may be infeasible or impractical.

Chapter 7

Divergence-tolerant resonant bandpass filters

Optical devices based on resonant gratings include broadband mirrors [18,52], biosensors [20], spectral filters [14,54,72], polarizers [21], and beam-transforming meta-surfaces [55]. These devices operate under the guided-mode resonance mechanism [25,70] that incorporates resonant coupling to leaky Bloch modes in the waveguide-grating layer system. The resultant spectra are engineered by selection of device materials and parameters to meet specifications for a desired application. Recent work in this field indicates potential to create spectrally narrow and efficient optical filters with high quality (Q) resonances [57,81]. Whereas narrow-linewidth spectral filters are attractive for many applications, including sensing and communications, in practice, in some cases, they may not be able to accommodate the angular divergence of finite-size beams. This motivates the aim of the present contribution which is to improve the angular tolerance of resonant bandpass filters.

Previous studies addressing angular tolerance of guided-mode resonance (GMR) devices treat reflection-type spectral filters with complex grating structures [82-85]. For example, Lemarchand *et al.* conducted a theoretical study and showed that doubly periodic resonant gratings considerably improve the angular tolerance without affecting the spectral bandwidth [82]. A later experimental demonstration by the same group provided a four-layer stack with two-dimensional (2D) periodicity and a top layer containing circular air holes with differing radii [83]. They reported improved angular tolerance and polarization independence [83]. Another means to achieve increased angular stability

involves use of a standard GMR filter surrounded by Bragg reflectors. This geometry has recently been referred to as cavity-resonator-integrated guided-mode resonance filter [84]. Buet *et al.* applied this geometry to design and fabricate a filter with a relatively narrow linewidth and an angular tolerance of several degrees at normal incidence [85].

In this Chapter, we investigate the angular response of a single-layer GMR bandpass filter with 1D periodicity under fully conical incidence and compare with classical incidence. In fully conical mounting, the plane of incidence (POI) is orthogonal to the grating vector of the periodic surface. On the other hand, in classical mounting, the POI is parallel to the grating vector. We report theoretical and experimental results demonstrating that the full conic mount provides considerably larger angular linewidth than its classical counterpart for the particular filter under study. Moreover, we provide physical explanations for the properties observed.

Device Structure

The bandpass filter structure shown in Figure 7-1(a) is based on a crystalline-silicon (c-Si, refractive index = 3.48) grating on a quartz (refractive index = 1.51) substrate. The top c-Si film resides on the xy-plane and the c-Si grating vector is along the x-axis. The grating geometry is defined by the period Λ, ridge-width $f\Lambda$ (where f is the fill factor), c-Si film thickness t, and grating height d_G. As d_G < t, this is a zero-contrast grating design [18]. A calculated zero-order transmittance (T_0) spectrum for the set of parameters reported in Chapter 4 for normally incident transverse-electric (TE) polarized light is shown in Figure 7-1(b); see figure caption for device parameters. Normal incidence is defined by the incident wave vector (k_i) pointing along the z-axis. Input light is in the TE (as opposed to transverse magnetic, TM) polarization state when the incident electric field, E_i, (magnetic
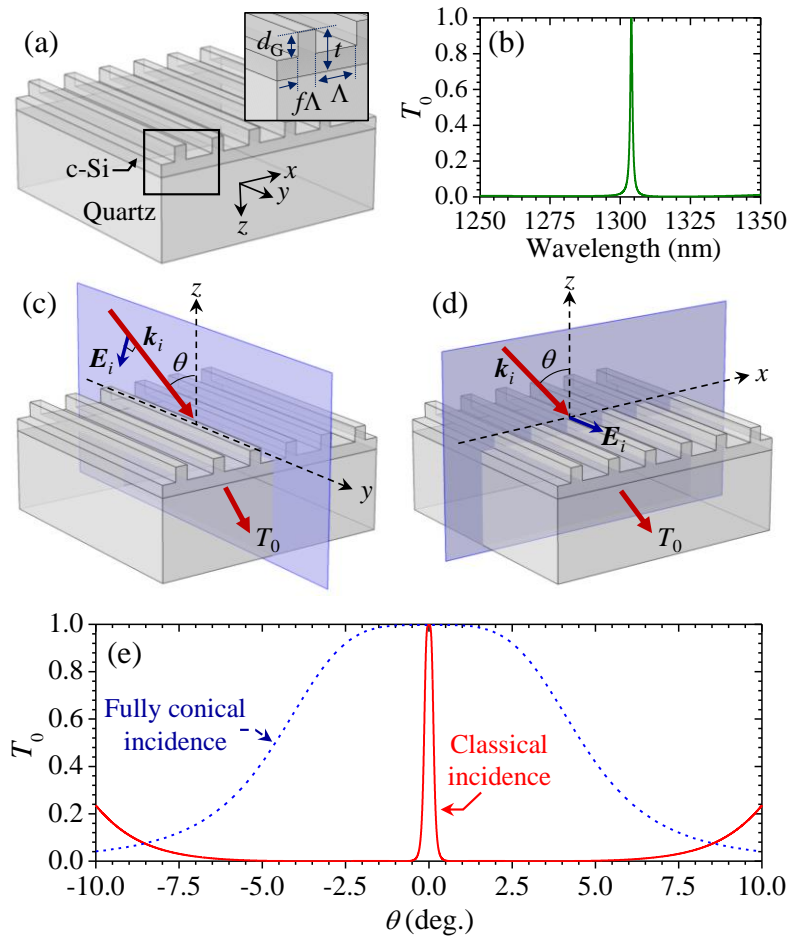
Figure 7-1 Comparison between fully conical and classical light incidence. (a) Structure of a device with a c-Si grating on a quartz substrate showing period Λ, fill factor f, film thickness t, and grating height d_G. (b) Calculated zero-order transmittance (T_0) for TE polarized light at normal incidence for a filter with parameters $\Lambda = 860$ nm, $f = 0.24$, $t = 520$ nm, and $d_G = 277$ nm. (c) Schematic representation of fully conical incidence where incident wave vector (k_i) and electric field (E_i) fall on the yz-plane. (d) Schematic representation of classical incidence where k_i falls on the xz-plane and E_i is along the y-axis. In (c) and (d), θ is the angle of incidence. (e) Computed angular T_0 plot at peak wavelength $\lambda = 1304$ nm.

field, H_i, for TM) points along the y-axis. Numerical calculations are carried out using Rsoft DiffractMOD.

Schematic illustrations of fully conical and classical mounts are presented in Figures 7-1(c) and 7-1(d), respectively. For full conical incidence in Figure 7-1(c), the POI is the yz-plane and both k_i and E_i lie in this plane and are orthogonal to each other. For

classical incidence in Figure 7-1(d), the POI is the xz-plane, $\boldsymbol{k_i}$ lies on the POI, and $\boldsymbol{E_i}$ is along the y-axis. For both mounts, the angle of incidence, θ, is the angle between k_i and the z-axis. A calculated T_0 plot for fully conical and classical incidence between $\theta = \pm 10°$ at T_0-peak wavelength $\lambda = 1304$ nm is shown in Figure 7-1(e). There, the fully conical incidence shows a much larger acceptance angle compared to the classical incidence. The computed angular full-widths-at-half-maximum (FWHM) linewidths, $\Delta\theta$, are 9.2° and 0.29° for fully conical and classical incidence, respectively. This enlarged $\Delta\theta$ is potentially useful in applications demanding high angular tolerance.

Wave-vector analysis

The wave vectors associated with m-th order diffraction by the gratings in Figure 7-1 obey the following equations:

$$\text{(classical) } k_{x,m} = k_i \sin\theta + m(2\pi/\Lambda), k_{y,m} = 0, \tag{7.1}$$

$$\text{(full conical) } k_{x,m} = m(2\pi/\Lambda), k_{y,m} = k_i \sin\theta, \tag{7.2}$$

where $k_{x,m}$ and $k_{y,m}$ are the components along the x- and y-axes, respectively. As discussed in Chapter 3, the T_0 peak in Figure 7-1(b) is formed by second-order coupling ($m = \pm 2$) to the fundamental mode TE_0 whereas the wide background is established by first-order ($m = \pm 1$) coupling to the TE_2 mode. The angular variation of the second-order diffracted wave in the c-Si grating layer ($|\Delta k_{diff}|$) is defined as

$$\left|\Delta k_{diff}\right| = \left\|\left|k_{diff}\right| - \left|k_{diff}\left(\theta = 0°\right)\right|\right\|. \tag{7.3}$$

Using Eq. 7.3, the angular variations of the second-order diffracted wave for classic ($|\Delta k_{diff}|_{classic}$) and full conic ($\Delta k_{diff}|_{fully\ conic}$) mounts are expressible as

$$\left|\Delta k_{diff}\right|_{classic} = k_i \sin\theta, \tag{7.4}$$
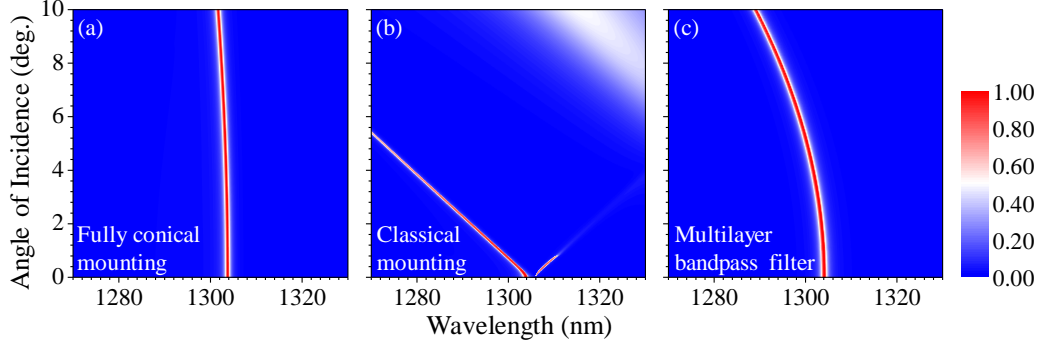
Figure 7-2 Calculated angle-dependent T_0 maps for (a) fully conical and (b) classical incidence for the bandpass filter in Fig. 1(a). (c) Angle dependent T_0 map for the 15-layer Si/SiO$_2$ multilayer bandpass filter presented in Figure 4-1(b) of Chapter 4.

$$\left|\Delta k_{diff}\right|_{fully\,conic} = \sqrt{\left(k_i \sin\theta\right)^2 + \left(4\pi/\Lambda\right)^2} - 4\pi/\Lambda. \tag{7.5}$$

In the subwavelength regime ($\Lambda < \lambda_0$), Eq. 7.5 can be re-rewritten in terms of $\left|\Delta k_{diff}\right|_{classic}$ by a Taylor series expansion as

$$\left|\Delta k_{diff}\right|_{fully\,conic} = \frac{4\pi}{\Lambda}\left\{\sqrt{\left(\frac{\Lambda}{4\lambda_0}\sin\theta\right)^2 + 1} - 1\right\} \approx \sin\theta\left(\frac{\Lambda}{4\lambda_0}\right)\left|\Delta k_{diff}\right|_{classic}. \tag{7.6}$$

Consequently, from Eq. 7.6, it is clear that $\left|\Delta k_{diff}\right|_{fully\,conic}$ is always smaller than $\left|\Delta k_{diff}\right|_{classic}$. In fact, for small θ, the angular variation of the second diffraction orders in fully conical mounting is much smaller than its classical counterpart. It is this stable second-order diffraction that enables the observed relatively angle-insensitive bandpass filtering under fully conical incidence. We recall that the leaky modes responsible for the resonance effects foundational to the operation of all GMR devices, including the bandpass filters presented here, are driven by these evanescent diffraction orders by phase matching [5].

A calculated λ-θ T_0 map under full conic incidence is provided in Figure 7-2(a). Shown there is excellent stability in angle, spectral profile, linewidth, and efficiency.

Changing the angle from $\theta = 0$ to 10°, the T_0-peak wavelength exhibits a 2-nm blue shift

from $\lambda = 1304$ nm to 1302 nm. This blue shift can be understood by analyzing the angular

variation of the second-order diffracted wave vector driving the associated leaky modes.

The propagation constant of a leaky mode is a complex number and its real part can be

approximated by $\beta_m = \left| k_{x,m}\hat{x} + k_{y,m}\hat{y} \right|$ [25]. Thus, the incident wave satisfies phase matching

with wave vector β_m where m denotes the excitation order; here $m = \pm 2$. From Eq. 7.2, for

full conic incidence, we find that the $m = -2$ and $m = +2$ orders of wave vectors are identical

and expressible as

$$\beta_{\pm 2, full\ conic} = 2\pi \sqrt{\left(\frac{\pm 2}{\Lambda}\right)^2 + \left(\frac{\sin\theta}{\lambda_0}\right)^2}.$$ (7.7)

As indicated by Eq. 7.7, this quantity decreases slowly with θ. As θ increases,

$\beta_{\pm 2,\ full\ conic}$ increases and the resonance wavelength decreases. This explains the blue shift in

Figure 7-2(a). Similarly, for the classical incidence, the features of the λ-θ loci in Figure 7-

2(b) are explainable by $\beta(\theta)$ expressed as

$$\beta_{-2,classic} = 2\pi \left(\frac{2}{\Lambda} - \frac{\sin\theta}{\lambda_0}\right), and$$ (7.8)

$$\beta_{+2,classic} = 2\pi \left(\frac{2}{\Lambda} + \frac{\sin\theta}{\lambda_0}\right)$$ (7.9)

As θ increases, the backwards diffracted wave vector ($m = -2$) decreases but the

forward diffracted wave vector ($m = +2$) increases. Thereby, the resonance wavelength is

split due to large red- and blue shifts with angle as originally presented in [25] and later

verified experimentally in [12]. The T_0 map under classical incidence displays a drastic,

almost-linear blue shift in the T_0-peak wavelength at a rate of ~6 nm per deg. In addition,
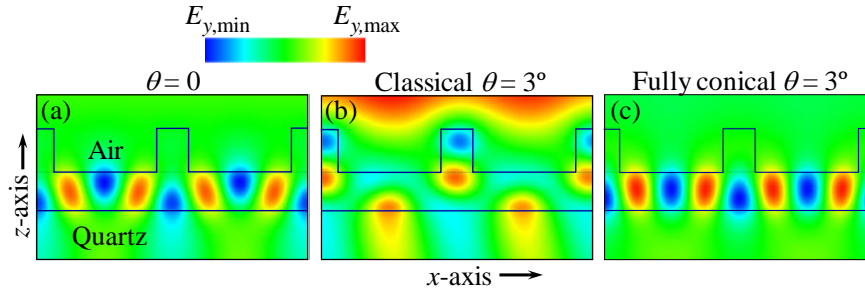
Figure 7-3 Internal electric field (E_y) profile at λ = 1304 nm for (a) normal incidence, (b) classical incidence at θ = 3° and (c) fully conical incidence at θ = 3°.

operating under classical incidence invites a secondary broad resonance at longer wavelengths as seen in Figure 7-2(b); at θ = 10°, the transmittance is ~60%. This peak arises by coupling of the m = +1 order to a TE_1 mode.

For comparison, in Figure 7-2(c), we show an angle-dependent T_0 map of the 15-layer Si/SiO_2 thin-film bandpass filter in Chapter 4. The multilayer device consists of a 14-layer Si/SiO_2 quarter-wave Bragg stack with an embedded half-wave SiO_2 defect layer; this filter is designed to operate at λ = 1304 nm. In Figure 7-2(c), the multilayer device exhibits an angularly robust bandpass profile for θ < 2°. At larger θ, the T_0-peak wavelength rapidly blue-shifts to λ = 1280 nm at θ = 10°. The blue-shift of the multilayer bandpass filter is understood by modeling it as a Fabry-Perot etalon [86]. In Figure 7-2, it is clear that the resonant subwavelength filter under fully conical mounting provides the most angularly-stable bandpass performance.

For added clarity, we plot the internal electric field (E_y component) profile for normal, classical, and fully conical incidence in Figure 7-3 illustrating the E_y profile in a cross-sectional xz-plane over two grating periods. The internal electric field for normal incidence and T_0-peak wavelength λ = 1304 nm is shown in Figure 7-3(a). There, the guided waves constituting a TE_0 mode form a standing wave pattern residing primarily in the

homogeneous c-Si layer. The E_y profile for classical incidence at $\theta = 3°$ and $\lambda = 1304$ nm is depicted in Figure 7.3(b). Unlike Figure 7-3(a), where the incident light is fully transmitted, in Figure 7-3(b) the input light is fully reflected, resulting in concentration of electric fields above the grating layer as depicted. At $\theta = 3°$ for fully conical incidence, $T_0 \approx 0.85$ at $\lambda = 1304$ nm with corresponding E_y profile as shown in Figure 7-3(c). There, the guided-mode is a TE_0 mode coupled to the second diffraction order — this is similar to the mode at $\theta = 0°$ in Figure 7-3(a). Hence, as expected for small values of θ, fully conical incidence does not induce a significant change in the second diffracted waves in the c-Si layer and they continue to drive the TE_0 modes supporting a bandpass spectrum. As the angle increases, the propagation constants acquire increasing y-components as in the analogous case of resonance reflection [87].

Experimental Demonstration

Device fabrication and measurements

To experimentally demonstrate the extraordinary angular tolerance associated with full conical mounting, we use a bandpass filter fabricated with the silicon-on-quartz (SOQ) platform. The SOQ wafer contains a 520-nm thick c-Si film on a quartz substrate. The device fabrication steps include UV interference lithography to create a photoresist mask, pattern-transfer to the c-Si film in a reactive ion etcher using a CHF_3 and SF_6 gas mixture, and removal of residual photoresist through O_2 ashing. The measured geometrical parameters of the fabricated device are $\Lambda = 856$ nm, $f = 0.21$, and $d_G = 272$ nm. For spectral measurements, we use a super-continuum light source and a near-infrared optical spectrum analyzer. Our input beam is appropriately polarized and well collimated with ~1 mm spot size. The sample is placed on a rotation stage for θ control. We measure

the intensities of the input and transmitted signals and calculate T_0 as measured signal normalized by the input signal; the input signal is directly measured with sample removed from the beam path. In the measurements, we employ a spectral resolution of 0.1 nm and angular resolution of up to 0.02°.

Measured spectra

Measurement results for full conical and classical incidence are presented henceforth. Figure 7-4(a) provides an experimental T_0 map for full conical incidence demonstrating bandpass characteristics with angularly tolerant peak location, maintaining both efficiency and linewidth with angle. Consistent with the theoretical computations,
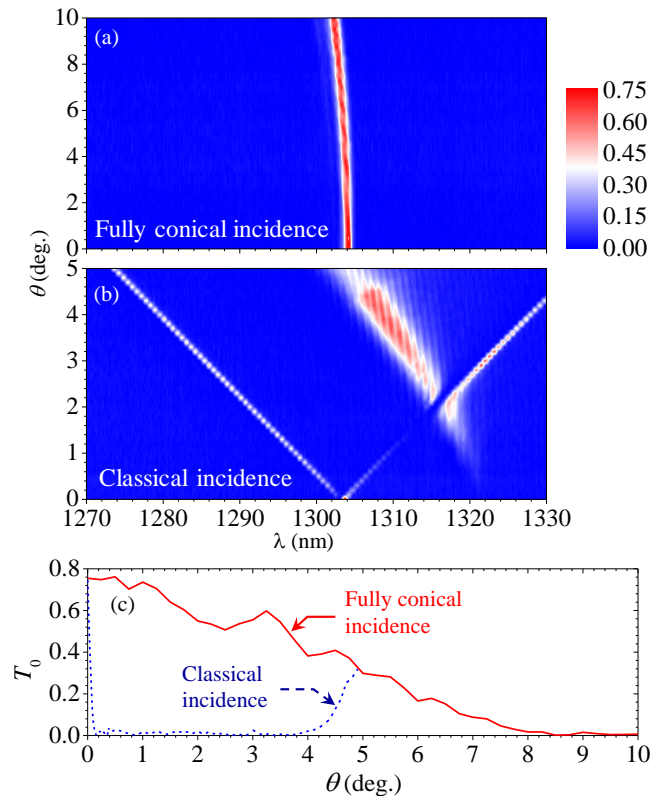

Figure 7-4 Measured angle-dependent T_0 maps for (a) fully conical and (b) classical incidence. (c) T_0 comparison between fully conical and classical incidence at $\lambda = 1304$ nm. Whereas the abscissa in (a) and (b) is the same, in (c) the T_0 plot for classical incidence covers only $\theta = 0$–5°.

from $\theta = 0°$ to $\theta = 10°$, the T_0 peak wavelength blue shifts by ~2 nm from λ = 1304.2 nm to λ = 1302.3 nm. The experimental T_0 spectrum for fully conical incidence in Figure 7-4(a) is in an excellent quantitative agreement with the theoretical prediction in Figure 7-2(a). Similarly, the T_0 map for classical incidence in Figure 7-4(b) shows a split in the T_0 peak at off-normal angles. The experimental results in Figure 7-4(b) are generally consistent with the theoretical T_0 map in Figure 7-2(b). In the experiment, a broad secondary resonance in the ~1300-1320 nm wavelength range at $\theta > 1°$ is seen. This resonance is observed at longer wavelengths in Figure 7-2(b). Figure 7-4(c) shows measured conical and classic $T_0(\theta)$ at λ = 1304 nm. There, fully conical and classical mountings exhibit angular FWHM linewidths ($\Delta\theta$) of 9.5° and 0.1°, respectively. Hence, the experimental full-conic bandpass filter exhibits ~95x the angular stability of its classical counterpart.

Conclusions

In summary, we provide herein the main angular-spectral characteristics of resonant bandpass filters employing the zero-contrast grating architecture. Fundamentally, in these filters, the transmission peak forms by second-order diffractive coupling to a fundamental TE_0 mode whereas the wide, low background is established by first-order coupling to a TE_2 mode. Slow angular variation of the central wavelength in fully conical mounting is provided by a concomitant slow angular variation of the resonant second diffraction orders driving the pertinent leaky modes. We show theoretically and experimentally that the full conical mount provides improved angular stability relative to the classic mount. Our experimental bandpass filter possesses a nearly 100-fold angular aperture under full conic incidence relative to its classical counterpart. We also show that full conical incidence preserves the bandpass spectral profile, including peak efficiency

84

and linewidth. High angular tolerance in full conical mount is characteristic of narrow linewidth filters supported by the guided-mode resonance effect in view of the physical explanations put forth herein. Thus, improved angular tolerance for reflection-type filters is also expected as recently treated by Peters *et al*. [88].

As the device is one-dimensional, the widened full conic angular aperture accommodates cylindrical wavefronts directly. Gaussian laser beams will be accepted partially with widened aperture along the grating grooves but limited by the classic-incidence bandwidth transverse to that direction. Thus, a Gaussian beam illuminating the filter treated here at normal incidence would pass with an approximate elliptical beam profile.

This research can be extended to the design and development of resonant bandpass filters that are angularly robust for arbitrary azimuthal angles of incidences. Extension to multiple alternate spectral regions is also of interest. Bandpass filters are applicable in many fields including display, spectroscopy, sensing, communications, and astronomy. Developing improved, materially-sparse bandpass filters that maintain narrow bandwidths while accommodating practical divergent beams is thus an important pursuit.

Chapter 8

Guided-mode resonant photonic lattices

There is a considerable current scientific interest in resonant dielectric films and related devices for optical applications such as broadband mirrors [17,18,89], spectral filters [53,54,72], and polarizers [21,90]. These devices operate under the guided-mode resonance (GMR) mechanism where light diffracted by the grating couples to one of more leaky modes supported by the high-index slab waveguide under a phase-matching condition [70]. A one dimensional grating has different phase-matching conditions for s- and p-polarized input; thus a guided-mode resonance in a resonant grating is dependent on the polarization of input light [17,21,90]. On the other hand, a resonant lattice with identical periodicity in both directions, *i.e.* 4-fold rotational symmetry, is unpolarized at normal incidence [53,54]. While early research work has mostly focused on resonant gratings that are periodic along one dimension (1D), 2D photonic lattices, also called 2D waveguide gratings, are of interest for their potentially unpolarized nature even though the fundamental resonance mechanisms are the same in both geometries.

Designing a polarized grating is relatively easy thanks to the ability to optimize a set of device parameters for an application by means of efficient inverse numerical methods [14,15]. An example of such techniques is particle-swarm optimization (PSO) [31] that utilizes a rigorous coupled-wave analysis (RCWA) [28] algorithm for the forward computations. Compared to 2D periodic resonance elements, numerical solutions of resonant gratings require considerably less computational power with computation time ~x100 or larger for resonant 2D devices in representative cases. This motivates the idea of
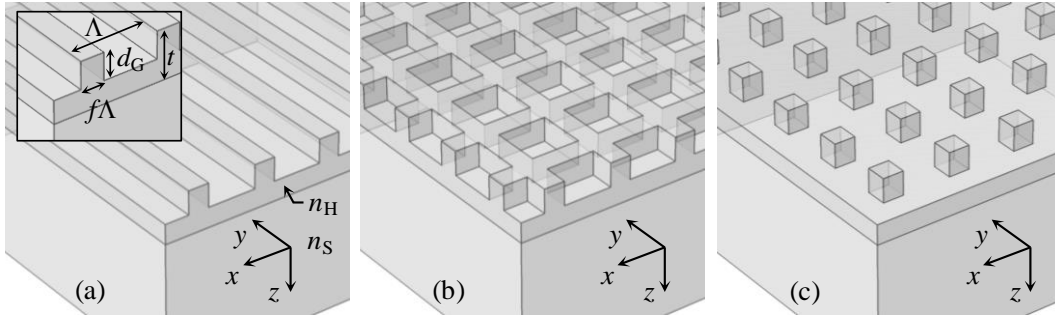
Figure 8-1 Structure of a resonant grating and photonic lattices. (a) Resonant grating structure comprising of a partially etched film of index n_H on substrate of index n_S. The grating geometry is defined by period Λ, film thickness t, grating depth d_G, and grating fill-factor f. (b) Square-hole photonic lattice corresponding to the resonant grating structure in (a). In (b), the orthogonal grating ridges in x- and y-directions are identical and have the same periodicity, depth, and fill factor as the gratings in (a). (c) Square-post photonic lattice corresponding to the partially etched resonant grating in (a). The posts in (c) also have the same periodicity, depth, and fill factor along the x and y axes.

seeding the design of a 2D resonant lattice by the more expedient design of a 1D GMR filter.

Accordingly, we present a study on design and fabrication of unpolarized photonic lattices operating under the guided-mode resonance effect. In the context of a resonant narrow-linewidth bandpass filter, we develop a design method accomplishing direct conversion from a polarized resonance grating to an unpolarized lattice while maintaining approximately the set of design parameters and functionality. As conventional holographic double exposure produces circular or elliptical hole masks in photoresist, we explore a novel two-step resist liftoff method to create a square-hole hard mask for fabrication of the proposed photonic lattices. This study provides methods for expedient design and fabrication of unpolarized 2D resonant photonic lattices rooted in simple 1D GMR filters

.

Theoretical Study

Device structure

The canonical zero-contrast grating (ZCG) structure [18] in our consideration in Figure 8-1(a) consists of a dielectric film (refractive index = n_H) of thickness t on a substrate medium (n_S) and surrounded from above by cover medium (n_C). The film is partially etched with periodicity Λ, depth d_G, and ridge-width $f\Lambda$ where f is the fill-factor. The grating is periodic along the x-axis and its grooves are along the y-axis. For illumination at normal incidence, *i.e.* the incident wave-vector is along the z-axis, two polarization states are defined: transverse electric (TE) when the electric field (E) of the incident light is along the y-axis and transverse magnetic (TM) when the magnetic field (H) of the incident light is along the y-axis. As TE and TM polarized input light will experience a different grating structure, the spectral response of the grating in Figure 8-1(a) is polarized.

Two-dimensional "equivalents" of the polarized grating structure in Figure 8-1(a) can be represented as two distinct structures: a square-hole lattice in Figure 8-1(b) and a square-post lattice in Figure 8-1(c). A square-hole lattice consists of grating ridges that are periodic in both x- and y-directions with identical Λ and f as shown in Figure 8-1(b). There, the top film of index n_H and thickness t contains square holes of size $(1-f)\Lambda$, filled with cover medium (n_C), and partially etched to a depth d_G. Likewise, the square-post lattice in Figure 8-1(c) contains square posts of size $f\Lambda$ and height d_G for a total film-thickness t. These posts are spaced at a periodicity of Λ in both x- and y-directions. We note that in Figures 8-1(b) and 8-1(c), TE and TM polarized light waves in each case see an identical grating structure due to the lattice symmetry in x- and y-axes. The resulting device is, hence, unpolarized.
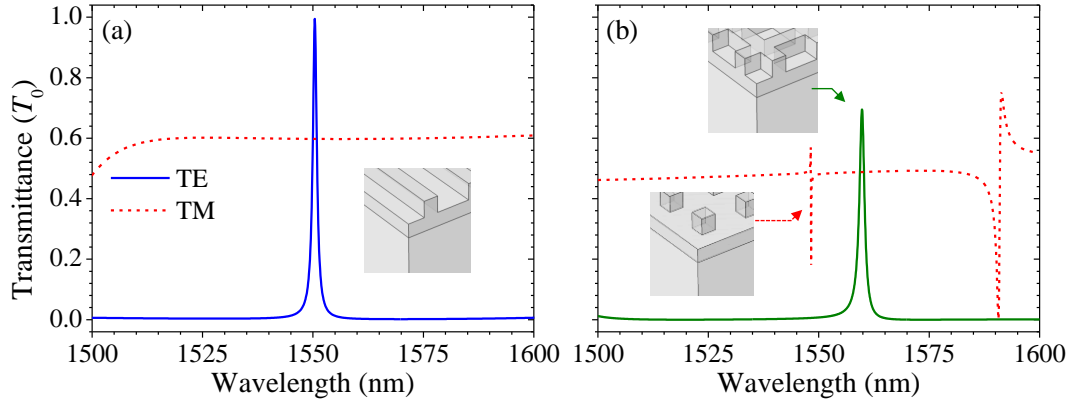
Figure 8-2 Calculated spectra. (a) Spectral response of partially etched Si resonant grating reported by Niraula *et al.* in [57]. Grating parameters are Λ = 1018 nm, f = 0.21, d_G = 355 nm, t = 652 nm. Refractive indices are n_H = 3.48, n_S = 1.45, and n_C = 1.0. The device operates as a bandpass filter at λ = 1550 nm for TE polarization (solid blue). TM polarized spectrum (dashed red) does not exhibit a GMR in the spectral band. (b) Spectral responses of square-hole (solid green) and square-post (dotted red) lattices applying the same grating parameters and materials as the device in (a). The 2D hole grating structure exhibits a bandpass filter profile at λ = 1560 nm.

An intriguing device application of GMR is a single-layer bandpass filter; this device in a ZCG format was initially proposed by Niraula *et al.* in [57] and later experimentally demonstrated in [72]. The partially etched bandpass filter proposed in [57] resembles the structure in Figure 8-1(a) with the following device parameters: n_C = 1.0 (air), n_S = 1.45 (SiO$_2$), n_H = 3.48 (Si), Λ = 1018 nm, f = 0.21, d_G = 355 nm, and t = 652 nm. Calculated zero-order transmittance (T_0) spectra for TE and TM polarizations corresponding to this structure are shown in Figure 8-2(a). There, TE polarization (solid blue) exhibits a bandpass profile centered at λ = 1550 nm with a full-width at half-maximum (FWHM) linewidth of $\Delta\lambda$ = 1 nm. TM polarization (dashed red) does not exhibit any GMR in the 1500-1600 nm band as shown in the figure. Here we note that if the grating is periodic in *y*- as opposed to *x*-axis, TM polarization will exhibit a bandpass profile while TE will not resonate. This observation raises an interesting question: can the device support an unpolarized

bandpass profile if the grating lines are periodic in both *x*- and *y*-directions (*i.e.* a 2D photonic lattice)?

We now apply the design parameters for the polarized grating in Figure 8-2(a) to square-hole and square-post lattices in Figures 8-1(b) and 8-1(c), respectively. Calculated T_0 spectra (unpolarized) corresponding to these lattices are shown in Figure 8-2(b). Whereas the square-post lattice exhibits two resonances with classic Fano-type shape in the spectral band, the square-hole lattice exhibits a bandpass profile with passband centered at $\lambda = 1560$ nm and a T_0-peak efficiency of 70% and a FWHM of $\Delta\lambda = 1$ nm. Thus, while a direct conversion of from a polarized grating to an unpolarized square-hole lattice in context of a bandpass filter is feasible, the resultant unpolarized T_0 profile exhibits a spectral shift and impaired efficiency although the sidebands remain low and broad. We conduct a modal and parametric study to investigate this conversion further.

Modal study

For convenience, we re-plot the T_0 spectra in Figures 8-2(a) and 8-2(b) in Figures 8-3(a) and 8-3(b), respectively. In Figure 8-3(a), the TE spectrum has a T_0-peak at $\lambda = 1550$ nm; corresponding simulated internal E field profile (*y*-component, *xz*-plane) over two grating periods is shown in Figure 8-3(c). There the E_y field profile shows a standing-wave corresponding to the second-order diffraction in the Si layer coupled to the TE_0 mode. It is this fundamental TE mode that forms the narrow passband as previously reported in [57]. Comparatively, the E_y profile for square-hole lattice (solid green) in Figure 8-3(b) at T_0-peak wavelength $\lambda = 1560$ nm under TE incidence is shown in Figure 8-3(d). Again, the guided-modes are driven by second-order diffraction coupled to the TE_0 mode; similar to the case of Figure 8-3(c). We remark that in the 2D case, there are modes running along
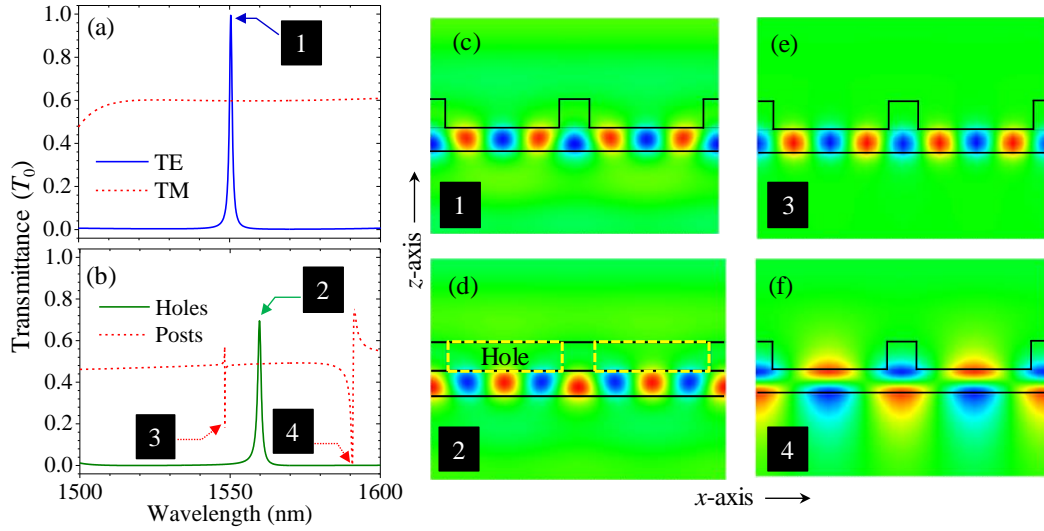
Figure 8-3 Study of internal field profiles at resonance wavelengths. (a) T_0 spectrum of resonant grating structure as shown in Fig. 2(a). (b) T_0 spectrum of square-post and square-hole lattices, as shown in Fig. 2(b). In (a) and (b), markings 1, 2, 3, and 4 denote GMR locations. (c)-(f) Internal electric-field (E_y) profiles for GMRs denoted by (c) 1, (d) 2, (e) 3, and (f) 4.

both x and y directions simultaneously for unpolarized light input. Here, it is worthwhile to note that at TM incidence we expect an E_x profile (over the yz-plane) identical to Figure 8-3(d).

The T_0 spectrum (dashed red) corresponding to the square-post lattice exhibits two Fano-type resonances with T_0-minima at λ = 1548.25 and λ = 1590.80, respectively. For TE incidence, E_y profile corresponding to λ = 1548.25 nm is shown in Figure 8-3(e). There, interestingly, the guided-mode is a fundamental mode excited by and coupled to the second diffraction order, similar to Figures 8-3(c) and 8-3(d). However, the first-order diffraction does not form a broad stopband around the TE$_0$ mode, necessary for bandpass profile under the double-resonance condition [57]. Instead, the first-order diffraction forms a relatively narrow Fano-resonance at λ = 1590.80 nm as shown by the E_y profile in Figure 8-3(f). Another interesting observation we make here is that the standing TE$_0$ modes

91

corresponding to T_0-peaks in Figures 8-3(c) and 8-3(d) exhibit a significant vertical oscillation as a result of interference between guided-modes coupled to second- and first-order diffraction [57]. These modes cooperatively support the double-resonance condition required for bandpass profile formation. In Figure 8-3(e), the E_y profile does not exhibit a significant vertical oscillation as the guided modes coupling to the second- and first-order diffraction are now separated, and non-cooperative.

Parametric study

Next, we conduct a parametric study to elucidate the conversion from a polarized 1D grating to the 2D unpolarized lattice. At this point, we focus on the square-hole lattice as it supports an unpolarized bandpass profile. The parameter of choice in this study is the grating fill factor, *f*. For the polarized grating in Figure 8-4(a), we vary the f_x, the fill-factor of the grating in the *x*-direction. Calculated T_0 maps for f_x variation from 0 to *f* (*i.e.* 0.21) for
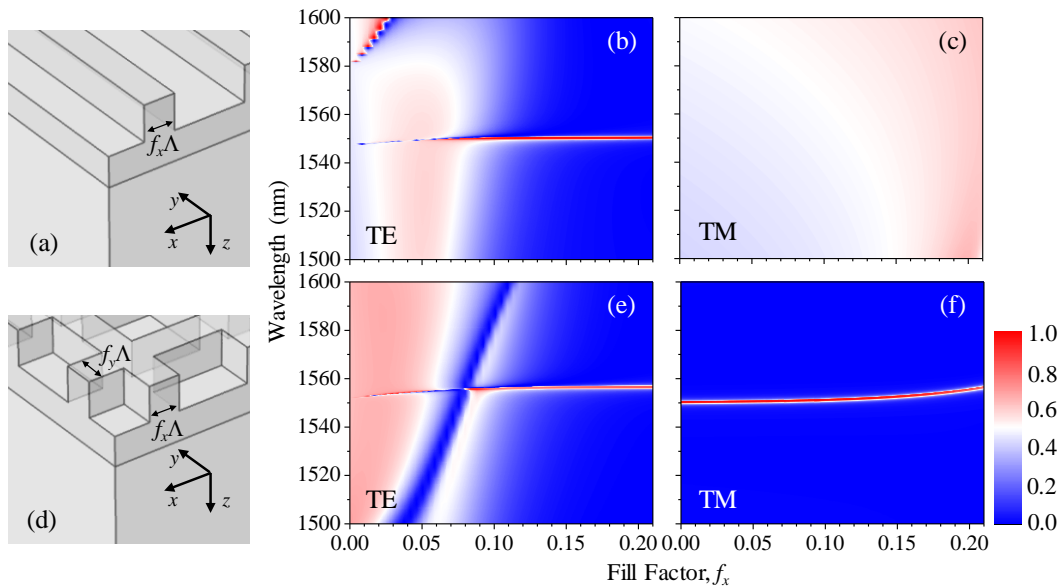

Figure 8-4 Parametric dependence. T_0 maps corresponding to the device in (a) for f_x variation from 0 to *f* for (b) TE and (c) TM polarizations. (d) Structure of a photonic lattice. T_0 maps corresponding to device in (a) for f_y = *f* and f_x variation from 0 to *f* for (e) TE and (f) TM polarizations. Other device parameters are the same as in Fig. 2.

TE and TM polarizations are shown in Figures 8-4(b) and 8-4(c). In Figure 8-4(b), for $f_x > 0$, a Fano-type resonance starts to form at ~1550 nm. As $f_x \to 0.21$, the stopbands start to form. Finally, at $f_x = f = 0.21$, the bandpass profile is complete. In contrast, TM polarization is non-resonant over the entire computational space as shown in Figure 8-4(c).

Similarly, for the lattice in Figure 8-4(d), we fix fill-factor of grating ridges in y-direction, $f_y = f = 0.21$ and vary f_x. Calculated T_0 map for TE polarization for f_x variation from 0 to f is shown in Figure 8-4(e). At $f_x = 0$, the structure resembles a polarized grating with incident E-field and grating vector both along the y-axis. As noted above, this condition does not support a GMR in the 1500-1600 nm spectral band. As $f_x \to 0.21$, a Fano-shaped resonance forms at ~1560 nm. Gradually, transmission stopbands start to form, and finally at $f_x = f_y = 0.21$, an unpolarized bandpass profile is complete. The T_0 map in Figure 8-4(e) exhibits a similar transformation as the T_0 map in 8-4(b) as in both cases the grating ridges along the x-direction diffract TE waves that support a bandpass profile. Likewise, the calculated T_0 map for TM polarized input for f_x variation from 0 to 0.21 is shown in Figure 8-4(f). There, $f_x = 0$ corresponds to a polarized grating with both H-field and grating vector along the y-axis; this condition is resonant with a bandpass profile centered at $\lambda = 1550$ nm. As $f_x \to f_y$, a slight redshift in T_0-peak location occurs, whereas the stopbands remain low. This is expected as the grating ridges periodic along the x-axis do not contribute to the resonant diffraction of TM polarized input.

In Figure 8-4(f), the slight shift in T_0-peak location and efficiency between $f_x = 0$ to $f_x = f_y$ is due to the perturbation in the resonant grating ridges along the y-axis caused by increase in f_x. For small values of f_x, the T_0-peak location is highly persistent and the effect of this perturbation is virtually non-existent. However, for larger f_x, its effect increases.
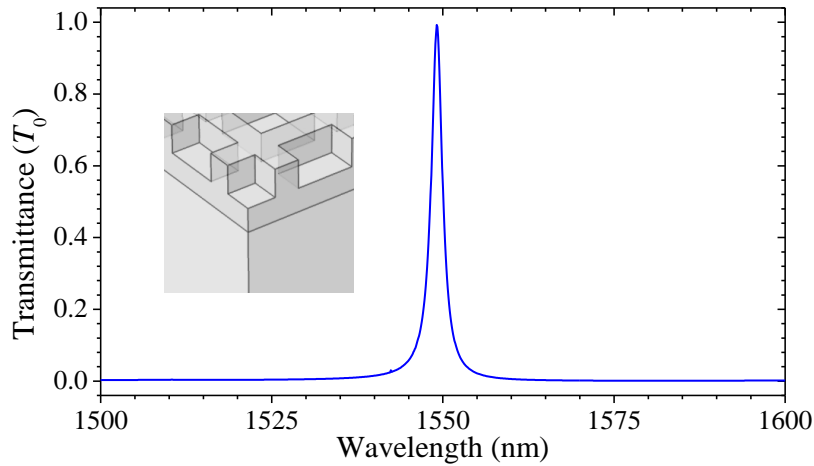
Figure 8-5 Calculated unpolarized T_0 spectrum of a square-hole photonic lattice as shown in inset with parameters Λ = 1018 nm, d_G = 366 nm, t = 655 nm, f = 0.18, n_H = 3.48, n_S = 1.45, and n_C = 1.0.

Whereas, in this example, the direct conversion only provides a ~70% unpolarized T_0 efficiency, the set of geometrical parameters thus deduced provide a good starting point to obtain higher performance through continued optimization. In Figure 8-5, we obtain peak T_0 efficiency approaching ~100% for an optimized 2D photonic lattice.

Mask Patterning for Square-Hole Lattice

For the devices considered here, we require square lattice geometry. Holographic lithography [6] is the technique of choice for mask patterning for the fabrication of polarized gratings. Compared to e-beam lithography, the holographic technique is fast and
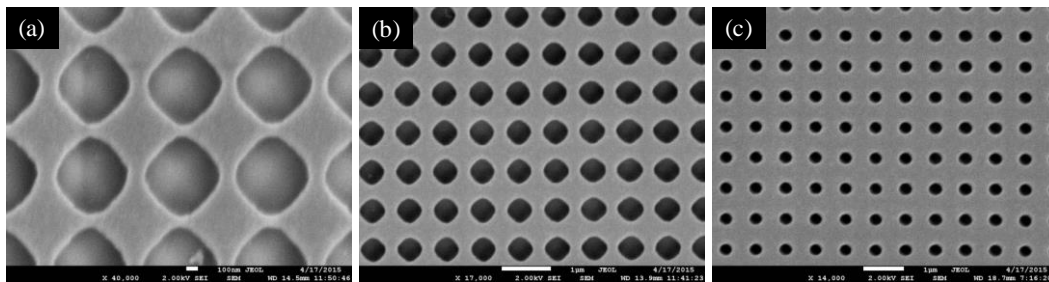

Figure 8-6 Top-view scanning electron micrographs of PR-mask lattice corresponding to (a) 10 second, (b) 15 second, and (c) 30 second holographic double-exposure. As the exposure duration is increased, the size of the holes decreases — this is characteristic of a negative PR.

can be used to fabricate a very large device. To create a 2D photonic lattice, a holographic double-exposure approach can be implemented. There, a photo-resist (PR) mask is exposed twice: the second exposure is orthogonal to the first exposure, and developed, resulting in a PR mask with hole or post lattices [91]. In our experiments, as a first step towards 2D resonant films for filters, we spin-coat a silicon wafer with ~400 nm thick layer of UVN-30, a negative PR. Our exposure beam is UV (266 nm) and highly collimated with a uniform intensity of ~26 $\mu W/cm^2$. We characterize the mask-patterning process by carrying out holographic exposures for different time durations; the first exposure is followed by sample rotation by 90° and re-exposure for the same duration. The exposed sample is then baked and developed in 917-MIF developer solution. Scanning electron micrographs (SEMs) of PR lattices patterned using this method are shown in Figure 8-6.

Figure 8-6 depicts some issues associated with the use of holographic double-exposure for photonic lattice fabrication. First, a square-hole mask profile is not attainable as the fabricated masks completely lack sharp profiles as needed for square patterning. This limitation can also be observed in the literature [91,92]. Second, large holes like the ones in Figure 8-6(a) require shorter exposure potentially preventing the PR mask from opening well onto the Si substrate. For longer exposures in Figures 8-6(b) and 8-6(c), the holes open down to the Si substrate. However, a photonic lattice intended for a particular application may require specific lattice geometry, especially for a high-Q GMR. Thus, the ability to fabricate a square-hole mask is important.

Two-step resist liftoff method

In the pursuit of sharp, clear square lattices, we implement a novel two-step resist-liftoff method as illustrated in Figure 8-7. We begin with PR coating, holographic exposure,
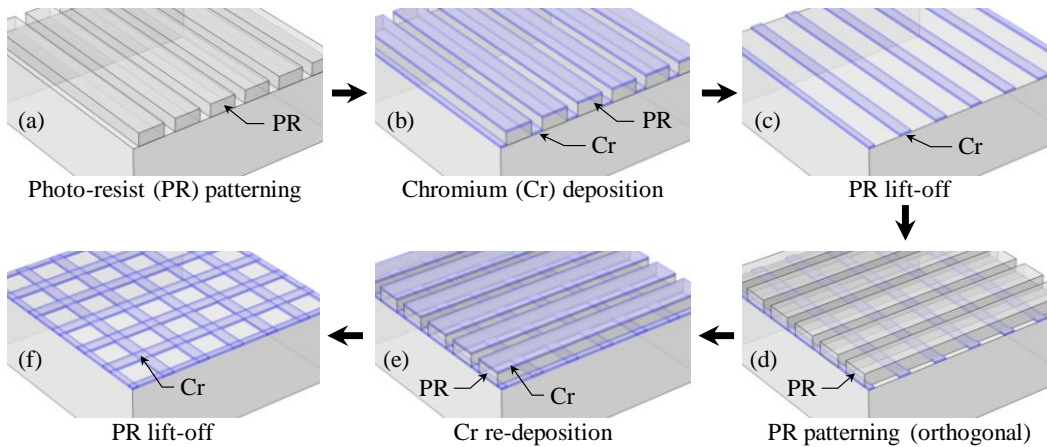
Figure 8-7 A two-step resist lift-off method for patterning square-hole mask. The fabrication steps include (a) photo-resist (PR) patterning via holographic lithography, (b) chromium (Cr) deposition via e-beam evaporation, (c) PR lift-off leaving behind Cr gratings, (d) re-patterning of PR at orthogonal direction, (e) re-deposition of Cr, and (f) PR lift-off for orthogonal Cr gratings with square openings.

and development to create patterned PR mask as shown in Figure 8-7(a). The PR grating

has a fill-factor 1 – f where f is the desired fill-factor of the final device. We then deposit,

via e-beam evaporation, a thin layer (~50 nm) of chromium (Cr), as shown in Figure 8-7(b).

E-beam evaporation offers highly directional deposition, thus the narrow trenches in a

high fill-factor PR mask can be filled with Cr with relative ease. The PR is then lifted off in

an ultra-sonic bath using AZ-400T, a PR stripper, leaving a Cr grating mask as shown in

Figure 8-7(c). Because the Cr grating is only ~50 nm thick, the wafer can be re-coated with

PR (~400 nm thick), exposed, and developed to create a patterned PR mask with grating

lines orthogonal to original lines, as shown in Figure 8-7(d). This is followed by Cr re-

deposition in Figure 8-7(e). Finally, after a second PR lift-off, orthogonal Cr gratings remain

in Figure 8-7(f). The Cr lines act as a hard mask for etching the substrate through the

square-hole openings.

A photograph of a wafer with an array of nine device areas is shown in Figure 8-8(a). Each device area contains a Cr square-hole mask, fabricated using the two-step resist
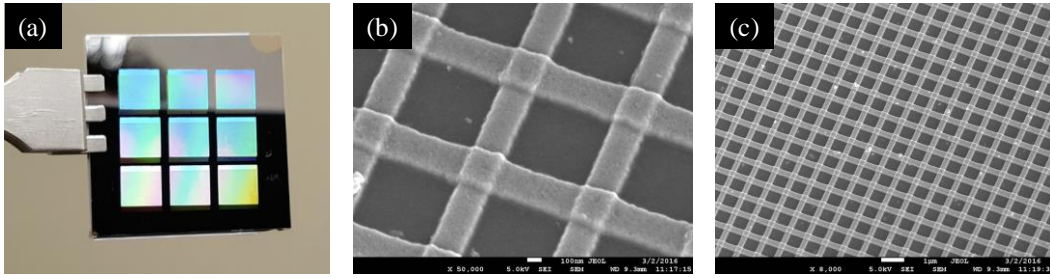
Figure 8-8 Fabrication results. (a) Photograph of a 1x1 inch² wafer with nine Cr square-hole mask device areas. (b),(c) Top-view SEM of a representative device area in (a). Estimated geometrical parameters in (b) are Λ = 850 nm and f = 0.30.

lift-off technique in Figure 8-7, with varying f and Λ parameters. Top-view SEMs of representative devices are shown in Figures 8-8(b) and 8-8(c). The square-holes in the figures are uniform and have relatively sharp edges. The mask pattern can be transferred to the substrate using reactive-ion etching technique for final device fabrication.

Conclusions

In summary, this paper presents a study on easy design and fabrication of photonic lattices operating under the GMR effect. A narrow-band resonance in a polarized grating can exist in an unpolarized square-hole lattice with similar grating parameters. This is feasible when the alternate polarization in a polarized grating is non-resonant; thus addition of an orthogonal grating does not significantly affect the resonance, especially in low-f devices where effect of perturbation due to non-resonant grating ridge in the orthogonal direction is relatively small as shown in Figure 8-4. As conventional holographic double-exposure limits the patterned resist mask to relatively circular-shaped holes, we propose a novel two-step resist lift-off method to fabricate hard metal mask with square holes for pattern transfer. Whereas 1D resonant gratings require less computational power to solve and optimize, 2D photonic lattices can be designed expeditiously using this approach shown herein to realize unpolarized filters.

Chapter 9
Future Work and Conclusions

The work presented in previous chapters can be extended to several more studies to improve the performance and applicability of proposed devices. The end of each chapter contains discussions about future work. In particular, the future study should consider fabricating unpolarized bandpass filters based on photonic lattices and concurrent spatial and spectral filters in transmission. The potential of work in these application areas is briefly discussed below.

Unpolarized Bandpass Filters

In Chapter 4, we demonstrate a resonant bandpass filter with narrow linewidth and low, flat stopbands. Although the 1D nature of the resonant grating limits the application of the device to TE polarization, the experimental demonstration proves the feasibility of single-layer resonant periodic devices in bandpass filtering applications. In the future, it is important to design single-layer polarization-independent bandpass filters.

In Chapter 8, we discuss the feasibility of converting a resonant grating design to an unpolarized photonic lattice maintaining the geometrical and performance parameters. There, we also propose a novel method of fabricating metal hard-mask for square-hole patterning. With the feasibility to easily design and fabricate, unpolarized bandpass filters based on square-hole photonic lattices is an important near-term pursuit.

Concurrent Spatial and Spectral Filter in Transmission

In Chapter 5, we present a novel class of non-subwavelength reflectors with concurrent spatial and spectral filtering capabilities. This work can potentially be extended
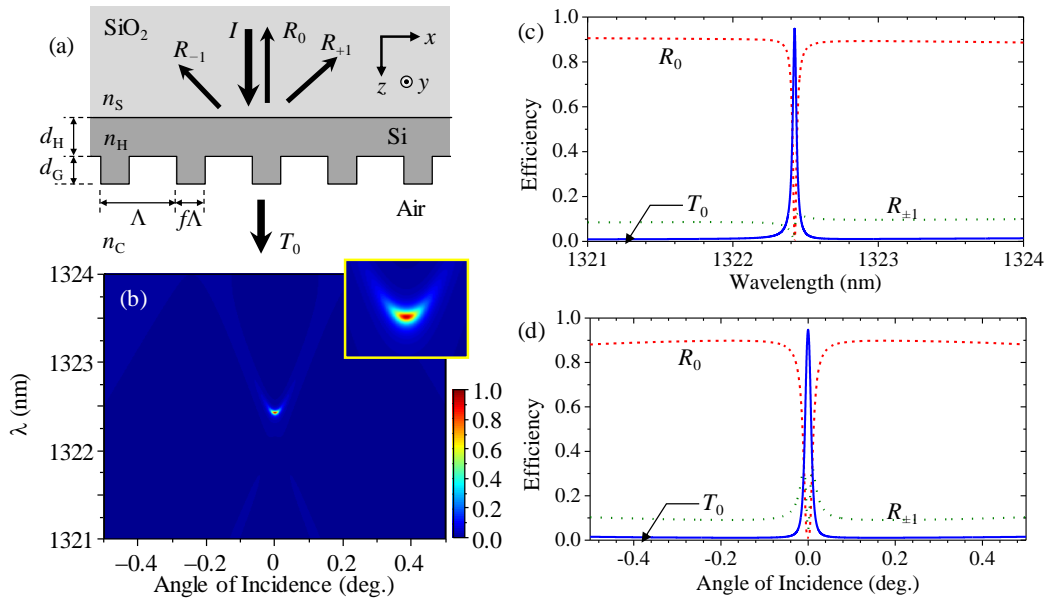
Figure 9-1 Calculated transmittance showing spatial/spectral delta function characteristics. (a) Device schematic. The geometry is defined by the grating period Λ = 1.15 μm; fill factor f = 0.36; total film thickness t = 3.07 μm and grating depth d_G = 160 nm. Refractive indices are n_F = 3.51 for the SiO$_2$ film, n_S = 1.52 for the glass substrate, and n_C = 1.0 for air. (b) Computed angle-dependent zero-order transmittance (T_0) spectrum the device under TE polarized light incidence (electric field vector along y. Efficiencies of all propagating orders at (c) normal incidence with varying wavelength and (c) at T_0-peak wavelength with varying angle of incidence.

to a concurrent spatial and spectral transmission filter operating in the non-subwavelength regime. A bandpass filter selective in the angular and wavelength domains can potentially be useful in focus-free spatial filtering, beam management, and solid-state light emission. Future work should consider both the experimental demonstration of the spectral/spatial selectivity in transmission as well as spatial filtering applications.

An example of a concurrent spatial and spectral filter in transmission is provided in Figure 9-1. Here, a partially etched silicon thin-film on a glass substrate as shown in Figure 9-1(a) is applied. The device is illuminated from the substrate to have higher-order diffraction in the substrate. The structure is optimized using the PSO algorithm for a

99

transmission resonance in the non-subwavelength regime (i.e. $\Lambda > \lambda_0/n_S$). See the figure captions for device parameters. The angle-dependent T_0 spectral map is shown in Figure 9-1(b). Here, like the R_0 peak in Figure 5-1(a), the T_0 peak is selective in both angle and wavelength. Simulated spectra at normal incidence are shown in Figure 9-1(c). There, the full-width at half maximum (FWHM) spectral linewidth of the resonance is $\Delta\lambda = 31$ pm. Similarly, the FWHM angular linewidth at the T_0-peak wavelength is $\Delta\theta_i = 0.0154°$ as shown in Figure 9-1(d). This, or similar, devices should be fabricated to verify these predictions.

Concurrent spatial and spectral filters based on resonant polarized gratings are limited to a specific light polarization. Future work should also consider the possibility of extending this to 2D photonic lattice architectures, as discussed in Chapter 8, for polarization independence. Feasibility of angular selectivity for conical incidence is an important pursuit.

Conclusions

Advancement in optical systems requires development of fundamental application areas. An example includes the ability to filter light. In this dissertation, we present theoretical and experimental studies on different classes of resonant periodic devices for optical filtering applications. Our study provides novel optical devices with simple structures, excellent performance, and significant reduction in fabrication time compared to the technology currently available. Namely, we show that single-layer partially etched device architectures can provide a similar bandpass filter performance as its multilayer counterpart employing a 15-layer Bragg stack. In experiment, we demonstrate a bandpass filter with sub-nanometer linewidth operating in the original

telecommunication band at wavelength 1304 nm. We also show that the angular tolerance of this class of bandpass filters can be improved ~95x by having the filter mounted at fully-conical incidence as opposed to classical incidence.

Similarly, we propose a novel concept for unpolarized wideband reflection through a sequential arrangement of two polarization-dependent 1D grating reflectors. In experiment, we obtain a relative bandwidth of ~44%, a record result for resonant reflectors. The technologies presented here can be a promising alternative to multilayer thin-film counterparts particularly at longer wavelengths where multi-layer quarter- and/or half-wave thin-film deposition may not be feasible.

We also identify a new class of resonant periodic devices with concurrent spatial and spectral filtering capabilities. This device is designed with carefully-crafted nanogratings operating in the non-subwavelength regime. We fabricate this device on TiO_2 on glass platform and obtain a reflection filter with ~4 mrad and ~1 nm angular and spectral linewidths, respectively. The experimental results presented in this dissertation demonstrate the feasibility of resonant periodic devices in practical applications. Relevant future work in this field is discussed and includes photonic lattices for unpolarized bandpass filtering and extending concurrent spatial and spectral filtering to transmissive and photonic lattice architectures.

Appendix A
List of Publications

Journal Publications

1. M. Niraula, J. W. Yoon, and R. Magnusson, "Mode-coupling mechanisms of resonant transmission filters," Opt. Express **22** , 25817-25829 (2014).

2. M. Niraula, J. W. Yoon, and R. Magnusson, "Concurrent spatial and spectral filtering by resonant nanogratings," Opt. Express **23**, 23428-23435 (2014).

3. M. Niraula, J. W. Yoon, and R. Magnusson, "Single-layer optical bandpass filter technology," Opt. Lett. **40**, 5062–5065 (2015).

4. M. Niraula and R. Magnusson, "Unpolarized resonance grating reflectors with 44% fractional bandwidth," Opt. Lett. **41**, 2482–2485 (2016).

5. M. Niraula and R. Magnusson, "Design and fabrication methods for unpolarized photonic lattices operating under guided-mode resonance," (Manuscript under preparation).

6. Y. H. Ko, M. Niraula[*], and R. Magnusson, "Divergence-tolerant resonant bandpass filters." (Manuscript under review). [*]*co-first author*

7. H. G. Svavarsson, B. H. Hallgrimsson, M. Niraula, K. J. Lee, and R. Magnusson, "Large arrays of ultra-high aspect ratio periodic nanowires obtained via top-down route," Appl. Phys. A **122**, Art. No. 52 (2016).

8. Y. H. Ko, M. Niraula, K. J. Lee, and R. Magnusson, "Properties of wideband resonant reflectors under fully conical light incidence," Opt. Express **22**, 25817–25829 (2016).

Conference Proceedings

1. J. W. Yoon, K. J. Lee, M. Niraula, M. S. Amin, and R. Magnusson, "Properties of photonic and plasmonic resonance devices," Nanotek (Invited, San Fransisco, California) **4**, 148 (2014).

2. R. Magnusson, J. W. Yoon, M. Niraula, and K. J. Lee, "Guided-mode resonant nanophotonic devices: Physics, design, fabrication, and characterization," Proc. PIERS (Invited, Prague, Czech Republic) **36**, 687 (2015).

3. R. Magnusson, M. Niraula, J. W. Yoon, Y. H. Ko, and K. J. Lee, "Guided-mode resonance nanophotonics in materially sparse architectures," Proc. SPIE High Contrast Metasurfaces V (San Francisco, California) **9757** , 975705 (2016).

4. R. Magnusson, J. W. Yoon, M. Niraula, K. J. Lee, and H. Svavarsson, "Resonance-based nanophotonic device technology: filters, polarizers, and absorbers," IEEE Aerospace Conference (Big Sky, Montana) **37**, (2016).

References

[1] R. W. Wood, "On a remarkable case of uneven distribution of light in a diffraction grating spectrum," Philos. Mag. **4**, 396–402 (1902).

[2] Lord Rayleigh, "Note on the remarkable case of diffraction spectra described by Prof. Wood," Philos. Mag. **14**, 60–65 (1907).

[3] J. Strong, "Effect of evaporated films on energy distribution in grating spectra," Phys. Rev. **49**, 291–296 (1936).

[4] U. Fano, "The theory of anomalous diffraction gratings and of quasi-stationary waves on metallic surfaces (Sommerfeld's waves)," J. Opt. Soc. Am. **31**, 213–222 (1941).

[5] Hessel and A.A. Oliner, "A new theory of Wood's anomalies on optical gratings," Appl. Opt. **4**, 1275–1297 (1965).

[6] W. W. Ng, C.-S. Hong, and A. Yariv, "Holographic Interference Lithography for Integrated Optics," IEEE Trans. Elect. Dev. **25**, 1193–1200 (1978).

[7] M. G. Moharam and T. K. Gaylord, "Rigorous coupled-wave analysis of planar-grating diffraction," J. Opt. Soc. Am. **71**, 811–818.

[8] L. Mashev and E. Popov, "Zero order anomaly of dielectric coated gratings," Opt. Comm. **55**, 377–380 (1985).

[9] S. S. Wang, R. Magnusson, J. S. Bagby, and M. G. Moharam, "Guided-mode resonances in planar dielectric-layer diffraction gratings," J. Opt. Soc. Am. A **7**, 1470–1474 (1990).

[10] R. Magnusson and S. S. Wang, "New principle for optical filters," Appl. Phys. Lett. **61**, 1022 (1992).

[11] D. L. Brundrett, E. N. Glytsis, and T. K. Gaylord, "Normal-incidence guided-mode resonant grating filters: design and experimental demonstration," Opt. Lett. **23**, 700–702 (1998).

[12] Z. S. Liu, S. Tibuleac, D. Shin, P. P. Young, and R. Magnusson, "High-efficiency guided-mode resonance filter," Opt. Lett. **23**, 1556–1558 (1998).

[13] R. Magnusson and S. S. Wang, "Transmission bandpass guided-mode resonance filters," Appl. Opt. **34**, 8106–8109 (1995).

[14] S. Tibuleac and R. Magnusson, "Narrow-linewidth bandpass filters with diffractive thin-film layers," Opt. Lett. **26**, 584–586 (2001).

[15] M. Shokooh-Saremi and R. Magnusson, "Particle swarm optimization and its application to the design of diffraction grating filters," Opt. Lett. **32**, 894-896 (2007).

[16] Y. Ding and R. Magnusson, "Doubly resonant single-layer bandpass optical filters," Opt. Lett. **29**, 1135–1137 (2004).

[17] C. F. R. Mateus, M. C. Y. Huang, C. J. Chang-Hasnain, and Y. Sujuki, "Broad-band mirror (1.12-1.62 µm) using a subwavelength grating," IEEE Phot. Tech. Lett. **16**, 1676–1678 (2004).

[18] R. Magnusson, "Wideband reflectors with zero-contrast gratings," Opt. Lett. **39**, 4337–4340 (2014).

[19] M. Shokooh-Saremi and R. Magnusson, "Properties of two-dimensional resonant reflectors with zero-contrast gratings," Opt. Lett. **39**, 6958–6961 (2014).

[20] S. Kaja, J. D. Hilgenberg, J. L. Collins, A. A. Shah, D. Wawro, S. Zimmerman, R. Magnusson, and P. Koulen, "Detection of novel biomarkers for ovarian cancer with an

optical nanotechnology detection system enabling label-free diagnostics," J. Biomed. Opt. **17**, 081412–1 (2012).

[21] S. Y. Chou and W. Deng, "Subwavelength amorphous silicon transmission gratings and applications in polarizers and waveplates," Appl. Phys. Lett. **67**, 742–744 (1995).

[22] K. J. Lee, J. Curzan, M. Shokooh-Saremi, and R. Magnusson, "Resonant wideband polarizer with single silicon layer," Appl. Phys. Lett. **98**, 21112 (2011).

[23] J. A. Giese, J. W. Yoon, B. R. Wenner, J. W. Allen, M. S. Allen, and R. Magnusson, "Guided-mode resonant coherent light absorbers," Opt. Lett. **39**, 486–488 (2014).

[24] J. W. Yoon, K. J. Lee, W. Wu, and R. Magnusson, "Wideband omnidirectional polarization-insensitive light absorbers made with 1D silicon gratings," Adv. Opt. Mater. **2**, 1206–1212 (2014).

[25] S. S. Wang and R. Magnusson, "Theory and applications of guided-mode resonance filters," Appl. Opt. **32**, 2606–2613 (1993).

[26] T. K. Gaylord and M. G. Moharam, "Analysis of application of optical diffraction by gratings," Proc. IEEE **73**, 894–937 (1985).

[27] D. Marcuse, *Theory of Dielectric Optical Waveguides* (Academic, New York, ed. 2, 1991).

[28] M. G. Moharam, E. B. Grann, D. A. Pommet, and T. K. Gaylord, "Formulation for stable and efficient implementation of the rigorous coupled-wave analysis of binary gratings," J. Opt. Soc. Am. A **12**, 1068–1076 (1995).

[29] M. G. Moharam, D. A. Pommet, E. B. Grann, and T. K. Gaylord, "Stable implementation of the rigorous coupled-wave analysis for surface-relief gratings: enhanced transmittance matrix approach," J. Opt. Soc. Am. A **12**, 1077-1086 (1995).

[30] J.-M. Jin, *The Finite Element Method in Electromagnetics* (Wiley-IEEE, New York, ed. 3, 2014).

[31] J. Kennedy and R. Eberhart, "Particle swarm optimization," Proceedings of the IEEE International Conference on Neural Networks **4**, 1942–1948 (1995).

[32] J. R. Devore, "Refractive indices of rutile and sphalerite," J. Opt. Soc. Am. **41**, 416-419 (1951).

[33] Y. Ding and R. Magnusson, "Resonant leaky-mode spectral-band engineering and device applications," Opt. Express **12**, 5661–5674 (2004).

[34] R. Magnusson, J. W. Yoon, M. S. Amin, T. Khaleque, and M. J. Uddin, "Extraordinary capabilities of optical devices incorporating guided-mode resonance gratings: application summary and recent examples," Proc. SPIE **8988**, 898801 (2014).

[35] P. Vincent and M. Neviere, "Corrugated dielectric waveguides: A numerical study of the second-order stop bands," Appl. Opt. **20**, 345–351 (1979).

[36] Avrutsky and V. A. Sychugov, "Reflection of a beam of finite size from a corrugated waveguide," J. Mod. Opt. **36**, 1527–1539 (1989).

[37] S. Tibuleac and R. Magnusson, "Reflection and transmission guided-mode resonance filters," J. Opt. Soc. Am. A **14**, 1617–1626 (1997).

[38] S. Tibuleac, P. P. Young, R. Magnusson, and T. R. Holzheimer, "Experimental verification of waveguide-mode resonant transmission filters," IEEE Microwave and Guided Wave Lett. **9**, 19–21 (1999).

[39] Y. Kanamori, M. Shimono, and K. Hane, "Fabrication of transmission color filters using silicon subwavelength gratings on quartz substrates," IEEE Photon. Technol. Lett. **18**, 2126–2128 (2006).

[40] T. Sang, Z. Wang, X. Zhou, and S. Cai, "Resonant enhancement transmission in a Ge subwavelength periodic membrane," Appl. Phys. Lett. **97**, 071107 (2010).

[41] T. Sang, T. Cai, S. Cai, and Z. Wang, "Tunable transmission filters based on double subwavelength periodic membrane structures with an air gap," J. Opt. **13**, 125706 (2011).

[42] M. S. Amin, J. W. Yoon, and R. Magnusson, "Optical transmission filters with coexisting guided-mode resonance and Rayleigh anomaly," Appl. Phys. Lett. **103**, 131106 (2013).

[43] J. M. Foley, S. M. Young, and J. D. Phillips, "Narrowband mid-infrared transmission filtering of a single layer dielectric grating," Appl. Phys. Lett. **103**, 071107 (2013).

[44] R. McKeracher, L. Fu, H. H. Tan, and C. Jagadish, "Integration of bandpass guided-mode resonance filters with mid-wavelength infrared photodetectors," J. Phys. D Appl. Phys. **46**, 095104 (2013).

[45] C. J. Chang-Hasnain and W. Yang, "High-contrast gratings for integrated optoelectronics," Adv. Opt. Photon. **4**, 379–440 (2012).

[46] Y. Ding, *Resonant leaky-mode spectral-band engineering and device applications* (Ph. D. dissertation, University of Connecticut, 2006).

[47] J. W. Yoon and R. Magnusson, "Fano resonance formula for lossy two-port systems," Opt. Express **21**, 17751–17759 (2013).

[48] J. Yoon, M. J. Jung, S. H. Song, and R. Magnusson, "Analytic theory of the resonance properties of metallic nanoslit arrays," IEEE J. Quantum Electron. **48**, 852–861 (2012).

[49] H. A. Macleod, *Thin-Film Optical Filters* (McGraw-Hill, New York, ed. 3, 1989).

[50] B. E. A. Saleh and M. C. Teich, *Fundamentals of Photonics* (Wiley, New York, ed. 2, 2007).

[51] Y. Fink, J. N. Winn, S. Fan, C. Chen, J. Michel, J. D. Joannopoulos, and E. L. Thomas, "A dielectric omnidirectional reflector," Science **282,** 1679-1682 (1998).

[52] C. F. R. Mateus, M. C. Y. Huang, Y. Deng, A. R. Neureuther, and C. J. Chang-Hasnain, "Ultrabroadband mirror using low-index cladded subwavelength grating," IEEE Photon. Technol. Lett. **16**, 518–520 (2004).

[53] S. Peng, and G. M. Morris, "Resonant scattering from two-dimensional gratings," J. Opt. Soc. Am. A **13**, 993–1005 (1996).

[54] D. W. Peters, R. R. Boye, J. R. Wendt, R. A. Kellogg, S. A. Kemme, T. R. Carter, and S. Samora, "Demonstration of polarization-independent resonant subwavelength grating filter arrays," Opt. Lett. **35,** 3201-3203 (2010).

[55] D. Fattal, J. Li, Z. Peng, M. Fiorentino, and R. G. Beausoleil, "Flat dielectric grating reflectors with focusing abilities," Nat. Photon. **4,** 466–470 (2010).

[56] S. Tibuleac and R. Magnusson, "Diffractive narrow-band transmission filters based on guided-mode resonance effects in thin-film multilayers," IEEE Phot. Tech. Lett. **9,** 464-466 (1997).

[57] M. Niraula, J. W. Yoon, and R. Magnusson, "Mode-coupling mechanisms of resonant transmission filters," Opt. Exp. **22,** 25817-25829 (2014).

[58] International Telecommunication Union, *Spectral grids for WDM applications: DWDM frequency grid.* (ITU-T G.694.1, 2012; http://www.itu.int/rec/T-REC-G.694.1-201202-I/en).

[59] T. W. Ebbesen, H. J. Lezec, T. T. Ghaemi, and P. A. Wolff, "Extraordinary optical transmission through sub-wavelength hole arrays," Nature **391,** 667-669 (1998).

[60] U. Schröter and D. Heitmann, "Surface-plasmon-enhanced transmission through metallic gratings," Phys. Rev. B **58,** 15419-15421 (1998).

[61] E. Sakat, G. Vincent, P. Ghenuche, N. Bardou, S. Collin, F. Pardo, J.-L. Pelouard, and R. Haïdar, "Guided mode resonance in subwavelength metallodielectric free-standing grating for bandpass filtering," Opt. Lett. **36**, 3054–3056 (2011).

[62] R. Magnusson, D. Wawro, S. Zimmerman, and Y. Ding, "Resonant photonic biosensors with polarization-based multiparametric discrimination in each channel," Sensors **11**, 1476–1488 (2011).

[63] P. Reader-Harris, A. Ricciardi, T. Krauss, and A. D. Falco, "Optical guided mode resonance filter on a flexible substrate," Opt. Express **21**, 1002–1007 (2013).

[64] E. Garnett, and P. Yang, "Light trapping in silicon nanowire solar cells," Nano Lett. **10**, 1082–1087 (2010).

[65] D. C. Marinica, A. G. Borisov, and S. V. Shabanov, "Bound states in the continuum in photonics," Phys. Rev. Lett. **100**, 183902 (2008).

[66] C. W. Hsu, B. Zhen, J. Lee, S.-L. Chua, S. G. Johnson, J. D. Joannopoulos, and M. Soljačić, "Observation of trapped light within the radiation continuum," Nature **499**, 188–191 (2013).

[67] M. Flury, A. V. Tishchenko, and O. Parriaux, "The leaky mode resonance condition ensures 100% diffraction efficiency of mirror-based resonant gratings," J. Lightwave Technol. **25**, 1870–1878 (2007).

[68] N. Vermeulen, P. Wasylczyk, S. Tonchev, P. Muys, H. Ottevaere, O. Parriaux, and H. Thienpont, "Low-loss wavelength tuning of a mid-infrared Cr^{2+}:ZnSe laser using a littrow-mounted resonant diffraction grating," Laser Phys. Lett. **8**, 606612 (2011).

[69] R. Magnusson, "Flat-top resonant reflectors with sharply delimited angular spectra: an application of the Rayleigh anomaly," Opt. Lett. **38**, 989–991 (2013).

[70] D. Rosenblatt, A. Sharon, and A. A. Friesem, "Resonant grating waveguide structures," IEEE J. Quantum Electron. **33**, 2038–2059 (1997).

[71] J. Yoon, K. H. Seol, S. H. Song, and R. Magnusson, "Critical coupling in dissipative surface-plasmon resonators with multiple ports," Opt. Express **18**, 25702–25711 (2010).

[72] M. Niraula, J. W. Yoon, and R. Magnusson, "Single-layer optical bandpass filter technology," Opt. Lett. **40**, 5062–5065 (2015).

[73] R. Magnusson and M. Shokooh-Saremi, "Physical basis for wideband resonant reflectors," Opt. Express **16**, 3456–3462 (2008).

[74] T. Khaleque, M. J. Uddin, and R. Magnusson, "Design and fabrication of broadband guided-mode resonant reflectors in TE polarization," Opt. Express **22**, 12349-12358 (2014).

[75] M. A. Green, "Self-consistent optical parameters of intrinsic silicon at 300 K including temperature coefficients," Sol. Energy Mater. Sol. Cells **92**, 1305-1310 (2008).

[76] K. Ikeda, K. Takeuchi, K. Takayose, I.-S. Chung, J. Mørk, and H. Kawaguchi, "Polarization-independent high-index contrast grating and its fabrication tolerances," Appl. Opt. **52**, 1049-1053 (2013).

[77] Y. H. Ko, M. Shokooh-Saremi, and R. Magnusson, "Modal processes in two-dimensional resonant reflectors and their correlation with spectra of one-dimensional equivalents," IEEE Photon. J. 7, 4900210 (2015).

[78] D. Zhao, H. Yang, Z. Ma, and W. Zhou, "Polarization independent broadband reflectors based on cross-stacked gratings," Opt. Express **19**, 9050-9055 (2011).

[79] S. Y. Lin, J. G. Fleming, D. L. Hetherington, B. K. Smith, R. Biswas, K. M. Ho, M. M. Sigalas, W. Zubrzycki, S. R. Kurtz, and J. Bur, "A three-dimensional photonic crystal operating at infrared wavelengths," Nature **394**, 251-253 (1998).

[80] J. M. Bennett and E. J. Ashley, "Infrared reflectance and emittance of silver and gold evaporated in ultrahigh vacuum," Appl. Opt. **4**, 221-224 (1965).

[81] A.-L. Fehrembach, K. C. Shin Yu, A. Monmayrant, P. Arguel, A. Sentenac, and O. Gauthier-Lafaye, "Tunable, polarization independent, narrow-band filtering with one-dimensional crossed resonant gratings," Opt. Lett. **36**, 1662–1664 (2011).

[82] F. Lemarchand, A. Sentenac, and H. Giovannini, "Increasing the angular tolerance of resonant grating filters with doubly periodic structures," Opt. Lett. **23**, 1149–1151 (1998).

[83] A.-L. Fehrembach, A. Talneau, O. Boyko, F. Lemarchand, and A. Sentenac, "Experimental demonstration of a narrowband angular tolerant, polarization independent doubly periodic resonant grating filter," Opt. Lett. **32**, 2269–2271 (2007).

[84] K. Kintaka, T. Majima, J. Inoue, K. Hatanaka, J. Nishii, and S. Ura, "Cavity-resonator-integrated guided-mode resonance filter for aperture miniaturization," Opt. Express **20,** 1444–1449 (2012).

[85] X. Buet, E. Daran, D. Belharet, F. Lozes-Dupuy, A. Monmayrant, and O. Gauthier-Lafaye, "High angular tolerance and reflectivity with narrow bandwidth cavity-resonator-integrated guided-mode resonance filter," Opt. Express **20**, 9322–9327 (2012).

[86] X. Baillard, A. Gauguet, S. Bize, P. Lemonde, P. Laurent, A. Clairon, and P. Rosenbusch, "Interference-filter-stabilized external-cavity diode lasers," Opt. Comm. **266**, 609–613 (2006).

[87] D. Lacour, J-P. Plumey, G. Granet, and A. Mure-Ravaud, "Resonant waveguide grating: Analysis of polarization independent filtering," Opt. Quantum Electron. **33**, 451–470 (2001).

[88] D. W. Peters, R. R. Boye, and S. A. Kemme, "Angular sensitivity of guided mode resonant filters in classical and conical mounts," Proceedings of SPIE **8633**, 86330W (2013).

[89] A. Ricciardi, S. Campopiano, A. Cusano, T. F. Krauss, and L. O'Faolain, "Broadband mirrors in the near-infrared based on subwavelength gratings in SOI," IEEE Photon. J. **2**, 696–702 (2010).

[90] J. W. Yoon, K. J. Lee, and R. Magnusson, "Ultra-sparse dielectric nanowire grids as widebands reflectors and polarizers," Opt. Express **23**, 28849–28856 (2015).

[91] C. J. M. van Rijn, "Laser interference as a lithographic nanopatterning tool," J. Microlith., Microfab., Microsyst. **5**, 011012 (2006).

[92] J.-H. Seo, J. H. Park, S.-I. Kim, J. Bang, Z. Ma, J. Choi, and B.-K. Ju, "Nanopatterning by Laser Interference Lithography: Applications to Optical Devices," J. of Nanoscience and Nanotechnology **14**, 1521–1532 (2014).

Biographical Information

Manoj Niraula completed his PhD in electrical engineering in 2016 and his B. Sc. in electrical engineering in 2013 from the University of Texas at Arlington. He joined the Nanophotonics Device Group, led by Dr. Robert Magnusson, at the University of Texas at Arlington in May 2013 and began undergraduate research in the field of resonant periodic devices for optical applications. Work he started as an undergraduate researcher led to two publications in peer-reviewed journals.

He joined the Ph.D. program in electrical engineering at the University of Texas at Arlington in January 2014 and continued his research as a Graduate Research Associate. His research interests include theoretical analysis of the guided-mode resonance mechanism in subwavelength and non-subwavelength periodic structures, fabrication of resonant periodic devices, establishment and optimization of lithography and reactive ion etching processes, and characterization of fabricated samples. He also enjoys designing microcontroller-based hardware and software. After graduation, Manoj plans to join the semiconductor/photonics industry to fill a position of his expertise.